

NANOSTRUCTURE EFFECT ON RADIATION DETECTION  
AND ENERGY STORAGE DEVICES

By

ALYSON C. NIEMEYER

A DISSERTATION PRESENTED TO THE GRADUATE SCHOOL  
OF THE UNIVERSITY OF FLORIDA IN PARTIAL FULFILLMENT  
OF THE REQUIREMENTS FOR THE DEGREE OF  
DOCTOR OF PHILOSOPHY

UNIVERSITY OF FLORIDA

2010

© 2010 Alyson C. Niemeyer

To all who nurtured my intellectual curiosity, academic interests, and sense of scholarship throughout my lifetime, making this milestone possible

## ACKNOWLEDGMENTS

I thank the chair (Dr. Franky So) and members of my supervisory committee for their mentoring and guidance. In addition, I would like to acknowledge my mentors at Los Alamos National Laboratory for their support, especially Dr. Neil Henson and Dr. Michele DeCroix for counseling both in scientific areas as well as career advice. Finally, I thank my family (including those who are no longer with us) and my fiancé Corey for their loving encouragement, which motivated me to complete my study.

## TABLE OF CONTENTS

	<u>page</u>
ACKNOWLEDGMENTS.....	4
LIST OF TABLES.....	8
LIST OF FIGURES.....	9
ABSTRACT .....	13
CHAPTER	
1 IMPORTANCE OF NANOSTRUCTURE EFFECT.....	15
2 INTRODUCTION TO RADIATION DETECTION DEVICES.....	18
Homeland Security Application.....	18
Current Technology .....	19
Scintillators.....	19
Photomultiplier Tubes.....	20
Photodiodes .....	21
Organic Materials.....	23
Improvements Over Si Photodiodes.....	23
Effect of Radiation on Organic Materials .....	24
Interdigitated Structure.....	25
3 THEORETICAL BACKGROUND .....	31
Semiconducting and Conducting Polymers .....	31
Band Theory.....	31
Hopping Conduction.....	33
Charge Carriers.....	34
Transport Mechanisms in Conjugated Polymers .....	35
Bulk vs. Planar Heterojunctions .....	36
4 BULK HETEROJUNCTION .....	42
Device Structure and Operation.....	42
Device Fabrication and Measurement .....	44
Device Optimization.....	45
Effect of Polymer Film Thickness .....	46
Effect of Polymer Ratio.....	46
Effect of Interdigitated Finger Spacing .....	47
Effect of Applied Field .....	47
Data Analysis.....	48

Onsager Model .....	50
Conclusions .....	52
5 PLANAR HETEROJUNCTION .....	67
Device Structure and Operation.....	67
Device Fabrication .....	69
Model for Exciton Dissociation.....	70
Importance of Heterojunction Energy Offsets .....	73
Conclusions .....	75
6 INTRODUCTION TO ENERGY STORAGE DEVICES .....	86
Importance of Portable Energy Storage.....	86
Current Technology .....	87
Batteries .....	87
Capacitors .....	88
Supercapacitors for Energy Storage.....	89
Carbon Nanotube Electric Double-Layer Supercapacitors.....	91
7 THEORETICAL BACKGROUND .....	96
Electrostatics .....	96
Computational Modeling .....	97
Molecular Dynamics Calculations.....	98
Density Functional Theory.....	99
8 NANOSCALE SHAPED ELECTRODES.....	101
Introduction .....	101
Methods and Models.....	102
Results and Discussion.....	103
CO in Absence of an Electric Field .....	103
Applied Field to Break CO Bond.....	104
Electric Field Gradient .....	106
Molecular Orbital Energies .....	106
Electron Density .....	107
Dinitrogen .....	107
Conclusions .....	108
9 CARBON NANOTUBE SUPERCAPACITORS .....	120
System Composition.....	120
Calculation Details .....	121
Results and Discussion.....	122
Acetonitrile Electrolyte System .....	122
Difference between positively and negatively charged CNT .....	122
Decreasing charge on CNT.....	123

Discharged CNT .....	124
Electric Field of Total System.....	124
Time dependence of ion distribution .....	125
Time dependence of electric field strength.....	125
Effects of each component.....	126
Water Electrolyte System .....	126
Polarization.....	128
Conclusions .....	129
<b>10 CONCLUSIONS .....</b>	<b>150</b>
Organic Electronic Photoconductors.....	151
Bulk Heterojunction .....	151
Planar Heterojunction.....	152
Future Work.....	152
Capacitors for Energy Storage.....	153
Electrode Geometry .....	153
Electric Double-Layer Carbon Nanotube Supercapacitors .....	154
Future Work.....	154
<b>LIST OF REFERENCES .....</b>	<b>156</b>
<b>BIOGRAPHICAL SKETCH.....</b>	<b>164</b>

## LIST OF TABLES

<u>Table</u>		<u>page</u>
2-1	Properties of some commercially available organic and inorganic scintillators...	27
6-1	Summary of electric double-layer super capacitors literature review.....	95
8-1	Summary of electrode shapes made from point charges .....	111
8-2	Summary of results of calculations in absence of an applied electric field .....	112
8-3	Calculation summary for dinitrogen molecule.....	119
9-1	Calculation summary.....	134
9-2	Calculation Summary for $K_2SO_4$ electrolyte.....	143

## LIST OF FIGURES

<u>Figure</u>		<u>page</u>
2-1	Schematic diagram of photomultiplier tube.....	28
2-2	Basic configuration of a conventional photodiode.....	29
2-3	Spectral response of a typical silicon photodiode.....	29
2-4	Mobilities of common organic materials.....	30
3-1	The overlapping of $2sp^2$ and $2p_z$ orbitals forms $\sigma$ and $\pi$ bonds respectively.....	38
3-2	Structure of two typical polymers where the backbone is conjugated (double and single bonds alternate) .....	38
3-3	Diagram of electron transfer mechanisms between adjacent sites separated by a potential-energy barrier.....	39
3-4	Schematic illustration of an electron moving along a polymer chain where double bonds flip back and forth to accommodate its passage .....	40
3-5	Schematic diagram depicting conceptually the photoinduced charge transfer in a bilayer and bulk heterojunction .....	41
4-1	Schematic drawing of MEH-PPV/PCBM photoconductor devices.....	54
4-2	Picture of MEH-PPV/PCBM device. ....	55
4-3	Energy band diagram for organic materials used in quantum efficiency study... ..	55
4-4	Interpenetrating organic networks. White: MEH-PPV, Grey: PCBM.....	56
4-5	Absorption spectrum for MEH-PPV/PCBM polymer solution.....	57
4-6	Typical dark current of MEH-PPV/PCBM interdigitated device.....	58
4-7	Schematic drawing of equipment setup for characterization of quantum efficiency. ....	59
4-8	Effect of polymer layer thickness on quantum efficiency. ....	60
4-9	Effect of polymer ratio on quantum efficiency.....	61
4-10	Spectral response of quantum efficiency as a function of applied field.....	62
4-11	Effect of applied field on peak quantum efficiency.....	63

4-12	Absorption spectra of 60 nm thick films.....	64
4-13	Quantum efficiency spectra of 165 nm thick 1:3 MEH-PPV:PCBM with 10 $\mu\text{m}$ spacing electrodes for 0.04, 0.1 and 0.2 MV/cm applied fields.....	65
4-14	Quantum efficiency at 494 nm versus applied electric field for 165 nm thick 1:3 MEH-PPV:PCBM interdigitated devices .....	66
5-1	Schematic of device with a planar heterojunction.....	76
5-3	Materials used for multilayers in planar heterojunction devices.....	77
5-4	Quantum efficiency for $\alpha$ -6T/ $\text{C}_{60}$ devices with different spacings at the same field.....	78
5-5	Device layout for exciton dissociation model.....	78
5-6	Organic transport levels for materials used in this study. ....	79
5-7	Absorption spectra for each polymer.....	80
5-8	Quantum efficiency of each material at an applied voltage of 80V.....	81
5-9	Quantum efficiency of F8BT/ $\text{C}_{60}$ devices at increasing applied voltage.....	82
5-10	Quantum efficiency contribution with increasing applied field for each polymer.....	83
5-11	Summary of quantum efficiency contribution with increasing applied field for each polymer.....	84
5-12	Energy offset compared to quantum efficiency contribution for each polymer alone, and in a device with $\text{C}_{60}$ .....	85
6-1	How a conventional dry cell battery works.....	94
8-1	Schematic of model electrode setup.....	109
8-2	Electrode shapes consisting of point charge arrays .....	110
8-3	Diagram of calculation set-up for CO molecule between two charged electrodes of different geometries .....	111
8-4	Uniform electric field between two plates, and curved electric field between a sphere and a plate.....	112
8-5	Bond length of CO molecule plotted against applied electric field for field created between two charged plates.....	113

8-6	Bond length of CO molecule plotted against applied electric field for field created between a charged plate and a charged cylinder .....	114
8-7	Bond length of CO molecule plotted against applied electric field for field created between a charged plate and a charged sphere.....	115
8-8	Molecular orbital diagram for carbon monoxide.....	116
8-9	Energy of the molecular orbitals in the CO molecule as an external, axial electric field is applied .....	117
8-10	Highest occupied molecular orbitals and total electron density. ....	118
9-1	Uncharged and charged capacitors.....	131
9-2	Molecules that make up the electrolyte solution surrounding the carbon nanotube. ....	132
9-3	Entire carbon nanotube supercapacitor system with carbon nanotube in center surrounded by electrolyte .....	133
9-4	Difference between positively and negatively charged CNT.....	134
9-5	Difference between positively and negatively charged CNT, density / bulk density .....	135
9-6	Decreasing charge on CNT .....	136
9-7	Increasing density.....	137
9-8	Discharged CNT .....	138
9-9	Electric field of total system .....	138
9-10	Electric field effects.....	139
9-11	Effect of increased CNT charge on applied field.....	139
9-12	Time dependence of the distribution of ions for Case 3.....	140
9-13	Time dependence of the electric field strength for Case 3.....	140
9-14	System with and without dielectric present.....	141
9-15	Charge and uncharged system with ions only, no dielectric.....	142
9-16	Surface attraction for Case 10.....	143
9-17	Effect of increasing molarity for a negatively charged nanotube.....	144

9-18	Effect of increasing molarity for a positively charged nanotube .....	145
9-19	Difference between positively and negatively charged nanotube at the same molarity .....	146
9-20	Radial distribution of nanotube with no applied charge .....	146
9-21	Electric field of total system .....	147
9-22	Electric field on discharged system. ....	148
9-23	Electron density of acetonitrile, boron tetrafluoride and tetraethylammonium. .	149

Abstract of Dissertation Presented to the Graduate School  
of the University of Florida in Partial Fulfillment of the  
Requirements for the Degree of Doctor of Philosophy

NANOSTRUCTURE EFFECT ON RADIATION DETECTION  
AND ENERGY STORAGE DEVICES

By

Alyson C. Niemeyer

May 2010

Chair: Franky So

Major: Materials Science and Engineering

Nanostructured materials differ from conventional bulk materials in the size of the structural units that compose them. Also they often exhibit properties that are drastically different from those of conventional materials. In this study, we focus on two specific areas where the nanoscale plays an important role: the development of nuclear radiation detection and energy storage devices. The first half of this study focuses on experiments performed to evaluate new structures and materials for photoconductor devices and how they are used for radiation detection. The second half of the study focuses on computational modeling of double-layer carbon nanotube supercapacitors for electrical energy storage and how each component of the system as well as the whole system is affected by an electric field.

In the photoconductor section of this work, devices with bulk heterojunctions and planar heterojunctions were fabricated and studied in order to determine how the transport process limits the quantum efficiency. The photoconductivity in interdigitated lateral photoconductors with a poly[2-methoxy-5-(2-ethylhexyl-oxy)-1,4-phenylene-vinylene] [MEH-PPV] / {6}-1-(3-(methoxycarbonyl) propyl)-{5}-1-phenyl-[6,6]-C61 [PCBM] blend as the active layer was investigated. It was found that the quantum

efficiency was limited by the dissociation of excitons, which was explained using a modified Onsager model for charge dissociation. In planar heterojunction devices, it was found that (1) trap sites in the active layer limited the quantum efficiency and (2) a larger heterojunction energy offset of the Lowest Unoccupied Molecular Orbital (LUMO) leads to higher quantum efficiency.

To study the use of double-layer carbon nanotubes for energy storage, we investigated the effect of an electric field on a single molecule at a short distance from an electrode as well as the supercapacitor system as a whole. Quantum chemical calculations were performed on a carbon monoxide molecule in an applied electric field with electrodes of different shapes. A 25% reduction in the applied field necessary to break the bond was found for a field generated by a spherical electrode when compared to a uniform field, which was determined to be due to the difference in the electric field gradient. Molecular dynamics simulations of supercapacitors based on carbon nanotubes were also performed. Results from calculations focusing on the molecular response of the nanotube-electrolyte assembly in the presence of an applied electric field were studied for electrolytes consisting of acetonitrile, boron tetrafluoride and tetraethylammonium, and water and potassium sulfate. Results demonstrating the effect of the electric field on the electric double-layer for a variety of conditions are discussed. It was found that (1) the relative sizes of the ions had the greatest effect on the molecular distribution in the charged double layer and (2) a “molecular packing” affect was observed.

## CHAPTER 1 IMPORTANCE OF NANOSTRUCTURE EFFECT

In this work, we study the nanostructure effect on nuclear radiation detection and energy storage applications. Nanostructured materials are a new class of materials which provide one of the greatest potentials for improving performance and extended capabilities of products in a number of industrial sectors, including the aerospace, tooling, automotive, recording, cosmetics, electric motor, duplication, and refrigeration industries.<sup>1</sup> Encompassed by this class of materials are multilayers, nanocrystalline materials and nanocomposites. Their uniqueness is due partially to the very large percentage of atoms at interfaces and partially to quantum confinement effects.

Nanoscale science, engineering and technology are concerned with the manipulation of matter on the nanometer length scale, which is now generally taken as the 1 to 100 nm range. Although nanoscience might simply be seen as a natural and necessary progression from the submicron-scale engineering that has driven the microelectronics and computing industries thus far, it is not merely the trend towards higher levels of miniaturization but the wealth of novel physical, chemical and biological behavior that occurs on the nanometer scale that makes nanoscience such a fundamentally exciting and technologically relevant area of research.<sup>2</sup>

A bulk material should have constant physical properties regardless of its size, but at the nano-scale size-dependent properties are often observed. In many instances, this is a result of the large fraction of grain boundaries in bulk materials, and hence the percentage of surface atoms. For example, for close-packed spheres the percentage of surface atoms is about 80% for a 50-atom particle, and is still 20% for a particle

containing as many as 2000 atoms. Due to the large surface area of nanomaterials, bulk properties become governed by surface properties.<sup>3</sup>

There are many examples of materials that have different properties at the nanoscale than they exhibit in the bulk. The absorption of solar radiation in photovoltaic cells is much higher in materials composed of nanoparticles than it is in thin films of continuous sheets of material, where smaller particles have greater absorption of solar energy. Other size-dependent property changes include quantum confinement in semiconductor particles, surface plasmon resonance in some metal particles and superparamagnetism in magnetic materials.

Zinc oxide particles have been found to have superior UV blocking properties compared to its bulk substitute. Sunscreens are utilizing nanoparticles that are extremely effective at absorbing light, especially in the ultra-violet (UV) range. Due to the particle size, they spread more easily, cover better, and save money since smaller quantities are required. They are also transparent, unlike traditional screens which are white.<sup>4</sup>

Nanoparticles have a very high surface area to volume ratio, which provides a tremendous driving force for diffusion, especially at elevated temperatures, and can reduce the incipient melting temperature of nanoparticles.<sup>5</sup> Clay nanoparticles when incorporated into polymer matrices increase reinforcement, leading to stronger plastics, verifiable by a higher glass transition temperature and mechanical property tests. These nanoparticles are hard, and impart their properties to the polymer (plastic).<sup>6</sup>

Nanoparticles have also been attached to textile fibers in order to create smart and functional clothing.<sup>7</sup> A company called NanoTex makes stain-resistant pants, with

surface fibers of 10 to 100 nanometers, uses a process that coats each fiber of fabric with "nano-whiskers."<sup>8</sup> Using aluminum nanoparticles, Argonide<sup>9</sup> has created rocket propellants that burn at double the rate of propellants made from non-nanoscale materials. They also produce copper nanoparticles that are incorporated into automotive lubricant to reduce engine wear.

These are just a few examples of ways that nanoparticles exhibit different (often enhanced) properties when compared to the bulk. That is why we choose to study this class of materials to improve radiation detection and energy storage devices.

## CHAPTER 2 INTRODUCTION TO RADIATION DETECTION DEVICES

In the first half of this study, we investigate replacing the photomultiplier tubes in scintillators with photoconductors to make the detectors less bulky. Lateral photoconductors with interdigitated (see explanation on p.25) electrodes and organic materials used for the active layer are studied. Photoconductors are devices that increase their electrical conductivity when exposed to light. Typically, they are made in a sandwich structure of electrode – active layer – electrode where the transport occurs vertically in the device. In devices with interdigitated electrodes, the transport occurs laterally (normal to the direction of absorption). The photoconductors in this study operate in a similar fashion to typical organic photovoltaics or solar cells, where light (photons) is absorbed in the organic active layer and electrons are collected at the electrodes.

### **Homeland Security Application**

There is a great need for low cost, large area  $\gamma$ -radiation detectors for Special Nuclear Material (SNM) and radiological isotope monitoring.<sup>10</sup> These detectors will require large area and low cost scintillators, such as plastic or liquid scintillators, as well as large area low cost photoconductors to read out the scintillator light. Organic electronic materials have many attributes which make them an attractive candidate material for photoconductors including: low cost processing over large areas and volumes; high quantum efficiency; low intrinsic dark current at room temperature; low dielectric constant; and high bulk resistivities permitting low capacitance interdigitated structures.<sup>11</sup> Organic photoconductors for radiation detection applications will be encased in metal with the scintillator and will only be exposed to the scintillator's light,

so that photodegradation will not be a major concern for these devices. High quantum efficiency is a critical parameter for photoconductors for radiation detection, and requires efficient exciton dissociation, separation of charges into distinct transport manifolds, and collection of these charges without their recombining. A quantitative understanding of exciton dissociation, charge separation, and carrier transport is necessary to enable design of optimum organic photoconductors.

The organic photoconductors developed in this study could provide a low cost, large area (>10cm<sup>2</sup>) alternative to conventional silicon photodiodes for readout of large scintillators that are used at border crossings, ports, toll plazas, nuclear facilities, etc. for monitoring the movement of radioactive material and distinguishing threats from non-threats.<sup>10</sup>

### **Current Technology**

The scintillation process is one of the most useful methods available for the detection and spectroscopy of a wide assortment of radiations. Photomultiplier tubes are the most common light amplifiers used with scintillators. However, advances in the development of semiconductor photodiodes have led to the substitution of solid-state devices for photomultiplier tubes in some applications.

### **Scintillators**

One of the overworked images of radiation in popular perception is the idea that radioactive materials glow, emitting some form of eerie light. Most materials when irradiated with gamma rays do not emit light; however, low-intensity visible and ultraviolet light can be detected from some transparent materials owing to the energy deposited by interacting charged particles. In certain types of transparent materials, the energy deposited by an energetic particle can create excited atomic or molecular states

that quickly decay through the emission of visible or ultraviolet light, a process sometimes called prompt fluorescence. Such materials are known as scintillators and are commonly exploited in scintillation detectors.

There are many characteristics that are desirable in a scintillator, including high scintillation efficiency, short decay time, linear dependence of the amount of light generated on deposited energy, good optical quality, and availability in large sizes at modest cost. No known material meets all these criteria, and therefore many different materials are in common use, each with attributes that are best suited for certain applications. Most scintillators for common use are either inorganic crystals or organic-based liquids and plastics, the most common being thallium-doped sodium iodide crystals, which have a high radiation-to-light conversion efficiency. Inorganic scintillators generally tend to have the best light output and linearity, but with several exceptions are relatively slow in their response time. Organic scintillators are generally faster but yield less light. Table 2-1 shows some typical properties of organic and inorganic scintillators. The intended application has the largest influence on scintillator choice.

### **Photomultiplier Tubes**

The use of scintillators in radiation detection would be impossible without devices to convert the extremely weak light output of a scintillation pulse into a corresponding electrical signal. A photomultiplier tube is an instrument that detects low levels of electromagnetic radiation (usually visible light or infrared radiation) and amplifies it to produce a detectable electrical signal. One type resembles a photocell with an additional series of coated electrodes (dynodes) between the cathode and anode. Photons striking the cathode releases electrons (primary emission) that hit the first dynode, producing yet more electrons (secondary emission), which strike the second

dynode. Eventually this produces a measurable signal up to 100 million times larger than the signal produced in the first stage by the time it leaves the anode. The simplified structure of a typical photomultiplier tube is illustrated in Figure 2-1.

The spectral response, quantum efficiency, sensitivity, and dark current of a photomultiplier tube are determined by the composition of the photocathode. The best photocathodes capable of responding to visible light are less than 30 percent quantum efficient, meaning that 70 percent of the photons impacting on the photocathode do not produce a photoelectron and are therefore not detected. Photocathode thickness is an important variable that must be monitored to ensure the proper response from absorbed photons. If the photocathode is too thick, more photons will be absorbed but fewer electrons will be emitted from the back surface, but if it is too thin, too many photons will pass through without being absorbed.

Large area scintillators are currently used for radiation detection, but using photomultiplier tubes for converting their light output into an electrical signal can also be problematic. Photomultiplier tubes are fragile, bulky, costly, sensitive to magnetic fields, and power hungry. To address these issues, there has been a great deal of interest in studying solid-state devices (e.g. photodiodes or other types of photoconductors) as substitutes for photomultiplier tubes for radiation detection and other applications.

### **Photodiodes**

Photoconductors and photodiodes specifically are devices capable of converting light into an electrical signal. A common configuration for a silicon photodiode is shown in Figure 2-2. When light is incident on a semiconductor, electron-hole pairs are generated as the photon is absorbed. Photons corresponding to typical scintillation light carry about 3-4eV of energy, which is sufficient to create electron-hole pairs in a

semiconductor with a bandgap of approximately 1-2eV. The conversion is not limited by the need for charge carriers to escape from a surface as in a conventional photocathode, so the maximum quantum efficiency of the process can be as high as 60-80%, several times larger than in a photomultiplier tube. This high quantum efficiency also plans a much wider wavelength range than is typical for photocathodes in photomultiplier tubes, so a much higher primary charge usually is created by the light from the scintillator.

For the readout of scintillators, PIN photodiodes in reversed bias operation are commonly used. They typically have the following performance parameters: 70pF/cm<sup>2</sup> capacitance for a 200μm thick wafer, response time on the order of ns, and the dark current at ~20V reversed bias voltage and at room temperature can be as low as 1nA.<sup>12</sup> The spectral response of a typical silicon photodiode is shown in Figure 2-3.

In addition to higher quantum efficiency (hence better energy resolution), photodiodes have the following advantages over photomultiplier tubes for use with scintillators in radiation detection: they consume less power; are more compact; more rugged; and are insensitive to magnetic fields. Also, because of the relatively small dimensions over which charges must move in these devices, their time response is comparable to that of conventional photomultiplier tubes.<sup>11</sup> However, silicon photodiodes have no amplification, so electronic noise is a serious issue. To minimize electronic noise the photodiode should have small capacitance and low dark current. The noise problems of silicon photodiodes on the low-energy border and the timing and radiation resistance problems on the high-energy border forces physicists and engineers to look for new types of photodiodes.

## Organic Materials

Organic electronic materials have many attributes that make them an attractive candidate material for photoconductors when compared with conventional inorganic photodiodes. This section discusses these advantages of organic materials as well as the effect radiation has on these materials for their intended use in radiation detection.

### Improvements Over Si Photodiodes

Organic electronic materials promise low cost processing over large areas and volumes. An external quantum efficiency of 83% has been demonstrated in polymer photodiodes.<sup>13</sup> Organic materials are available in a wide range of energy gaps so that organic photodiodes can be tailored to spectrally match specific scintillators. Larger gap (>2 eV) materials are available where thermal charge generation, and thus intrinsic dark current, is negligible at room temperature. Due to their low thermal charge generation, organic materials also have high bulk resistivities, which permit low capacitance interdigitated diode structures. Two-layer organic photodiodes are also possible, where the top thin layer is optimized to absorb the scintillator light, and the thick bottom layer is added to reduce capacitance. Organic materials have low dielectric constants, typically about 3 compared to 12 for silicon, which further decreases the capacitance of organic photodiodes relative to silicon. The lower capacitance of these photodiodes means they can be made into devices with either lower noise or larger area than silicon photodiodes. Conventional silicon photodiodes are expensive and limited to areas less than  $\sim 1 \text{ cm}^2$  because of noise considerations.

Typical materials used in organic photodiodes have mobilities of the order  $10^{-4} \text{ cm}^2/\text{Vs}$ . Figure 2-4 shows a chart of the mobilities of common organic materials. Organic materials with mobilities up to  $1 \text{ cm}^2/\text{Vs}$  are available for charge transport layers.

The main technical hurdle in developing multilayer organic photodiodes is the fabrication of relatively thick (~1 mm) films of relatively high mobility (~0.1 cm<sup>2</sup>/Vs) organic materials.

Consider a structure with a 0.1 μm thick absorbing layer with electron mobility 10<sup>-4</sup> cm<sup>2</sup>/Vs, and a 1 mm hole transport layer with hole mobility 1 cm<sup>2</sup>/Vs. If we apply 100 V to the device we get a field of 1 kV/cm across the device. Then it takes 100 μs to extract electrons from the thin layer and holes from the thick layer. The capacitance of this device is 2.6 pF/cm<sup>2</sup>, which is about an order of magnitude lower than current silicon photodiodes. Capacitance and noise considerations limit current silicon photodiodes to 1 cm<sup>2</sup> areas. The same considerations permit organic photodiodes up to 10 cm<sup>2</sup> areas.

### **Effect of Radiation on Organic Materials**

All scintillation and detection materials are subject to radiation damage effects when exposed over prolonged periods to high fluxes of radiation. The damage is most likely evidenced as a reduction in the transparency of an inorganic scintillator caused by the creation of color centers that absorb the scintillation light. A comprehensive review has been published of the effects of radiation damage in a number of common inorganic scintillators.<sup>14</sup>

Radiation can affect polymers themselves by: chain scission, a random rupturing of bonds, which reduces the molecular weight (i.e., strength) of the polymer; cross-linking of polymer molecules, which results in the formation of large three-dimensional molecular networks; or it can result from excitation or ionization of atoms. A *Gray* (Gy) is the SI unit of absorbed dose. Most polymer derivatives can withstand 50kGy without damaging effects, where emissions at toll plazas are on the order of μGy.

Polymer photoconductors are not yet widely in use, so no research has been done on the effect of radiation specifically on photoconductors. However, there have been studies done on the effect of radiation on organic-based scintillators. Because of the widespread application of plastic scintillators in particle physics measurements, where they may be exposed to sustained high levels of radiation, considerable attention<sup>15-17</sup> has been paid to the degradation in the scintillation output of plastics due to radiation damage. The process is a complicated one, and many variables such as the dose rate, the presence or absence of oxygen, and the nature of the radiation play important roles and mainly affect the light output of the scintillator.

### **Interdigitated Structure**

As opposed to more common sandwich-style vertical transport devices, the devices in this study have lateral transport of the charge carriers. The electrodes are interdigitated (interwoven, as the fingers of two hands that are joined). These structures have the advantages of low capacitance, and the possibility of manufacturing using large area low cost printing techniques. The capacitance of interdigitated diode structures with 10  $\mu\text{m}$  wide electrodes with 20  $\mu\text{m}$  center-to-center spacing is about 0.2  $\text{pF}/\text{cm}^2$ . This is about 2 orders lower than the capacitance of typical silicon photodiodes. The main issue for interdigitated structures is the leakage current. The leakage currents for organic and silicon devices with the electrodes specified above, a 1  $\mu\text{m}$  film thickness, an applied voltage of 100 V, and a bulk resistivity of  $10^{13} \Omega$  for organics, and  $10^5 \Omega$  for silicon are 20  $\text{pA}/\text{cm}^2$  for organics and  $2\text{mA}/\text{cm}^2$  for silicon. This high leakage current makes interdigitated silicon photodiodes impractical but the 8 order of magnitude smaller leakage current for the organic is acceptable. The response time of

these organic interdigitated structures will be 400  $\mu\text{s}$  for materials with mobility  $10^{-4}$   $\text{cm}^2/\text{Vs}$ , and 400 ns for materials with mobility  $10^{-1}$   $\text{cm}^2/\text{Vs}$ . Kudo, et al. did a study on the operational characteristics of lateral and vertical type organic Field Effect Transistors (FETs) and found that both types of devices showed field effect characteristics and reported on their performance.<sup>18</sup>

The main technical hurdle for interdigitated diode structures is producing both high mobility organic films for reasonable response times and high quantum efficiency for energy resolution. High mobility films ( $>0.1$   $\text{cm}^2/\text{Vs}$ ) are typically well ordered. Incorporation of additional components will tend to disrupt this order, reducing mobility, so organic materials need to be chosen carefully. All of the factors in the sections above help describe why replacing the photomultiplier tubes in scintillators with photoconductors would be a good choice to help improve the portability of radiation detectors.

Table 2-1. Properties of some commercially available organic and inorganic scintillators

Material	Wavelength of Max Emission (nm)	Refractive Index	Light Output (% relative to Anthracene)	Abs. Light Yield (photons/MeV)	Reference
<b>Organic</b>					
Anthracene (crystal)	447	1.62	100		11
EJ-212 (plastic)	423	1.581	65		11
EJ-240 (plastic)	428	1.58	41		11
NE102A (plastic)	423	1.58		10 000	11
EJ-301 (liquid)	425		78		11
EJ-305 (liquid)	425		80		11
<b>Inorganic</b>					
NaI (Tl)	415	1.85		38 000	19
CsI (Tl)	540	1.80		65 000	20,21
CsI (Na)	420	1.84		39 000	22
Li(Eu)	470	1.96		11 000	23
YAG	550	1.82		17 000	24

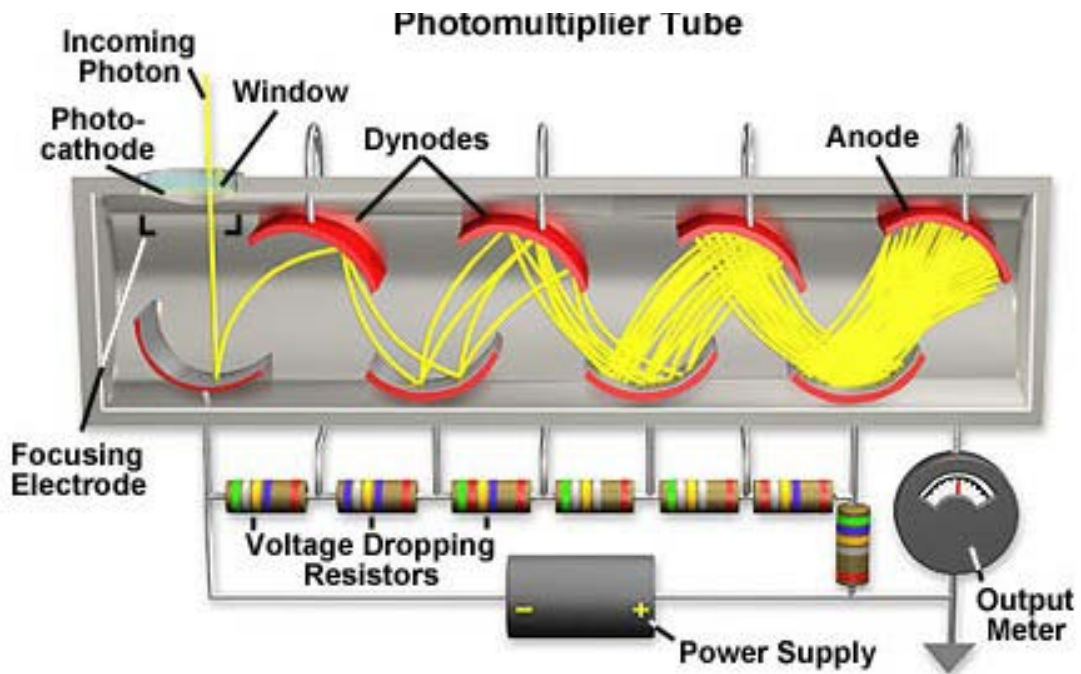


Figure 2-1. Schematic diagram of photomultiplier tube.<sup>25</sup> Photomultiplier tubes detect low levels of electromagnetic radiation (usually visible light or infrared radiation) and amplify it to produce a detectable electrical signal.

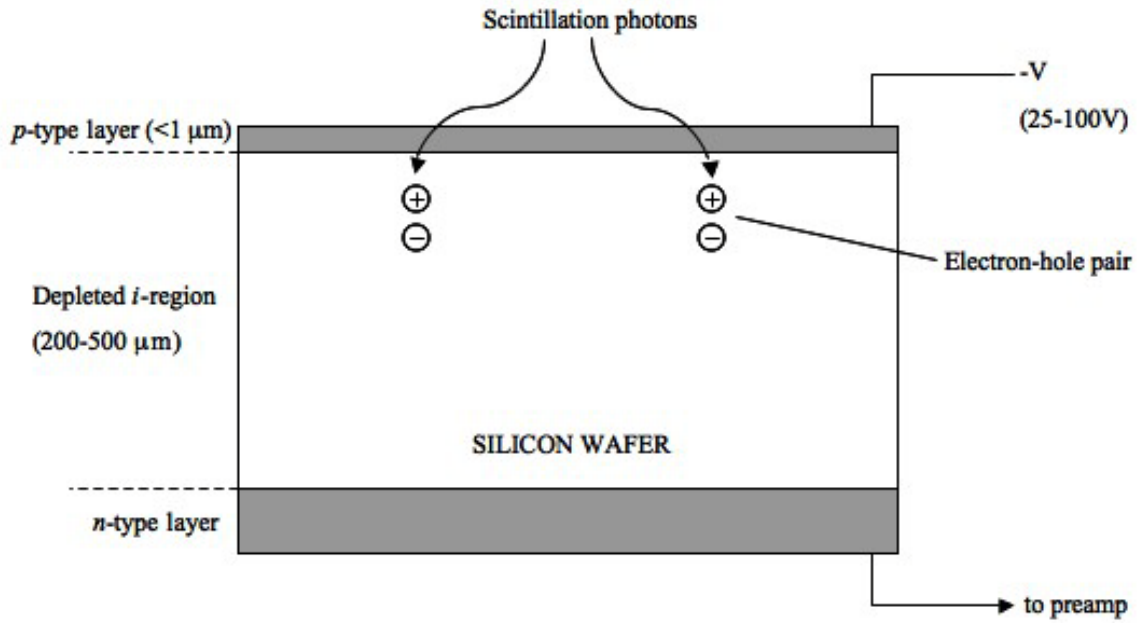


Figure 2-2. Basic configuration of a conventional photodiode.

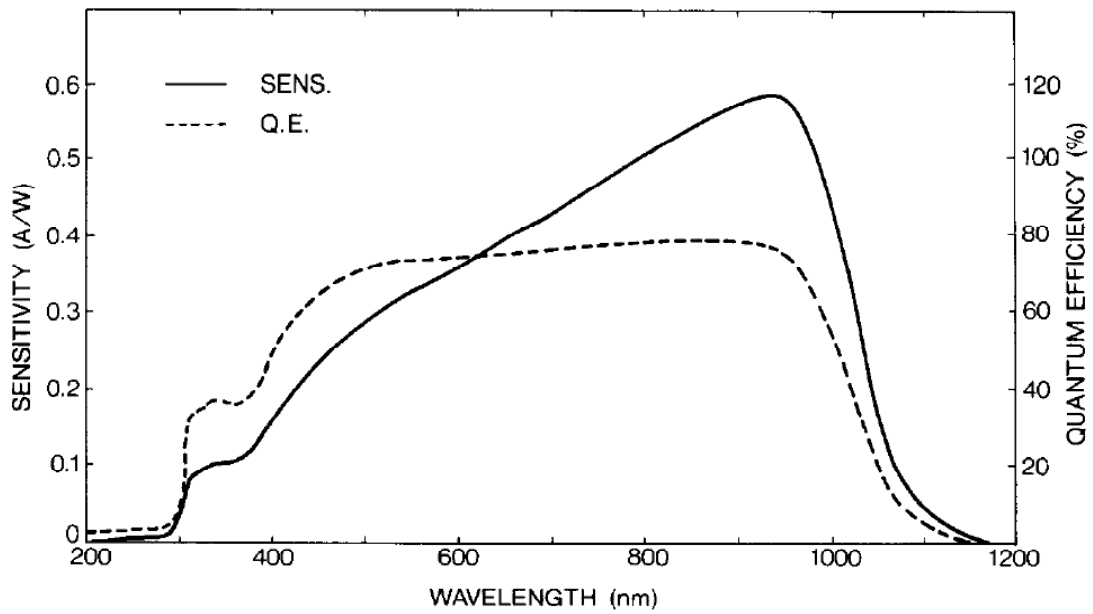


Figure 2-3. Spectral response of a typical silicon photodiode<sup>26</sup>

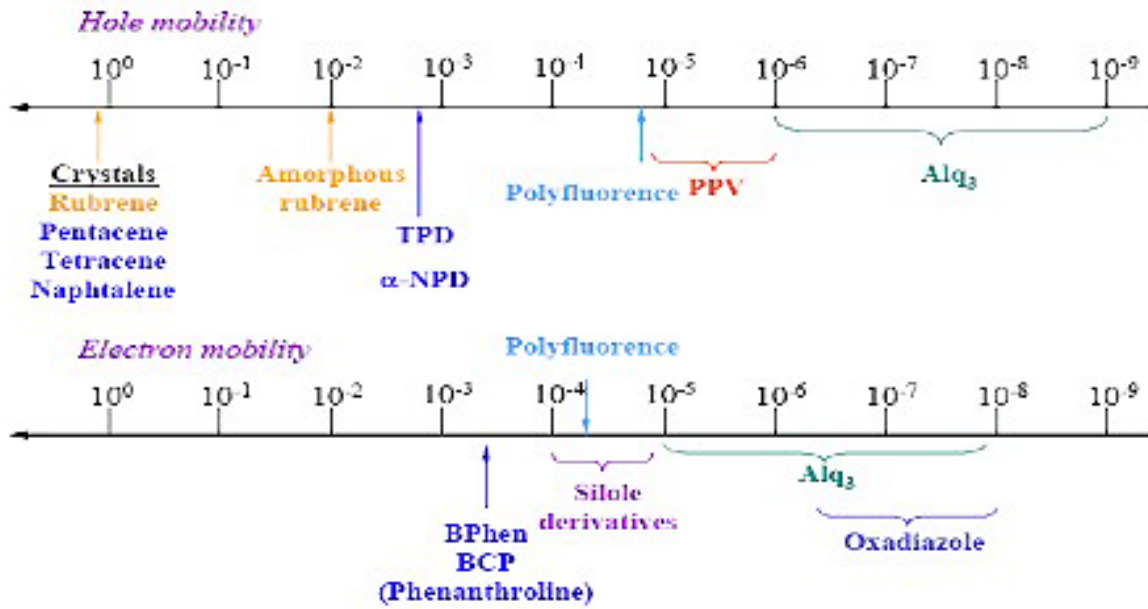


Figure 2-4. Mobilities of common organic materials (cm<sup>2</sup>/Vs)

## CHAPTER 3 THEORETICAL BACKGROUND

Before effective devices for the application can be discussed, it is necessary to have a fundamental comprehension of how these devices work. To have a better understanding of the organic materials used in making the photoconductors, this chapter will discuss charge transport in semiconducting and conducting polymers and the differences between bulk and planar heterojunctions in organic devices.

### **Semiconducting and Conducting Polymers**

It has been known for approximately 60 years that the electric conductivity of conjugated polymer chains is orders of magnitude higher than that of other polymeric materials.<sup>27</sup> A polymer chain is conjugated when it consists of alternating single and double carbon-carbon bonds. The mechanisms for charge transport in conjugated polymers are completely different than the transport mechanisms of conventional metallic conductors and inorganic semiconductors. In non-organic semiconductors, the materials are usually solid and therefore have a high degree of periodicity. In these materials, current conduction occurs via mobile or "free" electrons and holes, collectively known as charge carriers, which move freely on a background lattice of atomic nuclei. Polymer solids, on the other hand, are largely amorphous, and charge carriers travel more easily along polymer chains, rather than from chain to chain.

### **Band Theory**

According to the classical band theory, a solid that has a certain number of bands of energy that are completely filled with the other bands completely empty and a very large bandgap, is an electric insulator.<sup>28</sup> The effective number of free electrons is different from zero in a solid containing an incomplete energy band, and in this case the

solid has metallic character. At 0 K, the solid is in the lowest state of energy; but as the temperature increases, some electrons of higher energy in the filled band are excited into the next empty band and electronic conduction becomes possible.<sup>29</sup> For intrinsic semiconductors like silicon and germanium, the Fermi level is essentially halfway between the valence and conduction bands. Although no conduction occurs at 0 K, at higher temperatures a finite number of electrons can reach the conduction band and provide some current. In doped semiconductors, extra energy levels are added. This increase in conductivity with temperature can be modeled in terms of the Fermi function, which allows one to calculate the population of the conduction band. A similar phenomenon happens in conjugated polymers.

The origin of the band gap in conjugated polymers is best understood in terms of the bonding and anti-bonding of carbon-carbon double bonds. In these compounds, electrons are delocalized from their parent atoms and form two molecular orbitals of different energies, which act as a highest occupied molecular orbital (HOMO, “valence band”) and a lowest unoccupied molecular orbital (LUMO, “conduction band”). Carbon-carbon double bonds are formed when two of the three 2p orbitals on each carbon atom combine with the 2s orbital to form three  $2sp^2$  hybrid orbitals. These lie in a plane directed at  $120^\circ$  to each other, and form  $\sigma$  molecular orbitals with neighboring atoms. The third p orbital on the carbon atom, the  $2p_z$ , points perpendicularly to this plane, and overlaps with a  $2p_z$  orbital on a neighboring carbon atom, to form a pair of  $\pi$  bonding and  $\pi^*$  antibonding molecular orbitals (Figure 3-2). As equivalent  $\pi$  orbitals are formed between nearby atoms along the chain, the wavefunctions overlap, resulting in a delocalization over the polymer chain.

Poly(p-phenylene vinylene) or PPV and its derivatives (Figure 3-3) have been the basis for much of past research in semiconducting polymer devices. The bandgap of this polymer can be altered by adding different side groups to the polymer, which can push (or pull) charges to (or from) the backbone. Another duty of side chains is an improved solubility. Compared to the basic PPV, the solubility for MEH-PPV has been improved and the color has been shifted from yellow to orange by adding an appropriate side chain.

### **Hopping Conduction**

The band theory model fails as a model for charge transport if the bandwidth becomes too small and the mean free path of the charge carriers becomes comparable to the lattice spacing. In this situation, charge transport is possible through hopping conduction. In this case, charges are moved between localized states by thermal excitation. Such conduction requires the electrons to execute discrete jumps across an energy barrier and through space from one site to the next (see Figure 3-4). An electron may either hop over or tunnel through the barrier. Whether an electron uses one mechanism or the other depends on the shape of the barrier, the separation of the sites and the availability of thermal energy. To hop between sites the electron must have enough thermal energy to pass over the barrier. To tunnel between the sites, an electron must be small enough for the tail of the electron wavefunction to extend through the barrier. This thermally activated type of mobility will increase with temperature, which does not happen with the band theory mechanism of charge transport.

## Charge Carriers

One way to explain transport in semiconducting and conducting polymers is to discuss the carriers responsible for conduction. In this section, excitons, polarons, and solitons will be discussed.

Excitonic effects are well known in many solid-state systems and were well studied before electroactive polymers were investigated. In solid-state semiconducting crystals, excitons are electron-hole pairs that are bound together by their Coulombic interaction. Excitons are localized, but mobile, excited electronic states. Since they consist of a bound electron and hole, they cannot by themselves transport charge, but excitons can generate unbound carriers through several mechanisms. They can be formed by photons incident on the photosensitive layer or by coupling of opposite charges traveling through an electroluminescent device. The energy required to create them is less than the band gap. They may travel freely through the material transporting excitation energy, but not charge, as they are electrically neutral.

The concentration of dopant governs the conductivity of conjugated polymers, Charge doped into a polymer is stored in novel states such as polarons and solitons.<sup>29</sup> A polaron arises from the interaction between a charge carrier and the deformation of the lattice induced by this charge.<sup>30</sup> The concept of a polaron was first introduced in the case of ionic crystals<sup>31</sup>, and has been extended later to molecular crystals<sup>32</sup> and conjugated polymers<sup>33</sup>. In metals, the free electrons are polarized by the added charge so the effect on the crystal lattice is minimal. However, in intrinsic semiconductors there are far fewer free charges available to compensate for the effect of an added charge, so there is some polarization of the lattice. The effects will be small if the carrier is in a wide band (small effective mass and high velocity). The effects will be larger if the

carrier is in a narrow band (large effective mass and low velocity), if the lattice is polar (ionic), or if the carrier is localized in a trap. In these cases the lattice around the carrier is polarized and the carrier and the distortion to the lattice (or chemical structure, in polymers) move together. This distortion is termed a “polaron.”<sup>34</sup> Another state that can be present in intrinsic semiconductors is called a bipolaron. According to theoretical models<sup>35,36</sup>, a bipolaron is formed from the exothermic reaction of two polarons on the same chain.

Another way to portray the way charge is stored in a doped polymer is described by the motion of a solitary wave, called a soliton. Charged solitons explain the spinless transport observed in polymers with degenerate ground states, because they carry charge but not spin. Solitons can be negative, neutral, or positive in charge. The energy of solitons and the distortion of the sigma-bond framework have been estimated by quantum mechanical treatments using Hückel-type descriptions of  $\pi$  electrons.<sup>35</sup> High doping in some polymers causes the soliton energy levels essentially to overlap the filled valence and empty conduction bands, leading to a conducting polymer.<sup>37,38</sup>

### **Transport Mechanisms in Conjugated Polymers**

Figure 3-5 shows an example of how a charge carrier would move along a polymer chain, using polyacetylene as an example. Here, the charge carrier is not thought of as simply a hole or electron, but as a distortion to the local chain geometry with a net overall charge that is transferred along the chain. The charge carrier consists of a two-bond length long alteration to the chain geometry. This charge carrier, known as a (negative) soliton is transported along the chain by flipping back and forth of the single and double bond locations, as illustrated in Figure 3-5. The real mechanism differs from the schematic representation, as the bonds in conjugated systems are

delocalized over a certain length. Delocalized electrons are electrons in a molecule that are not associated with a single atom or to a covalent bond. They are contained within an orbital that extends over several adjacent atoms, making the whole molecule more stable. Double bonds represent regions of high electron density. Fluctuations in electron distribution can initiate a local bond flipping, which can travel along the polymer chain.

### **Bulk vs. Planar Heterojunctions**

Figure 3-6 depicts conceptually the photoinduced charge transfer in bilayer and bulk heterojunction structures. In the bilayer structure, where the electron donor (p-type hole conducting polymer) and electron acceptor (n-type electron conducting fullerene) form a well-defined planar interface by sequential deposition or spincoating of the organic layers, the external quantum efficiency and photocurrent are limited primarily by the exciton lifetime before photoexcited excitons recombine or dissociate into free charge carriers at the donor-acceptor interface. Therefore, the device thickness should be kept within the exciton diffusion length of the active polymer material for efficient charge transfer. On the other hand, in the bulk heterojunction device, the donor-acceptor interface is distributed over the entire active layer structure because both donor and acceptor materials are co-evaporated or blended in solution. Therefore, the interfacial area is increased by a large extent such that the dissociation site at a donor-acceptor interface falls within a distance closer than the exciton diffusion length from an each absorbing site. For this reason, the charge generation efficiency in the bulk heterojunction structure has the potential to be near 100%. However, in such a blended structure, efficient charge transport to the electrodes is sensitive to the nanoscale morphology of the mixture because it requires an interpenetrating network to provide pathways for the hole and electron conducting paths to reach the opposite contacts.

Nanomorphology is dependent on many parameters: the evaporation rate, substrate temperature during vacuum deposition process, specific solvents used and solvent evaporation time for solution process like spin-casting, and the annealing condition and relative concentration of the mixture for both processes.<sup>39</sup> It should be noted that charge transport in actual devices can be much more complicated than the continuous conducting paths as illustrated in Figure 3-6 B.<sup>40</sup>

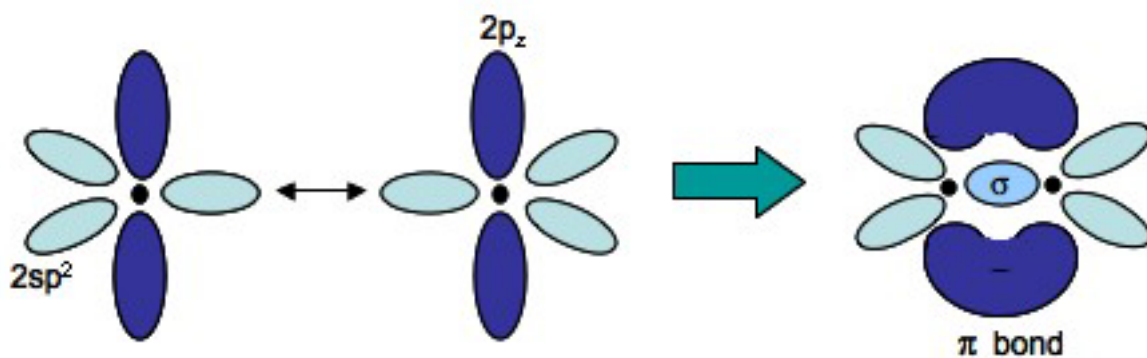


Figure 3-1. The overlapping of  $2sp^2$  and  $2p_z$  orbitals forms  $\sigma$  and  $\pi$  bonds respectively

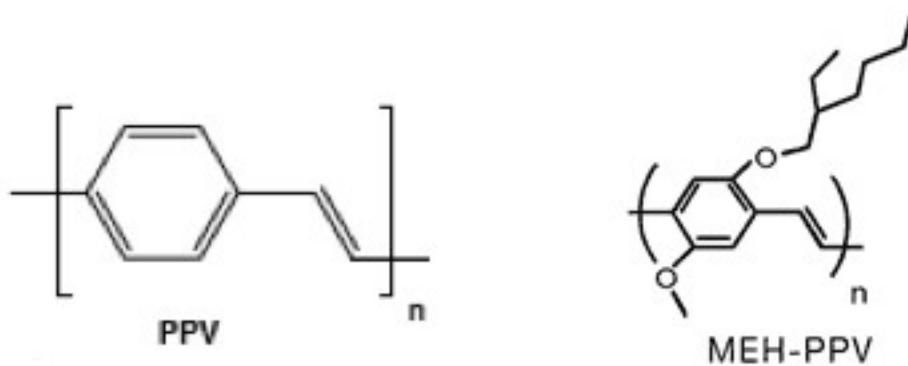


Figure 3-2. Structure of two typical polymers where the backbone is conjugated (double and single bonds alternate)

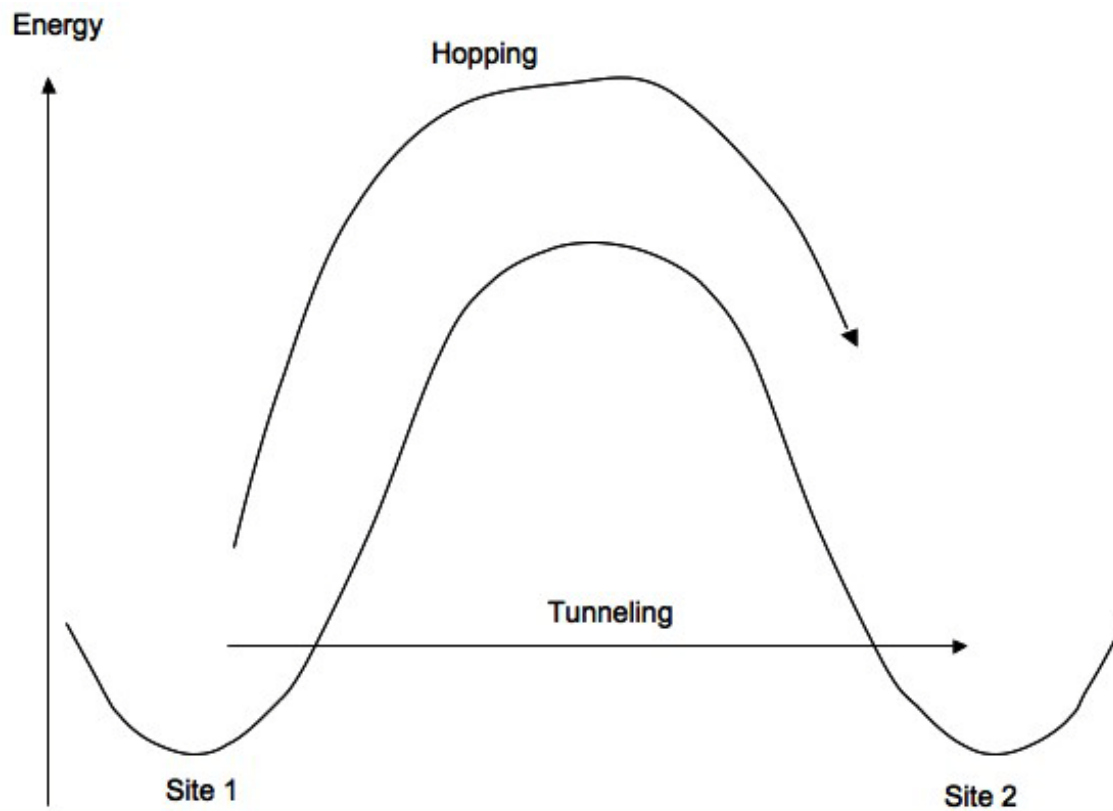


Figure 3-3. Diagram of electron transfer mechanisms between adjacent sites separated by a potential-energy barrier

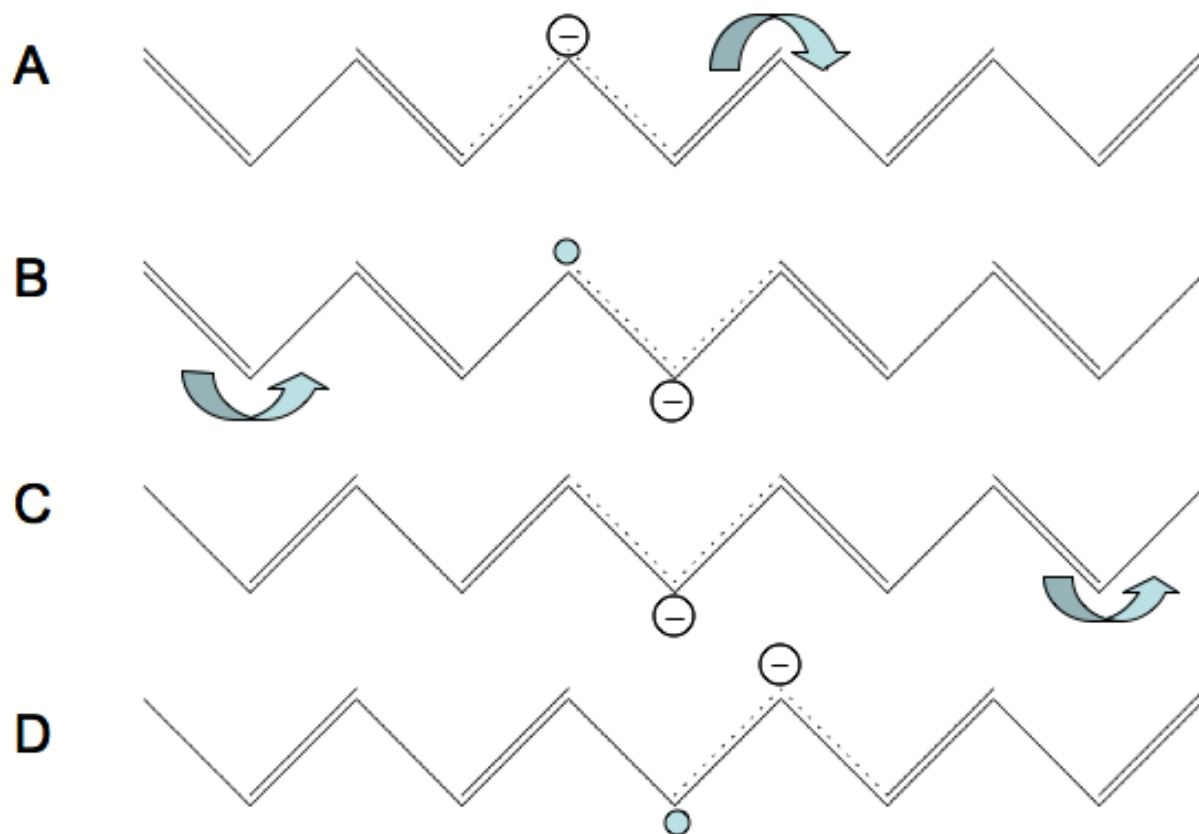
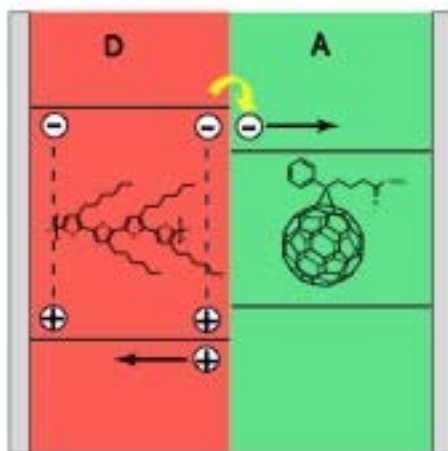
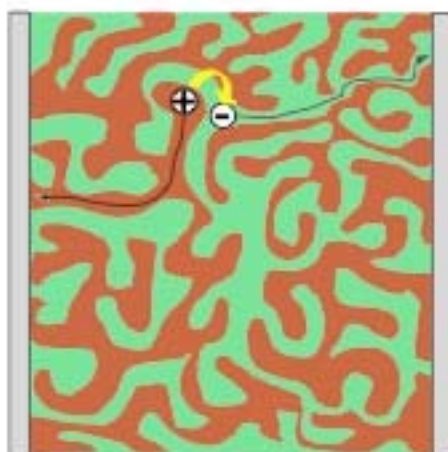


Figure 3-4. Schematic illustration of an electron moving along a polymer chain where double bonds flip back and forth to accommodate its passage



A. Bilayer heterojunction



B. Bulk heterojunction

Figure 3-5. Schematic diagram depicting conceptually the photoinduced charge transfer in A) bilayer heterojunction and B) bulk heterojunction. In a bilayer structure, the electron donor and electron acceptor form a well-defined planar interface by sequential deposition or spin-casting. In a bulk heterojunction, the donor-acceptor interface is distributed over the entire active layer structure and its interfacial area is increased by a large extent because both the donor and acceptor materials are co-evaporated or blended in solution

## CHAPTER 4 BULK HETEROJUNCTION

In this chapter, we study photoconductors designed to replace photomultiplier tubes in scintillator readout in radiation detection devices. The specific materials were chosen because they absorb light within the range of scintillator output, and bulk heterojunction devices were chosen because they are easily fabricated by spin-coating. High quantum efficiency is a critical parameter for photoconductors for radiation detection, and requires efficient exciton dissociation, separation of charges into distinct transport manifolds, and collection of these charges without their recombining. A quantitative understanding of exciton dissociation, charge separation, and transport is necessary to enable design of optimum organic photoconductors.<sup>41</sup> Devices were optimized by measuring the effects of polymer film thickness, polymer ratio, interdigitated finger spacing, and applied field on quantum efficiency. These studies allow us to discern which steps in the photoconducting process limit the quantum efficiency.

### **Device Structure and Operation**

We have investigated photoconductivity in interdigitated lateral photoconductors with oxidized aluminum contacts, and a poly[2-methoxy-5-(2-ethylhexyl-oxy)-1,4-phenylene-vinylene] [MEH-PPV] / {6}-1-(3-(methoxycarbonyl) propyl)-{5}-1-phenyl-[6,6]-C61 [PCBM] blend as the active layer. Both materials were obtained from American Dye Source. The devices consist of aluminum interdigitated fingers on top of a silica substrate with a polymer coating over the aluminum electrodes. A schematic of the device is shown in Figure 4-1, and a picture of an actual device is shown in Figure 4-2. The device fabrication and measurement is described in the following section.

In order to discuss the operation of these devices, an in-depth review of the organic materials used in the devices is necessary. Organic materials have the advantages of being low-cost and easily processable and are therefore an attractive material candidate for this project; however, there is some optimization that needs attention. The two organic materials chosen for this study are MEH-PPV and PCBM. Their structures and band diagrams are found in Figure 4-3. The MEH-PPV absorbs the exciton, which dissociates into an electron-hole pair. Then, the electron is transferred to the PCBM because it is at a lower Lowest Unoccupied Molecular Orbital (LUMO) energy level, thereby separating the electron-hole pair. The electron is then transported to the electrode in the PCBM, and the hole is transported to the electrode in the MEH-PPV.

There is an optimum ratio of the two organic compounds. The ratio controls the relative interface surface that is present between the two species in an interpenetrating network. There needs to be enough MEH-PPV to absorb the maximum amount of photons, but if there is too much there will be no PCBM near enough to grab the electron. Also, there needs to be a large amount of PCBM readily available to dissociate the electron-hole pair. The photoconductor issues of absorption, exciton dissociation, avoiding recombination, and charge extraction will be taken into account when developing the optimum ratio of these compounds. Figure 4-4 also shows the effect of the interpenetrating network of the organic compounds. In this diagram, the MEH-PPV is represented by the white areas (hole-transporting material) and PCBM is represented by the grey areas (electron transporting material). The transport materials carry the electrons or holes to their respective electrode.

The devices in this study are made to be used with scintillators and will convert their light output into an electronic signal. For this purpose, the polymers chosen for fabrication must absorb light within the visible range (400-700nm). A polymer solution of MEH-PPV and PCBM was chosen for this experiment because it fits the material requirements for high efficiency photoconductors. The absorption spectrum for the polymer solution with at 1:2 weight ratio of MEH-PPV:PCBM is shown in Figure 4-5. The bulk of the absorption is in the wavelength range of 400-700nm, which is the visible spectrum. The peak is around 525nm.

### **Device Fabrication and Measurement**

The first step in the fabrication process for the interdigitated devices is photolithography. Aluminum was thermally evaporated over the photoresist on the glass substrates to a thickness of 100 nm. The spacing between electrodes is either 5  $\mu\text{m}$  or 10  $\mu\text{m}$ , with electrode widths of 25  $\mu\text{m}$  or 50  $\mu\text{m}$ , respectively. The interdigitated electrodes cover an area of 3 mm x 3 mm. A picture of the layout of the devices is shown in Figure 4-1. Second, after lift-off, the electrodes were placed in an oxygen plasma for 2 minutes to form an oxide layer. Aluminum is a blocking contact for MEH-PPV, and by oxidizing it we further reduce electrical injection of carriers.<sup>42</sup> The MEH-PPV:PCBM active layers were spun cast at 400 rpm from a chlorobenzene solution with 5 mg MEH-PPV, and 5 $\times$ N mg PCBM per 1 mL chlorobenzene for the 1:N ratio films. Active layers were about 165 nm thick. Samples for absorption measurements were spun cast at 2000 rpm from solutions of (5 mg MEH-PPV + 15 mg PCBM) / mL chlorobenzene; 5 mg MEH-PPV / mL chlorobenzene; and 15 mg PCBM / mL

chlorobenzene, to form 60 nm, 35 nm, and 25 nm films respectively. After spin casting, the samples were heated to 120°C for one hour to remove solvents.

Next, the samples were loaded into a vacuum cryostat and measured at room temperature. Dark current and capacitance measurements were taken for all devices. Dark currents were typically in the  $10^{-7}$  A range and the capacitance of the devices were 6 to 12 pF. An example of a typical I-V curve with no light applied to the device is shown in Figure 4-6. Photoresponse measurements were also taken. Samples were illuminated from the substrate side with optically chopped light from a monochromator. The incident illumination was measured with a calibrated Newport 818UV photodiode. A schematic drawing of the setup for quantum efficiency measurements is shown in Figure 4-7. External quantum efficiencies were corrected for the shadowing of light by the electrodes, but not for reflections or incomplete light absorption.

### **Device Optimization**

The design of the device also has an effect on the quantum efficiency. As previously discussed, there needs to be sufficient interpenetrating networks of the organic materials. The blend ratio affects the absorption of the photons, dissociation of the excitons, as well as charge separation. There needs to be an optimum amount of MEH-PPV present to absorb the photons and for hole collection, as well as an optimum amount of PCBM for exciton separation and electron collection. Other aspects of the device can also be optimized to improve performance. The interdigitated fingers are made of aluminum, and their thickness (height), width, and spacing between them can all affect the charge transport properties of the device. If the fingers are spaced further apart, the charge carriers have to travel a longer distance and therefore are more

susceptible to falling into traps, which affects the charge collection efficiency. The thickness of the polymer film will change the absorption properties. The voltage applied to the devices can be varied to change the electric field that the charge carriers are moving in, which affects the charge transport properties.

### **Effect of Polymer Film Thickness**

The thickness of the polymer film was studied for several devices with similar polymer ratios, mask spacing, Al thickness, and applied voltage. The film thickness affects the film structure and the absorption of photons. The thicker the film, the more light is absorbed. Figure 4-8 shows the quantum efficiency vs. wavelength for three different film thicknesses. Quantum efficiency is defined as the electrons collected per photons incident. It was found that for thin films, the quantum efficiency roughly follows the absorption spectrum. One important feature of organic materials is that the materials can be chosen so that the peak of their absorption can be matched to a specific type of scintillator if desired.

### **Effect of Polymer Ratio**

The polymer ratio refers to the amount of MEH-PPV (poly[2-methoxy-5-(2'-ethylhexyloxy)-*p*-phenylene vinylene) as compared to PCBM ([6,6]-phenyl-C<sub>61</sub> butyric acid methyl ester) in a solution of chloroform. The ratios were based on the weight of the organic materials. The polymer ratio affects the absorption of the photons, dissociation of the excitons, as well as charge separation. There needs to be an optimum amount of MEH-PPV present to absorb the photons and for hole collection, as well as an optimum amount of PCBM for exciton separation and electron collection. It was found that the polymer ratio of 1:4 of MEH-PPV:PCBM gave the best quantum

efficiency of the ratios that were tested. These results are shown in Figure 4-9, which is a graph of quantum efficiency vs. wavelength for three different polymer ratios.

### **Effect of Interdigitated Finger Spacing**

Interdigitated finger spacings of 5 and 10  $\mu\text{m}$  were patterned and the quantum efficiency was measured. Scaling of the device properties can provide insight into the fundamental mechanisms in these devices. The spacing in between the fingers affects the trapping and the charge collection. The further the carriers have to travel between electrodes, the more likely they are to fall into a trap state, so less charges are collected. It was found that the mask spacing had only a small effect at the same field. This finding suggests that the quantum efficiency is limited by the exciton dissociation, not by charge trapping or carrier recombination (after the excitons dissociate and the charges separate).

Also, being able to use larger mask spacing (since there was no change in quantum efficiency for the same field) will make production cheaper, as the interdigitated fingers could be patterned using low-cost printing techniques as opposed to lithography. Devices with larger spacings also have lower capacitance. However, as you increase the distance between the electrodes, larger applied voltages are needed to maintain the same field.

### **Effect of Applied Field**

The voltage applied to the devices affects the charge transport properties as well as trapping. It was found that the quantum efficiency increased as the voltage increased. Also, the results under applied forward and reverse bias were similar (as expected) because both electrodes are aluminum. Applied field is the applied voltage divided by the spacing between the electrodes. It was found that the quantum efficiency

improves with increased applied field, with a maximum near 505 nm. These results are shown in Figure 4-10. As opposed to looking at the whole spectrum of the quantum efficiency at one applied field, Figure 4-11 shows the peak quantum efficiencies (measured at 505 nm) for varying applied fields. It was found that the quantum efficiency varies linearly with applied field, even for different electrode spacings.

### Data Analysis

Figure 4-12 shows the absorption spectra in arbitrary units of MEH-PPV, PCBM, a 60 nm thick 1:3 blend of MEHPPV:PCBM, and a fit to the 1:3 blend obtained from a linear sum of the MEH-PPV and PCBM absorption spectra. The absorption spectra of the MEH-PPV and PCBM shown in Figure 4-12 represent the contributions to the linear fit of the absorption of the blend for the wavelengths above the optical absorption gap shown in the figure. Below the optical gap one also expects weak absorption by charge transfer states that cause the linear fit to fail.<sup>43</sup> The absorption spectrum has a peak at 495 nm. The lowest unoccupied molecular orbital/ highest occupied molecular orbital levels of MEH-PPV and PCBM are 3.0/ 5.3 eV and 3.5/ 5.4 eV, respectively, so that MEH-PPV/PCBM interfaces form a type II heterojunction.<sup>44,45</sup> Excitons are formed both on the MEH-PPV and the PCBM and dissociate to form bound polaron pairs, with the electron polaron on the PCBM, and the hole polaron on the MEH-PPV. The precise mechanism for this dissociation is still in question.<sup>46,47</sup> The polaron pair is bound by their mutual Coulombic attraction and requires an electric field for collection.

Figure 4-13 shows the measured (solid lines) and fit (dashed lines) quantum efficiency versus excitation wavelength for 1:3 MEH-PPV:PCBM lateral devices with 5  $\mu\text{m}$  spacing between the 25  $\mu\text{m}$  fingers. The interdigitated fingers cover an area of 9

mm<sup>2</sup>. The capacitance of the devices is 6 pF for the 10 μm spacings and 12 pF for the 5 μm spacings. The excitation spot is approximately 1 mm x 2 mm, and is completely contained in the active area. The signal is independent of the location of this spot within the active area. The measured incident photon flux at 495 nm was 3x10<sup>13</sup> photons/sec. Assuming a carrier transit time of 1.0x10<sup>-6</sup> s and 100% internal quantum efficiency at 0.4 MV/cm, we expect a carrier population of 3x10<sup>9</sup> (number of carriers) in the illuminated area (2 mm<sup>2</sup>). The quantum efficiency has a peak at 495 nm, and increases with increasing applied bias. A variety of MEH-PPV:PCBM ratios were measured, the highest quantum efficiencies were found for ratios from 1:3 to 1:4. This is consistent with the results found for MEH-PPV:PCBM photodiodes.<sup>48</sup> Measurements were made for a variety of film thicknesses. For films less than the absorption length, the quantum efficiency followed the absorption spectrum. We fit the quantum efficiencies of the 165 nm thick devices with a linear combination of the absorption of MEH-PPV and PCBM films. The relative contributions of the two components are the same for all three fits, only the pre-factor is changed. From the absorption of 60 nm films we estimate that the 165 nm films absorb about 75% of the incident light at 495 nm; however, we do not correct for this in the quantum efficiencies.

The dependence of quantum efficiency on electric field could come from a variety of causes such as electronic traps or recombination centers in the active material. Both of these mechanisms will reduce the photocurrent in the device. These defects can be located either in the bulk of the active material or be located near the interface with the electrodes. If the defects are in the bulk of the active material we would expect the quantum efficiency to be lower for devices with wider electrode spacings for the same

applied field, because the carriers would have to sweep through a larger volume of material, and hence larger number of defects, as they sweep across the device. If the defects are located near the interfaces, they will introduce a given reduction in quantum efficiency at a given electric field. Devices with wider electrode spacing would then have more active area without defects, and hence higher quantum efficiency. If the field dependence of quantum efficiency is due to a problem with exciton dissociation or charge separation, then this should be independent of electrode spacing.

### **Onsager Model**

Figure 4-14 shows the quantum efficiency at 495 nm as a function of applied field for devices with 5  $\mu\text{m}$  spacing of 25  $\mu\text{m}$  wide electrodes, and for 10  $\mu\text{m}$  spacing of 50  $\mu\text{m}$  wide electrodes. The results are similar for both electrode spacings, so that charge traps or carrier recombination centers are not responsible for the field dependence. Separation of the dissociated charges that formed the exciton is likely responsible for the field dependence. When light is absorbed in the MEH-PPV:PCBM blend it forms excitons on the MEH-PPV and on the PCBM. These excitons quickly ( $<1$  ps) dissociate into a bound electron-hole pair, with the hole on the MEH-PPV and the electron on the PCBM.<sup>46</sup> A variety of models have been used to describe the electric field dependence of separating this bound electron hole pair. These models are modifications to the Onsager model of recombination of ions.<sup>49</sup> Onsager's model calculates the probability that a pair of oppositely charged ions will escape recombination by viewing this problem as one of Brownian motion under the combined action of the Coulomb attraction and the applied electric field. Recombination follows a Langevin form in Onsager's model.<sup>50</sup> Braun applied the Onsager theory to dissociation of charge transfer states in donor-

acceptor polymers by incorporating the finite lifetime of the charge transfer state to the model.<sup>51</sup> The Braun model model still incorporates a Langevin form for recombination and has been used successfully by several groups to describe photocurrent in organic systems.<sup>52-54</sup> Materials used for organic photoconductors, such as MEH-PPV/PCBM form bulk type II heterojunctions, and therefore introduce an energy barrier to recombination which is not included in the Langevin model. Recent results have shown that bimolecular recombination in these systems is over two orders of magnitude lower than predicted by the Langevin model.<sup>55</sup> In this study we use the Braun model, with a Gaussian distribution of initial charge separations, and a reduced Langevin recombination.

To explain the field dependence of the QE data shown in Figure 4-14, it was fit with Equation 4-1, where A is the percentage of incident light that is absorbed in the film,

$$QE = A \times P(T, E) \quad (4-1)$$

and P(T,E) is the probability that an exciton will dissociate and the constituent charges will separate and be collected by the field E. From the absorption data we find A = 75%. We assume that the excitons dissociate into bound electron hole pairs with an initial separation which follows a Gaussian distribution, shown in Equation 4-2.

$$P(T, E) = N_F \int P(x, T, E) F(x) dx \quad (4-2)$$

where:

$$N_F = 4/(\sqrt{\pi} a^3)$$

$$F(x) = x^2 e^{-x^2/a^2} \quad 51$$

A value of a = 1.3 nm was chosen for the fits.<sup>53</sup> The charge separation probability for an initial separation x is given by Equation 4-3.

$$P(x, T, E) = k_d(x, E) / (k_d(x, E) + k_F) \quad 51 \quad (4-3)$$

In this work we assume a carrier recombination rate of  $k_F = 1.0 \times 10^6 \text{ s}^{-1}$ .<sup>56</sup> The dissociation rate is given by Onsager's expression, shown in Equation 4-4.

$$k_d(x, E) = k_R \frac{3}{4\pi x^3} e^{-E_B/kT} \sum_{s=0}^{\infty} \frac{[2b(E)]^s}{s!(1+s)!} \quad (4-4)$$

where:

$$b(E) = \frac{q^3 E}{8\pi \langle \varepsilon \rangle \varepsilon_o k^2 T^2},$$

$$\langle \varepsilon \rangle = 4.5 \quad 57,58$$

$$k_R = \beta \frac{q \langle (\mu_e + \mu_h) \rangle}{\varepsilon_o \langle \varepsilon \rangle}$$

Previous workers have chosen  $\beta = 1$ , so that  $k_R$  represents Langevin recombination. Nunzi and coworkers have shown that the Langevin form overestimates bimolecular recombination in organic solar cells by over two orders of magnitude.<sup>55</sup> The parameters used to calculate  $P(T, E)$  are shown in Figure 4-14. The dotted line is calculated using  $\beta=1$ , the dashed line a fit to the data where  $\beta$  is the only variable. The fit value is  $\beta = 0.008$ , corresponding to significantly reduced recombination, consistent with previous experimental results.<sup>55</sup> Including realistic numbers for the recombination rate clearly improves the fit to the data, however, the fit still underestimates the data at higher electric fields. This may be due to the field dependence of the carrier mobilities, which was not included in this model.<sup>59</sup>

## Conclusions

Quantum efficiencies over 70% have been demonstrated in lateral interdigitated 1:3 MEH-PPV:PCBM based organic photoconductors, which makes this type of device a viable candidate for use in radiation detection applications. The absorption in the

MEH-PPV/PCBM films can be fit with a linear sum of the absorption of MEH-PPV and PCBM films. The quantum efficiency spectra follows the absorption spectra for films with optical densities less than one. The field dependence can be explained with a modified Onsager model for charge dissociation. With this deeper understanding of how the physical parameters of lateral interdigitated photoconductors effect quantum efficiency, a device that is optimized for radiation detection can be designed.

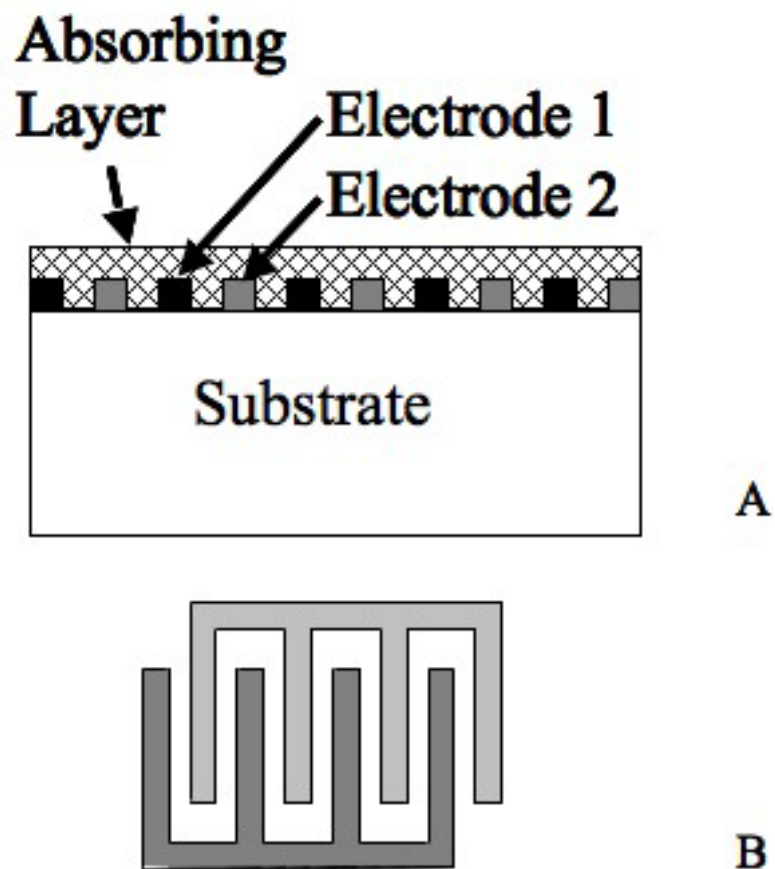
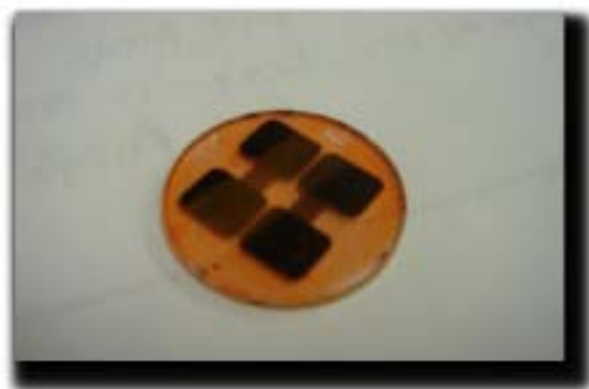


Figure 4-1. Schematic drawing of MEH-PPV/PCBM photoconductor devices. A) Side view of device with electrodes covered with a polymer (absorbing) layer. B) Top view of the interdigitated electrodes.



1 inch

Figure 4-2. Picture of MEH-PPV/PCBM device. The large outside squares are contact pads, and the two squares in the center are area with interdigitated fingers.

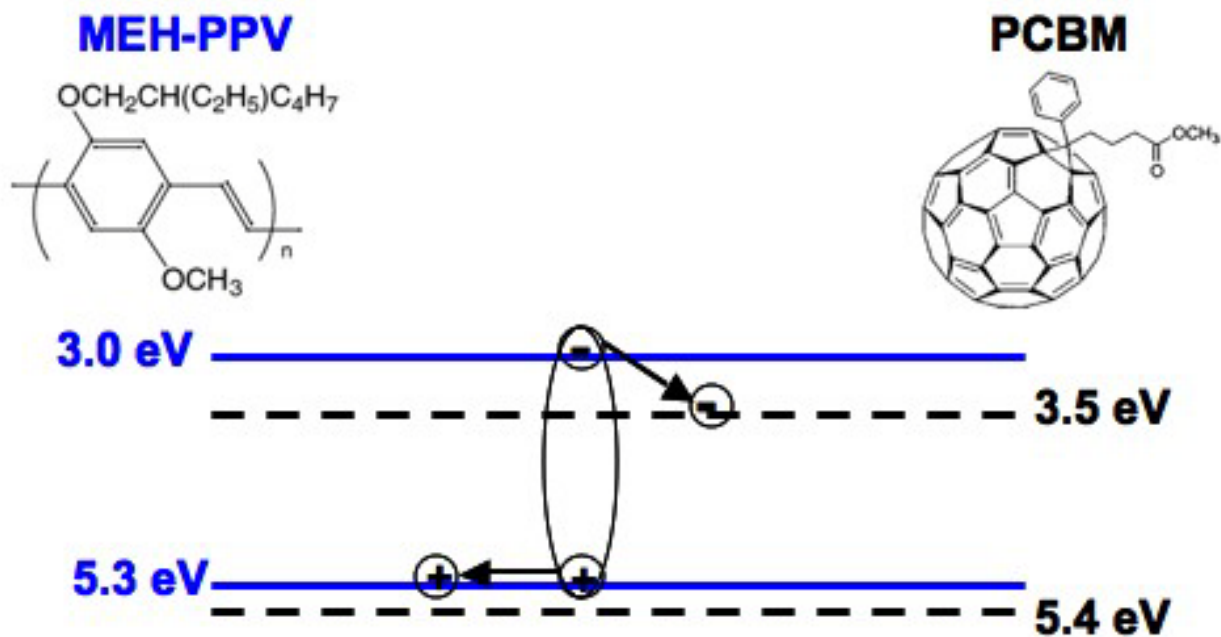


Figure 4-3. Energy band diagram for organic materials used in quantum efficiency study.

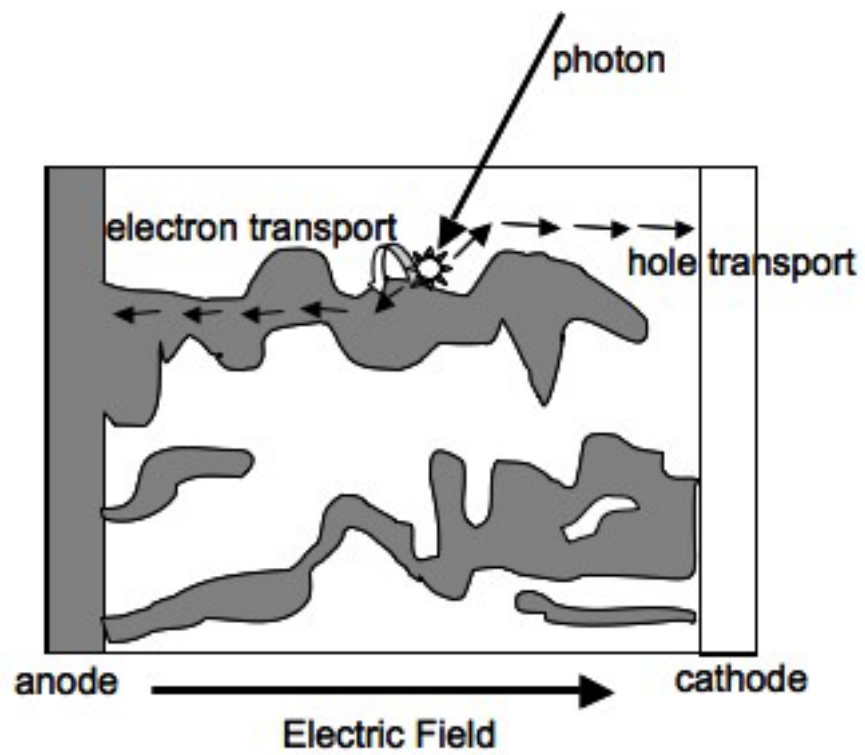


Figure 4-4. Interpenetrating organic networks. White: MEH-PPV, Grey: PCBM.

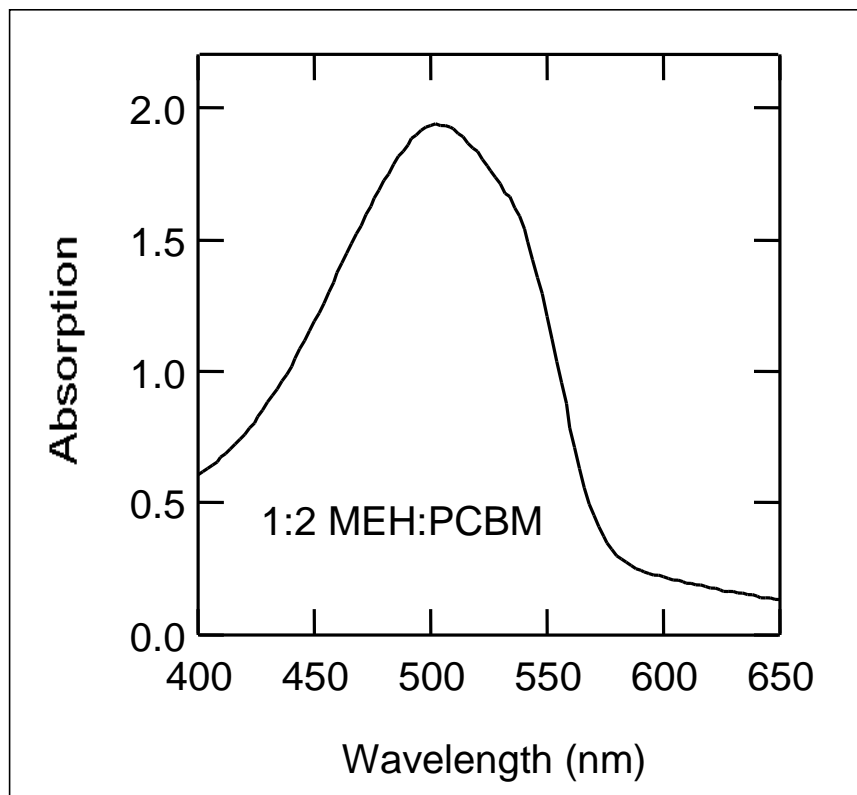


Figure 4-5. Absorption spectrum for MEH-PPV/PCBM polymer solution. The absorption peak is in the visible region.

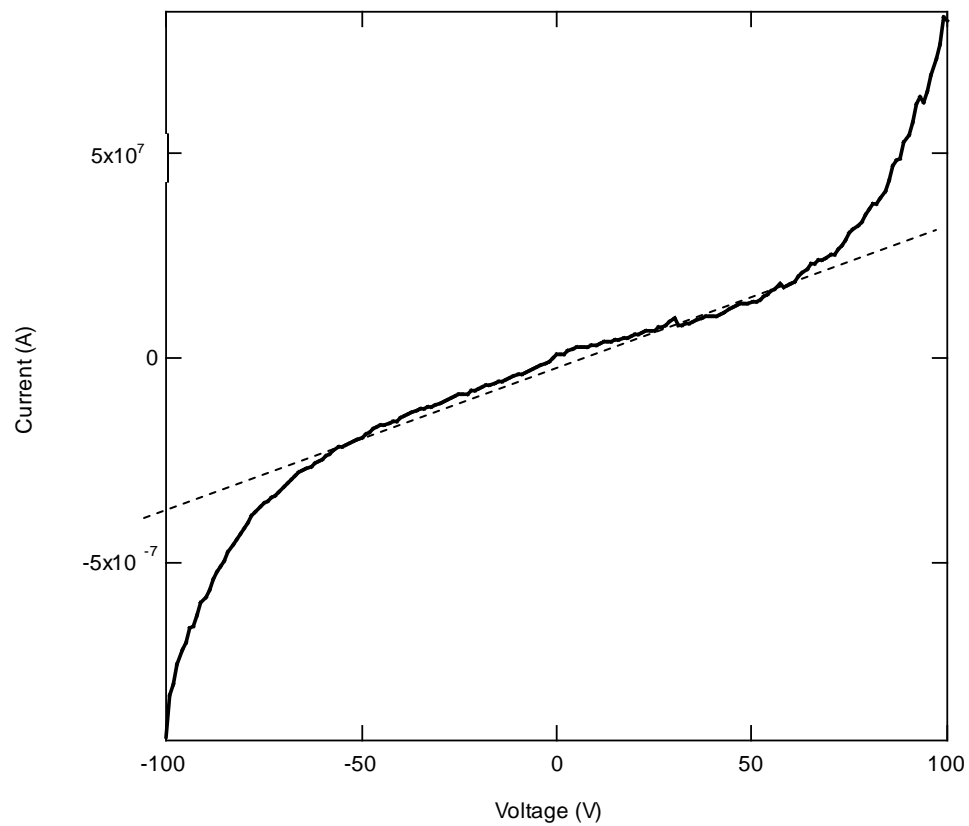


Figure 4-6. Typical dark current of MEH-PPV/PCBM interdigitated device

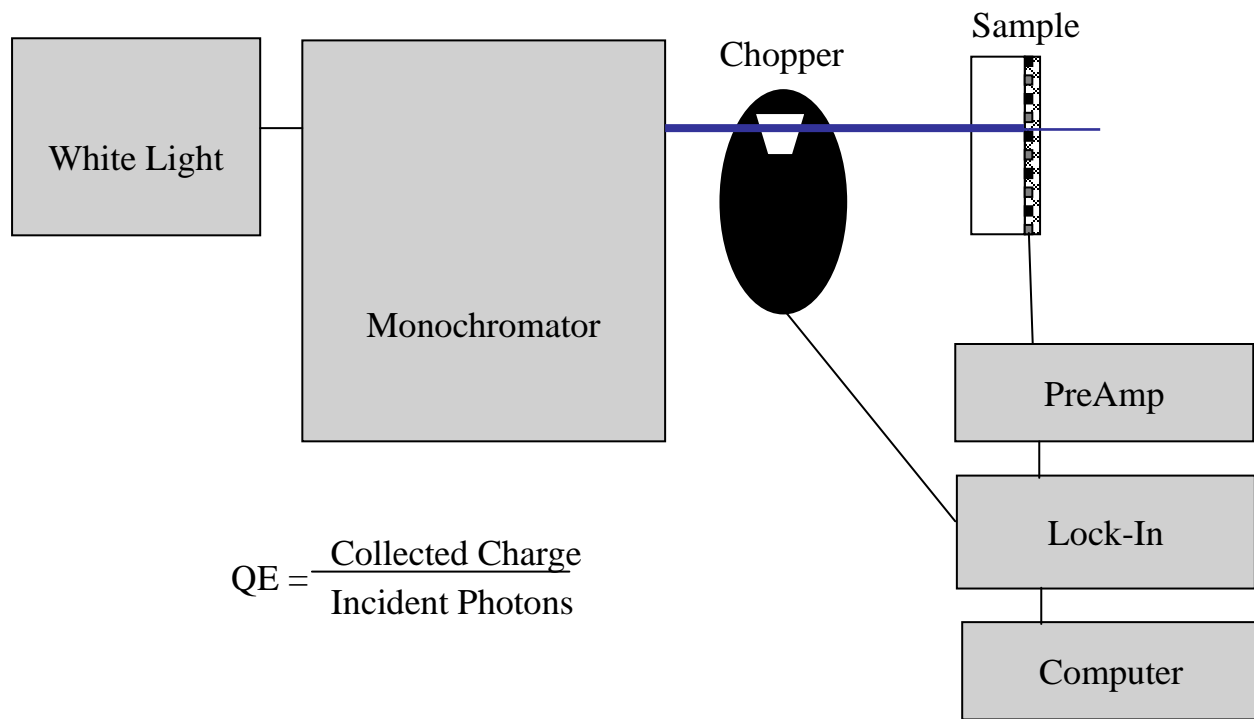


Figure 4-7. Schematic drawing of equipment setup for characterization of quantum efficiency.

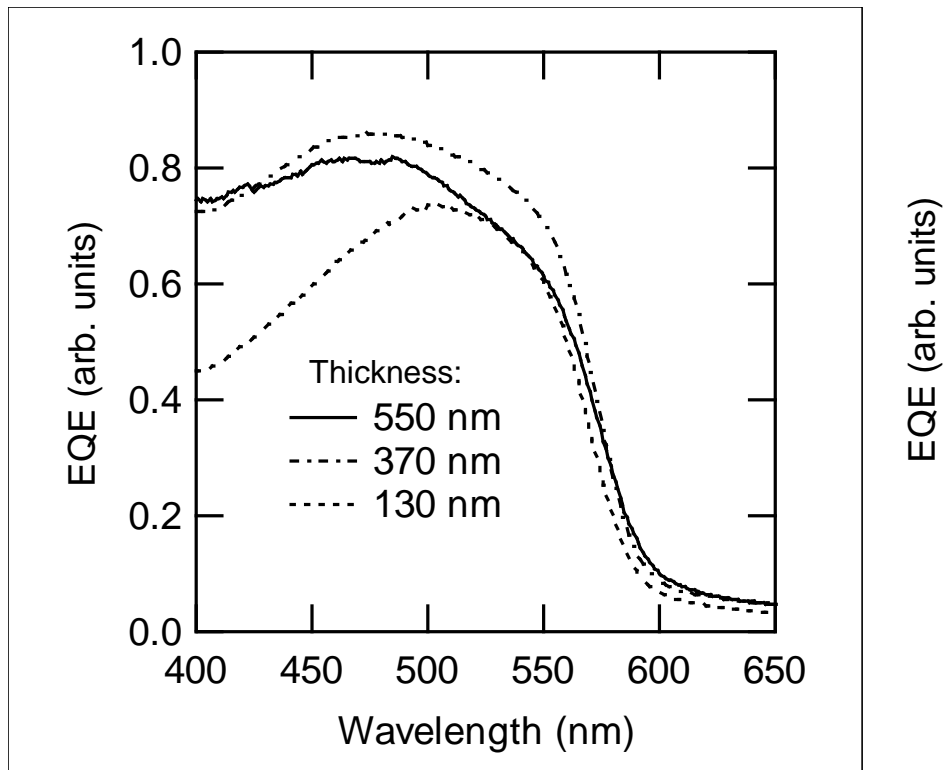


Figure 4-8. Effect of polymer layer thickness on quantum efficiency.

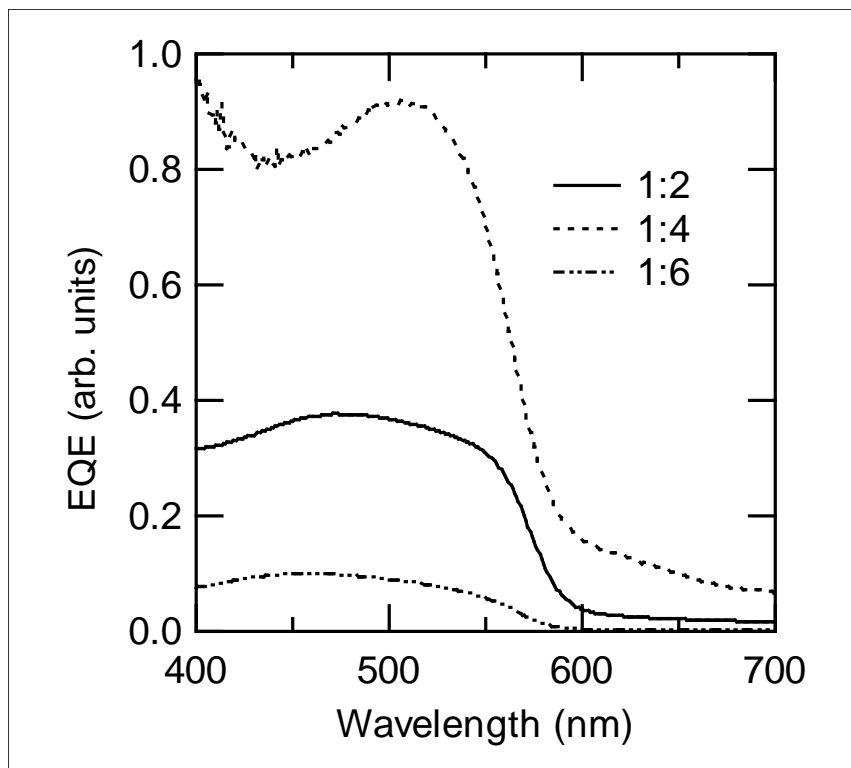


Figure 4-9. Effect of polymer ratio on quantum efficiency.

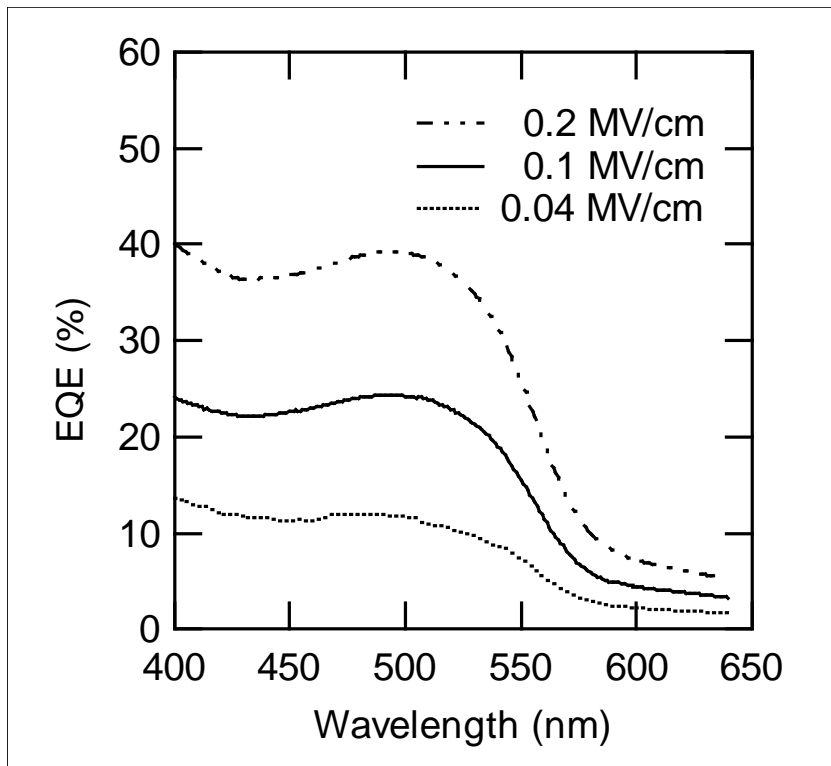


Figure 4-10. Spectral response of quantum efficiency as a function of applied field.

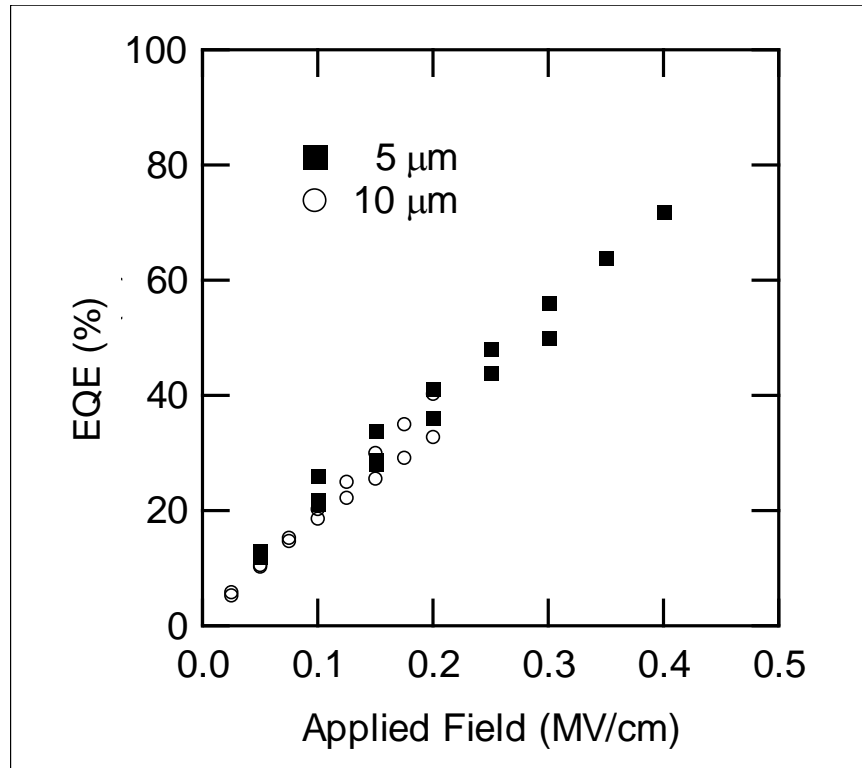


Figure 4-11. Effect of applied field on peak quantum efficiency.

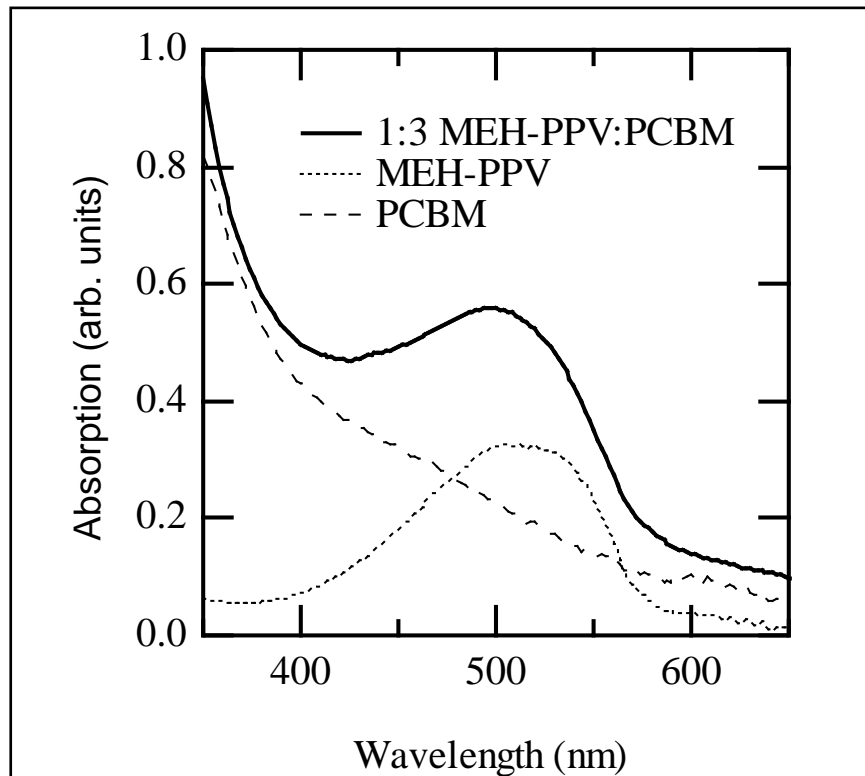


Figure 4-12. Absorption (unitless) spectra of 60 nm thick films: 1:3 MEH-PPV:PCBM (solid line), MEH-PPV film (dotted line), and PCBM (dashed line). MEH-PPV:PCBM is in arbitrary units, MEH-PPV and PCBM absorption are scaled to the values needed to fit the MEH-PPV:PCBM absorption.

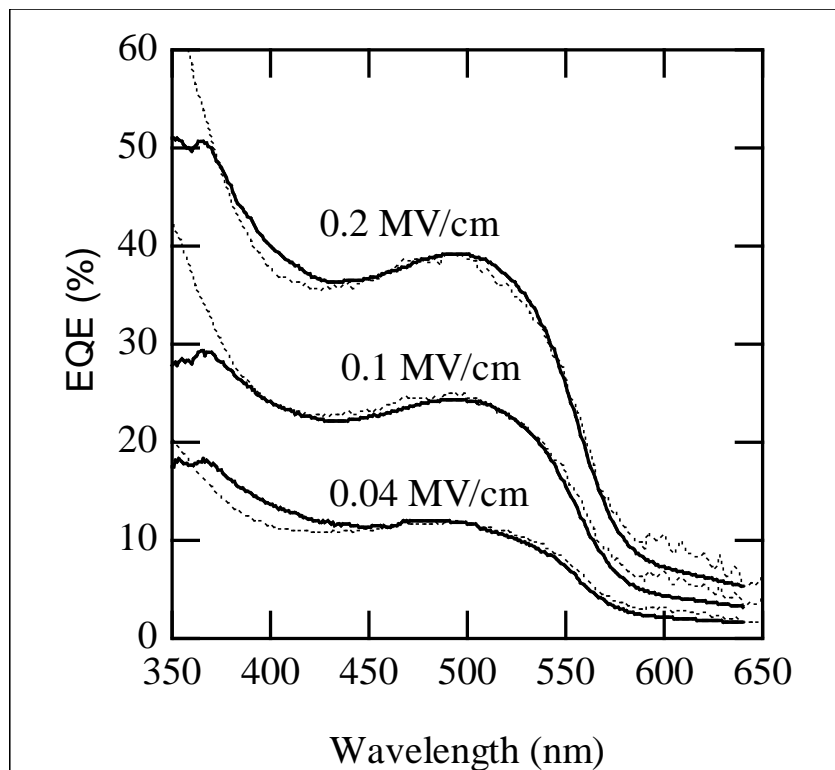


Figure 4-13. Quantum efficiency (solid lines) spectra of 165 nm thick 1:3 MEH-PPV:PCBM with 10  $\mu\text{m}$  spacing electrodes for 0.04, 0.1 and 0.2 MV/cm applied fields. The dashed lines are fits using a linear combination of MEH-PPV and PCBM absorption spectra.

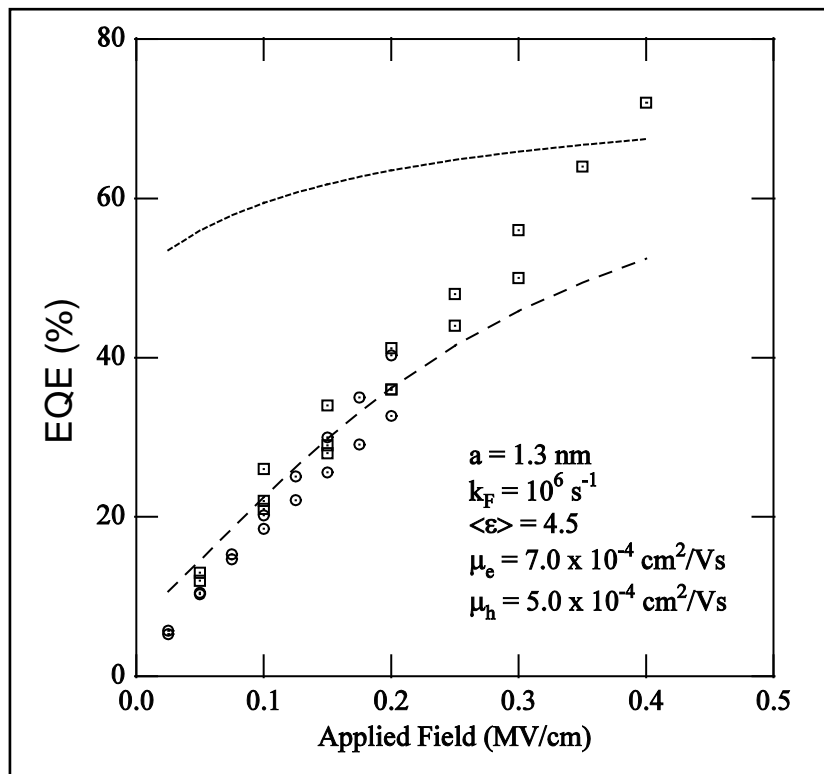


Figure 4-14. Quantum efficiency at 494 nm versus applied electric field for 165 nm thick 1:3 MEH-PPV:PCBM interdigitated devices with 5  $\mu\text{m}$  (circles) and 10  $\mu\text{m}$  (squares) electrode spacing. Dotted line is a fit with a modified Onsager model using parameters in the figure, and assuming Langevin recombination. Dashed line is a fit with the same model, but with the bimolecular recombination reduced to 0.008 the Langevin value.

## CHAPTER 5 PLANAR HETEROJUNCTION

In the previous chapter, organic photoconductors with an active layer made up of a bulk heterojunction were described; and in this chapter, photoconductors with a planar heterojunction are studied. The difference between these two types of devices was described in Chapter 3. In a planar heterojunction, the organic donor–acceptor interface separates excitons much more efficiently than the organic–metal interfaces in a single-layer bulk heterojunction device and vapor-deposited materials have a higher purity (as compared to devices made by spin-coating), so more efficient devices may be made. In these devices, like the bulk heterojunction devices, we study what step in the photoconducting process limits the quantum efficiency by measuring the quantum efficiency of devices with different layer thicknesses and modeling the exciton dissociation. We also study the effect of heterojunction energy offsets on the quantum efficiency by fabricating and testing planar heterojunction photoconductors with a variety of polymers.

The devices studied here are interdigitated lateral photoconductors with oxidized aluminum contacts with two vertical layers, one for hole transport and one for electron transport. The thickness of both layers combined was less than the thickness of the electrode, so horizontal transport still takes place in these devices. Figure 5-1 shows a schematic drawing of the devices studied in this chapter.

### **Device Structure and Operation**

The main factors affecting photocurrent in the organic devices are: (1) absorption (2) excitons reaching the interface of the two transport materials, (3) dissociation of the exciton, and (4) transport of the charge carriers to the electrodes without recombining at

trap sites. The energy band diagram of an electron-hole pair being separated and carried by each polymer is shown in Figure 5-2.

A number of steps are necessary in the process of converting incident light (photons) to collected charge (electrons). First, an exciton is absorbed in the active layer and forms an electron-hole pair. The electron and hole can be dissociated by providing an interface across which the chemical potential of electrons decreases.<sup>60</sup> After the dissociation of the exciton, the charge carriers must travel through the organic / small-molecule material to be collected at the electrode contacts. The transport materials used must have sufficiently high mobility, or else the carriers will not reach the electrodes and instead will recombine at trap sites or remain in the device as undesirable space charges that oppose the drift of new carriers.

Devices with lateral interdigitated electrodes have special device physics when compared to typical vertical devices. In vertical devices, the transport is in the same direction as the absorption. In lateral devices, the transport plane is normal to the absorption plane. In the devices with evaporated multilayers that make up the active layer,  $\alpha$ -6T is the hole-transporting material and C<sub>60</sub> is the electron-transporting material. In these types of devices, the heterojunction is planar. Excitons must diffuse to the junction and then dissociate. Therefore, layered devices must be thin to enable successful diffusion of the charge carriers to the contacts. However, the thinner the layer, the less light it can absorb. In lateral devices, the layer must also be thick enough to have continuous transport.

## Device Fabrication

The devices are made on glass substrates with aluminum interdigitated fingers. The active layer is made up of evaporated layers of one hole-transporting materials and one electron transporting material. Several different materials were used as hole-transporting materials: poly(2 - methoxy - 5(2' - ethyl)hexoxy - phenylenevinylene) (MEH-PPV), poly[2-methoxy-5-(2-ethylhexyloxy)- $\alpha$ -cyano-p-phenylene vinylene] (MEH-CN-PPV), poly(9,9-dioctylfluorene-co-benzothiadiazole) (F8BT), poly(9,9-dioctylfluorene) (PFO); and C<sub>60</sub> was used as the electron-transporting material. All materials were obtained from American Dye Source. Figure 5-3 shows the structure of the materials used in this study.

The fabrication procedure for the interdigitated devices is as follows. Interdigitated aluminum (100nm) electrode structures were defined photolithographically on glass substrates in a lift-off process. The spacing between electrodes is 5, 10, 25, 50 or 100 nm, with electrode widths of 50 nm. The interdigitated electrodes cover an area of 3 mm x 3 mm. After lift-off, the electrodes were cleaned in an oxygen plasma for 2 minutes to remove any remaining organic material from a well-defined oxide layer. Aluminum acts as a blocking contact and by oxidizing it we further reduce electrical injection of carriers.<sup>61</sup> Patterned substrates were immediately loaded into a glovebox with an integrated evaporation system for further processing. The hole-transport and C<sub>60</sub> layers were thermally deposited at a rate of 3 Å/s on cleaned substrates at a vacuum pressure of 10<sup>-7</sup> Torr. The layers were prepared immediately after one another without breaking vacuum.

The samples were then loaded into a vacuum cryostat and all measurements were carried out at room temperature in an inert environment. Capacitance and current-voltage measurements were taken using a Keithley SourceMeter. For photocurrent measurements, samples were illuminated from the substrate side with optically chopped light from a monochromator. The incident illumination was measured with a calibrated Newport 818UV photodiode. External quantum efficiencies were calculated as collected charge per incident photon. Quantum efficiencies were corrected for the shadowing of light by the electrodes, but not for reflections or incomplete light absorption. Samples were made with the hole-transporting layer closest to the electrode and with the electron-transporting layer closest to the electrode, and a negligible difference in the calculated results was found.

### **Model for Exciton Dissociation**

To model the exciton dissociation, we study devices with  $\alpha$ -6T as the hole-transporting material and C<sub>60</sub> as the electron-transporting material. Figure 5-4 shows the results of quantum efficiency measurements for devices with  $\alpha$ -6T and C<sub>60</sub> layers comprising the active layer of the device. Both layers are 500Å thick, with an applied field of 10<sup>5</sup> V/cm. The interdigitated aluminum fingers are 50µm wide, and the spacing between the fingers varies between 5µm - 100µm. The applied voltage was varied such that the field was the same for each of the devices.

It was found that the quantum efficiency varied with interdigitated finger spacing for the devices made from evaporated organic layers. As discussed in the device physics section, there are three main processes involved in the conversion of the incident photons to measured electrons: excitons must reach the interface, dissociate,

and the charges must travel to the electrodes without becoming trapped or recombining. First, we investigate the dissociation of the exciton to the interface at the planar heterojunction using the model described below. In the illustration in Figure 5-5, light hits the device from the substrate side and then passes through the first layer of thickness  $d_1$ , where the absorption coefficient is represented by  $\alpha_{o1}$  and the diffusion of the exciton is represented by  $\alpha_{e1}$ , with similar parameters describing the second layer.

From the illustration in Figure 5-5, an expression (Eq. 5-1) can be written to describe the quantum efficiency in the device

$$EQE = \int_0^{d_1} \alpha_{o1} e^{-\alpha_{o1}x} e^{-\alpha_{e1}(d_1-x)} dx + \int_{d_1}^{d_1+d_2} \alpha_{o2} e^{-\alpha_{o1}d_1} e^{-\alpha_{o2}x} e^{-\alpha_{e2}(x-d_1)} dx \quad (5-1)$$

When this expression is solved, we get Equation 5-2,

$$EQE = \left[ \frac{e^{-\alpha_{o1}d_1} - e^{-\alpha_{e1}d_1}}{\frac{\alpha_{e1}}{\alpha_{o1}} - 1} \right] + \left[ \left( \frac{e^{(-\alpha_{o1}-\alpha_{o2})d_1}}{\frac{\alpha_{e2}}{\alpha_{o2}} + 1} \right) * \left( 1 - e^{(-\alpha_{o2}-\alpha_{e2})d_2} \right) \right] \quad (5-2)$$

where:

$\alpha_{o1}$  = optical diffusion coefficient, layer 1

$\alpha_{o2}$  = optical diffusion coefficient, layer 2

$\alpha_{e1}$  = exciton diffusion coefficient, layer 1

$\alpha_{e2}$  = exciton diffusion coefficient, layer 2

$d_1$  = thickness of layer 1 and

$d_2$  = thickness of layer 2.

Equation 5-2 predicts the quantum efficiency based on exciton diffusion length. The optical diffusion coefficients are calculated from the absorption by Equation 5-3.

$$A = 1 - e^{-\alpha_0 d} \quad (5-3)$$

where  $A$  is the absorption and  $d$  is the thickness of the film. Using the following input parameters:  $\alpha_{e1} = 5 \times 10^5 \text{ cm}^{-1}$  (diffusion length of 20nm for  $\text{C}_{60}$ <sup>62</sup>),  $\alpha_{e2} = 2 \times 10^5 \text{ cm}^{-1}$  (diffusion length of 50nm for  $\alpha\text{-6T}$ <sup>63</sup>),  $d_1 = 500\text{\AA}$  and  $d_2 = 500\text{\AA}$ , a quantum efficiency of 13% is predicted at a wavelength of 450nm. In the previous section, we used the Onsager model to describe electric field dependence of separating a bound electron hole pair. Using a combined electron and hole mobility of  $0.1 \text{ cm}^2/\text{Vs}$ <sup>64</sup> for  $\alpha\text{-6T}$  and  $\text{C}_{60}$ , an  $A=35\%$  at 450nm, a field of  $10^5 \text{ V/cm}$ , and all other parameters the same, the Onsager model predicts that 34% of those excitons that reach the interface will dissociate. Combining these two predictions, it is estimated that the quantum efficiency should be 4.5% based on exciton diffusion and dissociation. However, experimental results for the quantum efficiency are less than 1%, as shown in Figure 5-4. In addition, we see a decrease in quantum efficiency for wider electrode spacings consistent with defects in the bulk of the active material. Traps could explain both the overestimate of the quantum efficiency and the field dependence. The photocurrent limited by trapping is proportional to the transit time and lifetime of the carriers as described by Equation 5-4, where where the transit time is described by Equation 5-5,

$$PC \propto \frac{\tau}{\tau_r} \quad (5-4)$$

$$\tau_r = \frac{L}{\mu(\mathcal{E}) \times \mathcal{E}} \quad (5-5)$$

and  $\tau$  is the lifetime of a free electron, which counts only the time spent by an electron in the conduction band. If the electron is trapped and thermally re-emitted to the conduction band, the time spent in traps is not included in  $\tau$ .<sup>65</sup>  $\tau_r$  is the transit time of a

free electron from one electrode to the other.  $L$  is the width between the electrodes,  $\mu(\varepsilon)$  is the field-dependent mobility, and  $\varepsilon$  is the applied electric field. For our devices, assuming we accurately know the mobility<sup>64</sup> and electric field, we get  $\tau_r = 0.002\text{s}$  and therefore a lifetime of 2ms can explain our quantum efficiency results. This is comparable to lifetime calculations of other organic photoconductors.<sup>66,67</sup>

### **Importance of Heterojunction Energy Offsets**

Organic materials typically have large exciton binding energies ( $> 0.5\text{ eV}$ ), so that dissociation only occurs at heterojunctions, contacts, or extrinsic defects. By varying the number of layers, layer thickness, and choice and deposition conditions of evaporated materials, we are able to study exciton dissociation and charge collection in these devices. By varying the layer thicknesses we determine the exciton diffusion lengths in these materials. By varying the materials used in the devices we determine the importance of energy offsets at the heterojunctions in exciton dissociation. Carrier mobility is determined by material choice and deposition conditions, and affects separation of charges after excitons dissociate. Carrier mobility is assessed by transient photocurrent measurements. Charge trapping in the devices can lead to reduction of photocurrent. Photocurrent scaling with interdigitated finger spacing and applied field is used to study charge carrier trapping.

In this part of the study, we compare several different polymers as the hole-transporting material in the planar heterojunction devices: poly(2-methoxy-5-(2'-ethyl)hexoxy-phenylenevinylene) (MEH-PPV), poly[2-methoxy-5-(2-ethylhexyloxy)- $\alpha$ -cyano-p-phenylene vinylene] (MEH-CN-PPV), poly(9,9-dioctylfluorene-co-benzothiadiazole) (F8BT), and poly(9,9-dioctylfluorene) (PFO). In these devices, the

aluminum electrode spacing is 10 $\mu$ m with fingers that are 50 $\mu$ m wide. The polymer is deposited first to a thickness of ~10nm, and then the C<sub>60</sub> is evaporated on top to a thickness of ~10nm. Measurements were carried out in the same manner as described in the Device Fabrication section of this chapter.

Figure 5-6 shows the bandgap and HOMO and LUMO levels for each of the polymers. The energy offset on the LUMO side is greatest between C<sub>60</sub> and PFO, followed by MEH-PPV, F8BT, then MEH-CN-PPV. The majority of the materials used are good candidates for use in photoconductors for radiation detection because they absorb light within the visible spectrum (which is what the scintillator outputs). PFO is the only exception, but it was studied because of its great energy offset to C<sub>60</sub>. The absorption of each material is shown in Figure 5-7. The absorption was calculated by measuring the reflection and the transmission, and the assuming the rest must be due to absorption.

Figure 5-8 shows the quantum efficiency of each material at an applied voltage of 80 V. As we saw with the bulk heterojunction devices, the quantum efficiency spectra follow the absorption spectra for each material. Also similar to bulk heterojunction results, the quantum efficiency increases with increasing electric field, as shown in Figure 5-9. This figure shows the quantum efficiency spectra for F8BT/C<sub>60</sub> devices at increasing applied voltage. These spectra could be fit to the spectra of the quantum efficiency contributions from F8BT and C<sub>60</sub>.

In Figure 5-10, the quantum efficiency contribution (defined as quantum efficiency per absorbed photon) with increasing applied field for each polymer. In these devices, the photoluminescence is quenched and gain is possibly observed. Figure 5-11 puts all

this information together in one graph. Here, it can be seen that materials with higher energy offsets had higher quantum efficiency contributions. PFO has the greatest quantum efficiency contribution per absorbed photon, and also has the largest LUMO energy offset from C<sub>60</sub>. Alternatively, MEH-CN-PPV has the smallest quantum efficiency contribution and the smallest energy offset. Finally, Figure 5-12 shows the energy offset compared to quantum efficiency contribution for each polymer alone, and in a device with C<sub>60</sub>. Here, it is easy to see that the heterojunction energy offset has a strong effect on the quantum efficiency. So increasing the energy offset of the materials (while still using materials in the desired absorption range) is an important way to increase the quantum efficiency of devices.

### **Conclusions**

In devices with a planar heterojunction, it was found that the quantum efficiency was limited by trap sites in the active layer. By predicting the quantum efficiency based on a model for the exciton diffusion to the interface and the dissociation of the excitons, the experimental quantum efficiency can be explained by trapping and a lifetime of the charge carriers could be calculated. Heterojunction energy offsets were also studied, and it was found that a larger offset leads to higher quantum efficiency per absorbed photon.

Height: 100nm Al interdigitated fingers, oxidized

Width: 50 $\mu\text{m}$  fingers, 10  $\mu\text{m}$  spacing

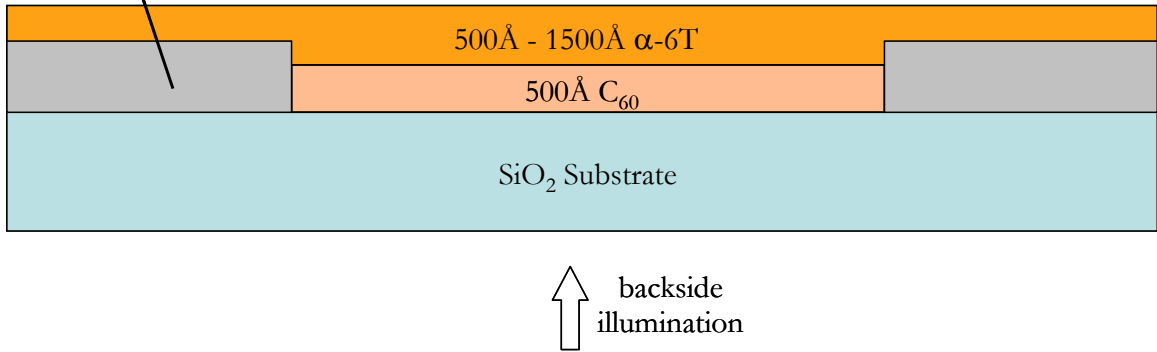


Figure 5-1. Schematic of device with a planar heterojunction

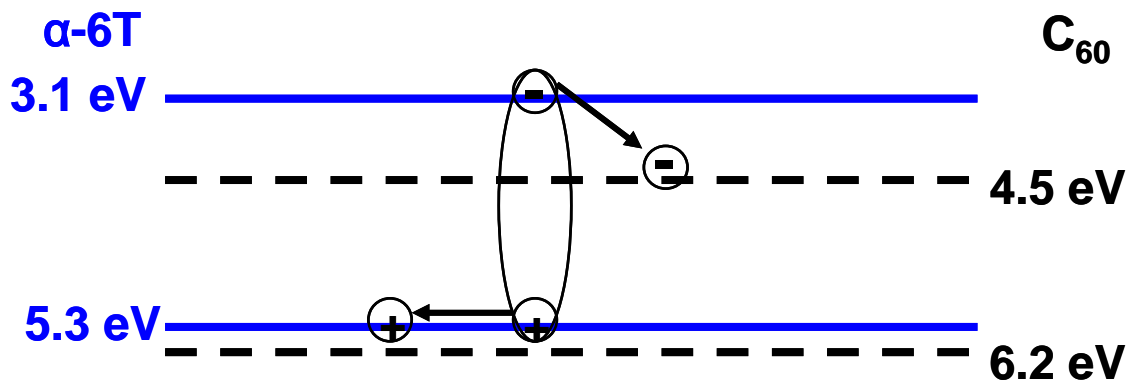


Figure 5-2. Energy band diagram for alpha sexithiophene and  $\text{C}_{60}$

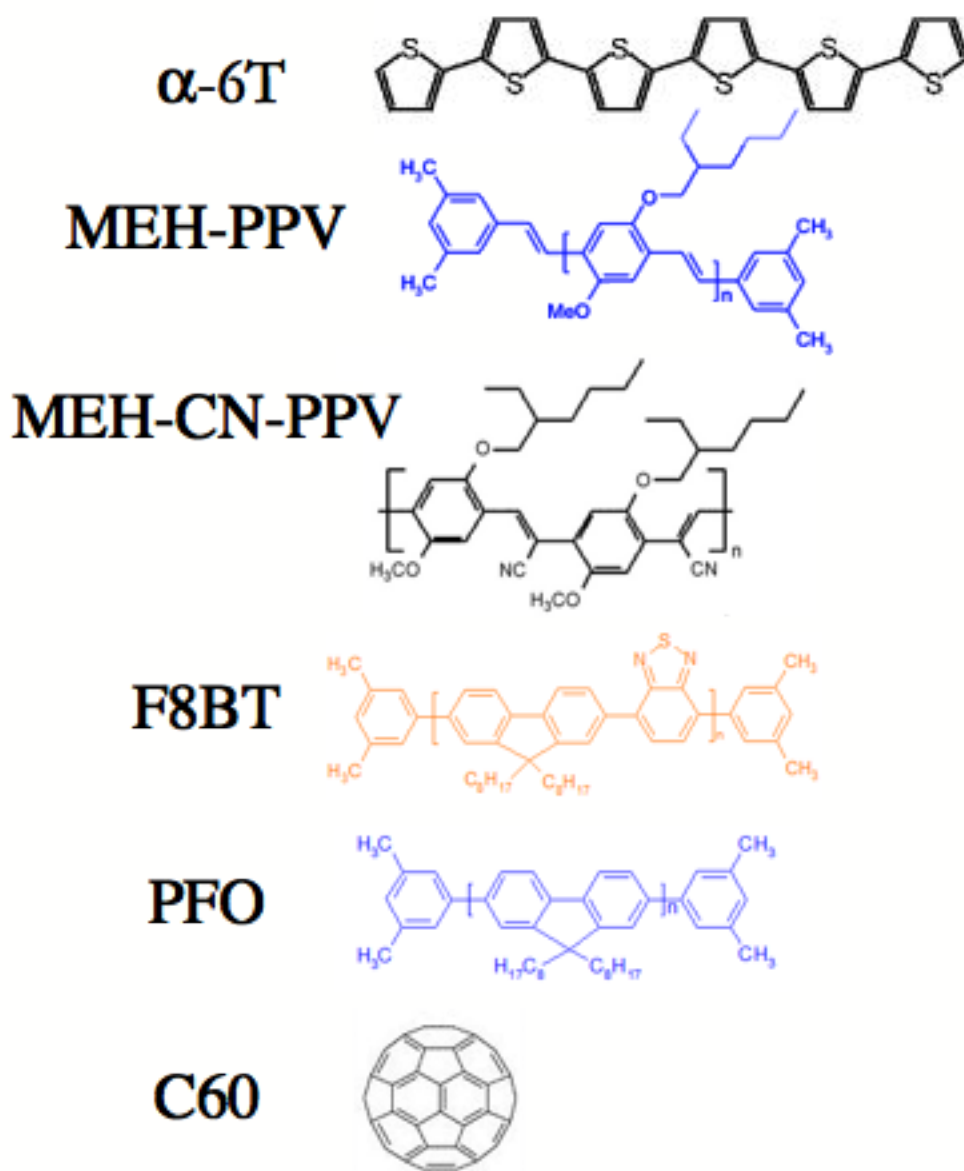


Figure 5-3. Materials used for multilayers in planar heterojunction devices.

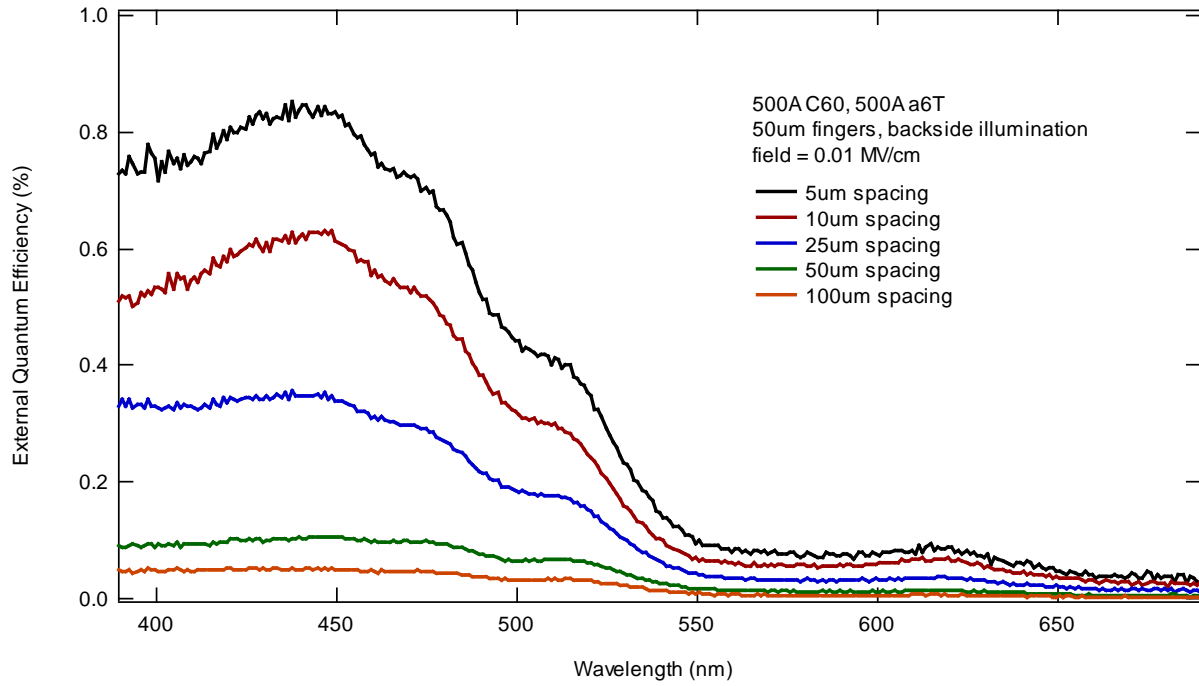


Figure 5-4. Quantum efficiency for  $\alpha$ -6T/C<sub>60</sub> devices with different spacings at the same field

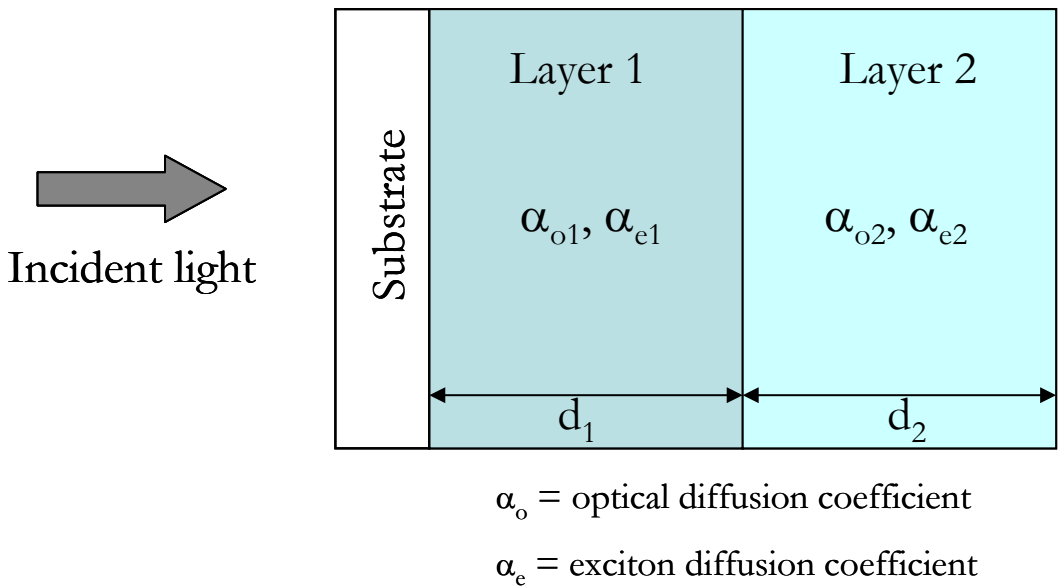


Figure 5-5. Device layout for exciton dissociation model

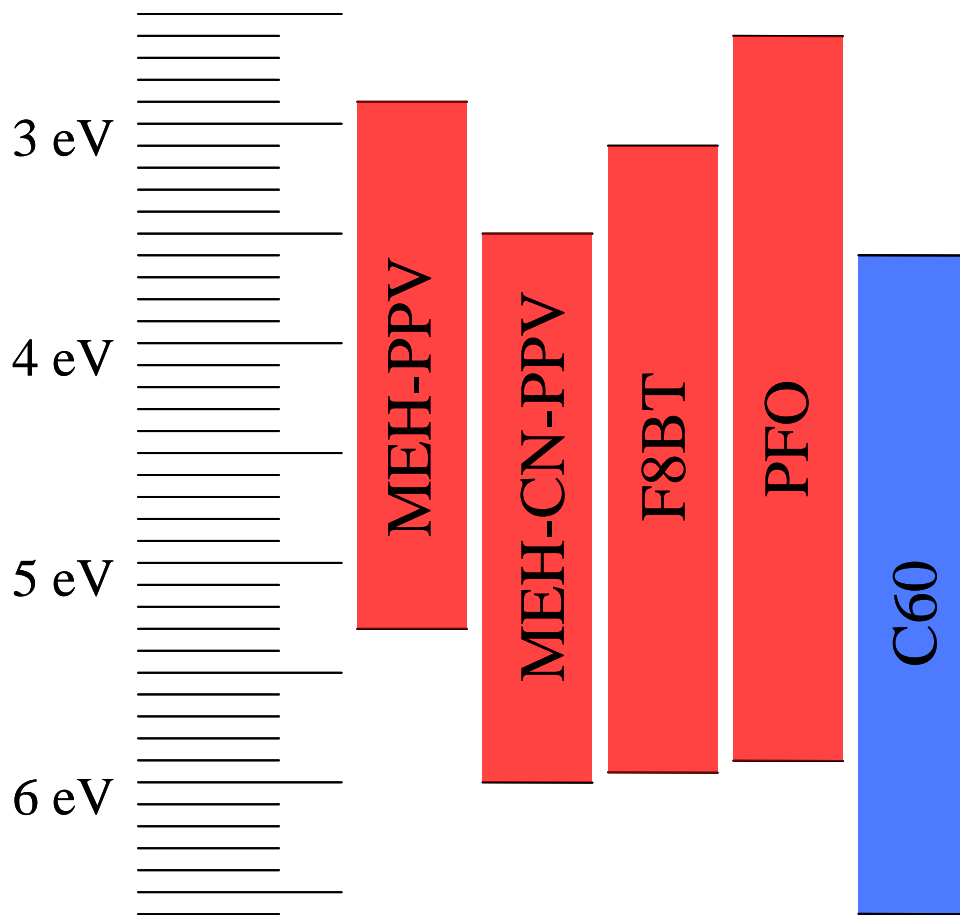


Figure 5-6. Organic transport levels for materials used in this study.

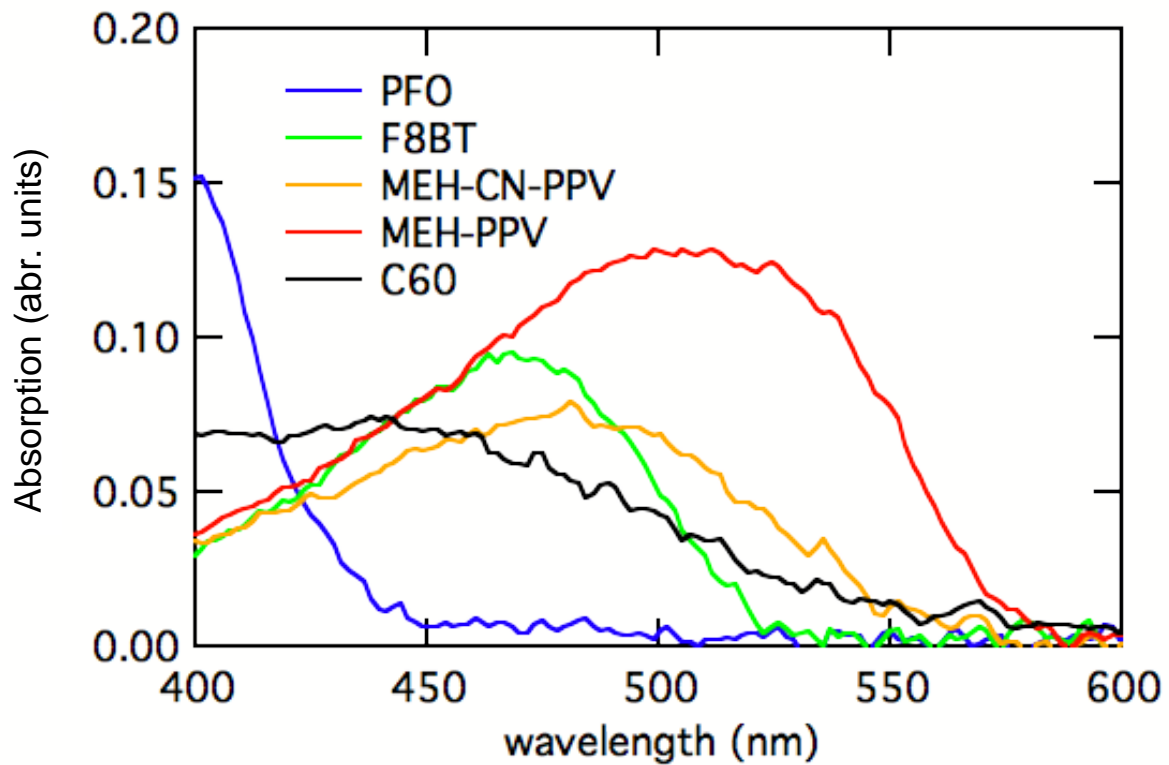


Figure 5-7. Absorption spectra for each polymer. Most absorb light within the visible spectrum, and would therefore be viable candidates to read scintillator output for radiation detection.

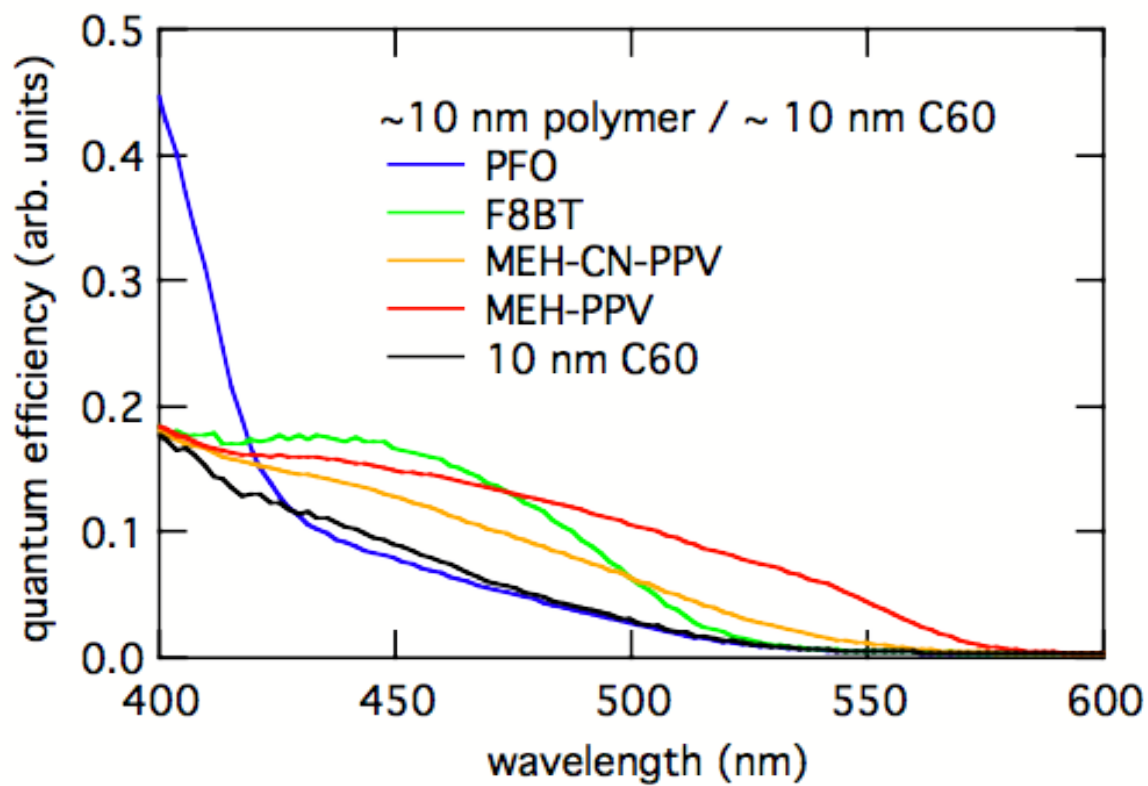


Figure 5-8. Quantum efficiency of each material at an applied voltage of 80V. As found in the previous section, quantum efficiency spectra follows the absorption spectra.

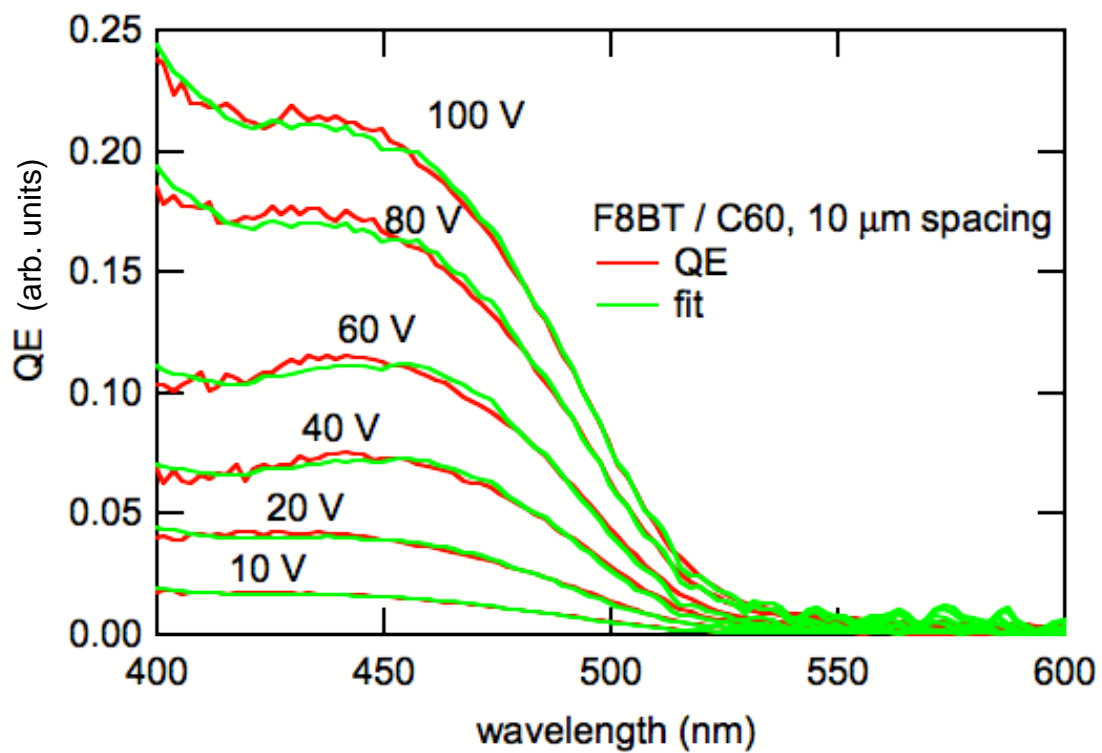


Figure 5-9. Quantum efficiency of F8BT/ C<sub>60</sub> devices at increasing applied voltage. The quantum efficiency spectra were fit with a sum of the contributions from F8BT and C<sub>60</sub>.

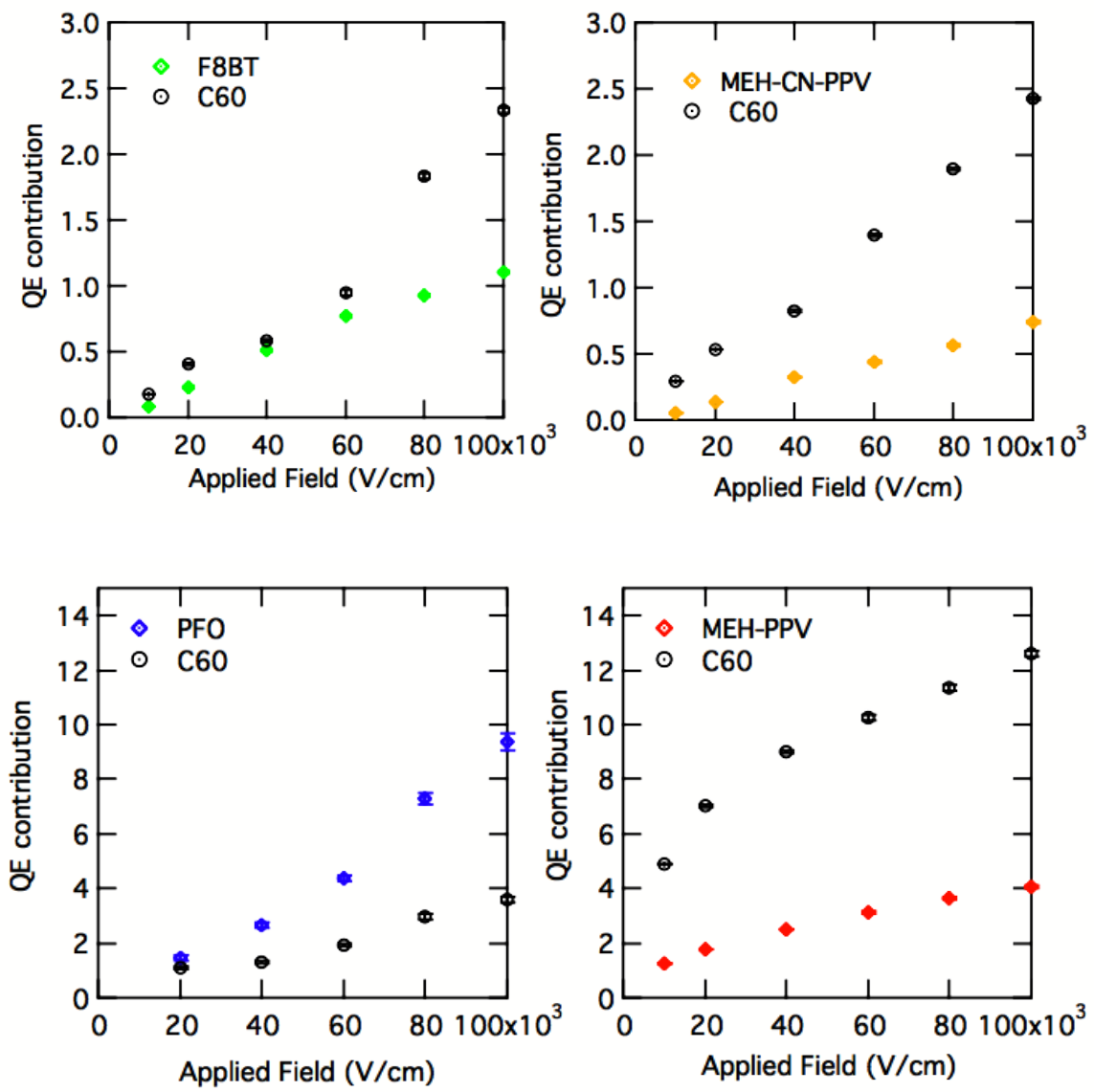


Figure 5-10. Quantum efficiency contribution (defined as quantum efficiency per absorbed photon) with increasing applied field for each polymer.

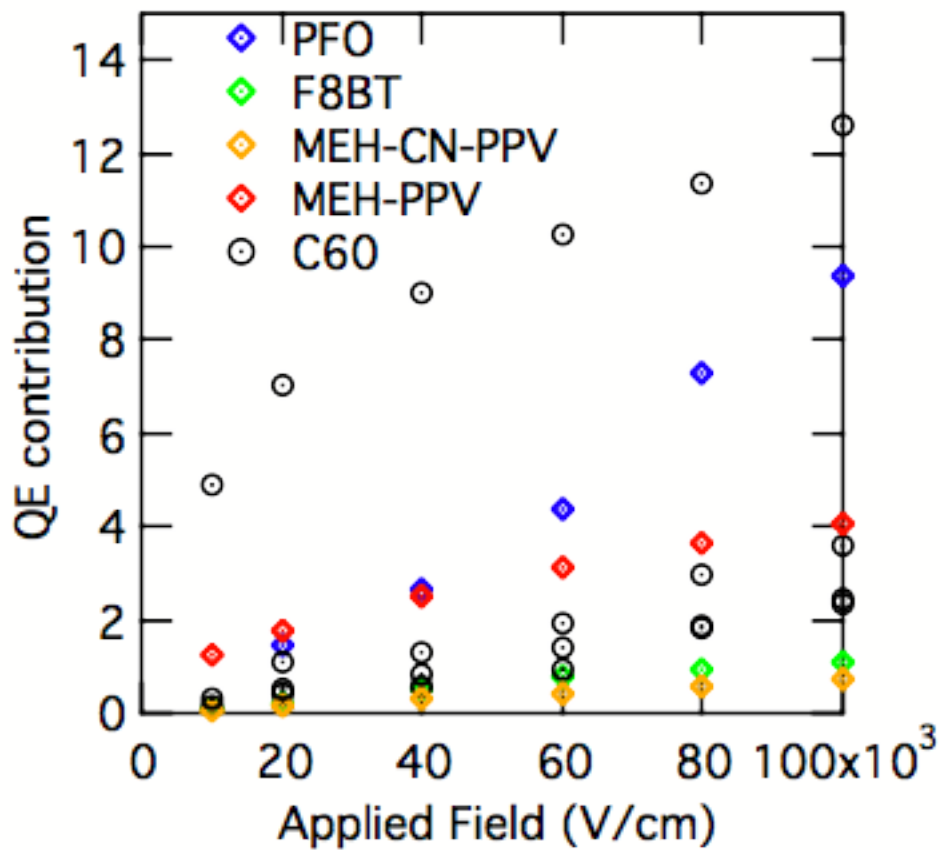


Figure 5-11. Summary of quantum efficiency contribution (defined as quantum efficiency per absorbed photon) with increasing applied field for each polymer. Materials with higher energy offsets had higher quantum efficiency contributions.

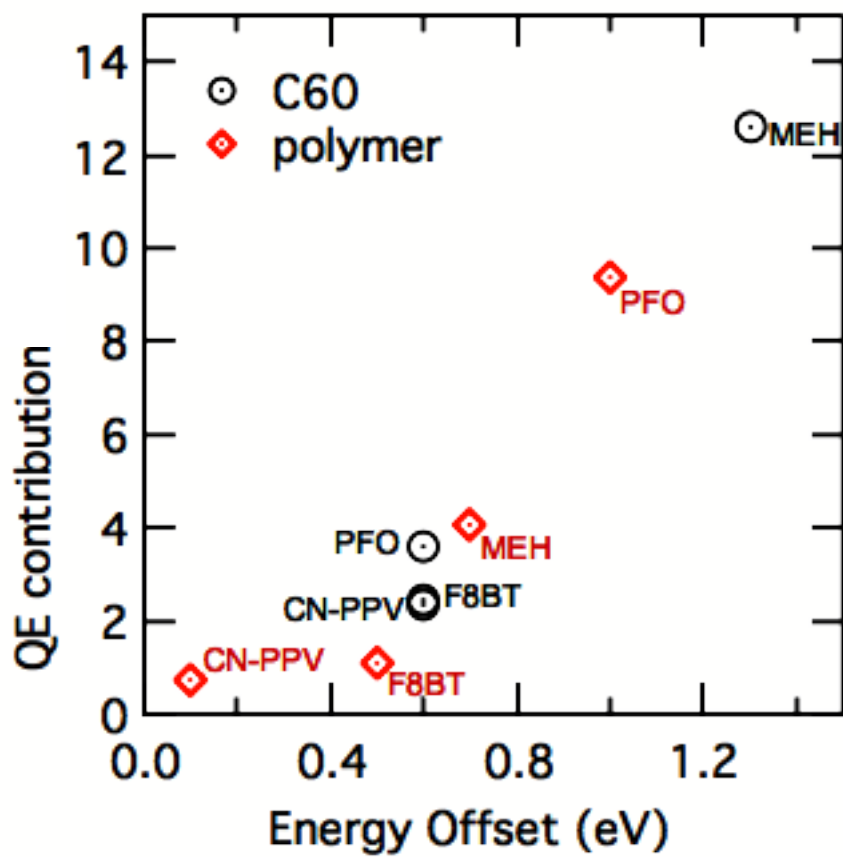


Figure 5-12. Energy offset compared to quantum efficiency contribution for each polymer alone, and in a device with C<sub>60</sub>. Measurements were taken at a applied field of 10<sup>5</sup> V/cm.

## CHAPTER 6 INTRODUCTION TO ENERGY STORAGE DEVICES

To have a better understanding of energy storage devices, this chapter will discuss the advantages of using capacitors, how they work, what supercapacitors are, and what other current research is being performed studying double-layer supercapacitors.

### **Importance of Portable Energy Storage**

The most important energy requirement for laptops and other consumer electronics products, such as cell phones and MP3 players, is energy-storage capacity. At a minimum, users want to be able to do several hours of uninterrupted work on their laptops on a full charge. Second is the ability to quickly charge the device, and third is cost.<sup>68</sup> The challenge is to create energy storage that is dependable, has long lifetime, safe, environmentally-sustainable, and portable.

If long-lived, low cost and safe batteries or capacitors are to be developed, a range of materials limitations must be overcome. The answer might lie in advances in new materials and new battery systems. According to Dr. Stanley Whittingham, director of the Materials Science Program and Institute for Materials Research at the State University of New York at Binghamton, "The materials challenges that need addressing are new anodes and cathodes that will store about double the energy of today's carbon anodes and oxide cathodes. But beyond the materials themselves, lower cost manufacturing methods need to be developed not only in the synthesis of the raw materials but also in the assembly of the cells and batteries. These will be major challenges as the materials go nano, with their low densities, and lifetimes of 10 years are demanded at costs of no more than \$250/kWh."<sup>69</sup>

## Current Technology

### Batteries

A battery is a device consisting of a single electrochemical cell or a group of cells that convert chemical energy into electrical energy. A wet cell (e.g., a car battery) contains free liquid electrolyte; in a dry cell (e.g., a flashlight battery) the electrolyte is held in an absorbent material, similar to a paste. Chemicals are arranged so that electrons released from the battery's negative electrode flow through a circuit outside the battery (in the device powered by it) to the battery's positive electrode. See Figure 6-1 for an illustration of how a battery works. The battery's voltage depends on the chemicals used and the number of cells (in series); the current depends on the resistance in the total circuit (including the battery — and thus on electrode size). Multiple batteries may be connected in series (the positive electrode of one to the negative electrode of the next), which increases total voltage, or in parallel (positive to positive and negative to negative), which increases total current. Batteries that are not rechargeable include standard dry cells used in flashlights and certain wet cells for marine, mine, highway, and military use. Car batteries, many kinds of dry cells used in cordless appliances, and batteries for certain military and aerospace uses may be recharged repeatedly.<sup>70</sup>

There are many different types of batteries, each with their own advantages and disadvantages. Lithium ion batteries have a higher energy density than most other types of rechargeable batteries and operate at higher voltages than other types, typically about 3.7 volts for lithium-ion cells vs. 1.2 volts for nickel-metal hydride (NiMH) or nickel-cadmium (NiCd) cells. Lithium-ion batteries also have a lower self discharge rate than other types of rechargeable batteries, retaining most of their charge even after

months of storage. NiMH and NiCd batteries can lose anywhere from 1-5% of their charge per day, (depending on the storage temperature) even if they are not installed in a device.

## **Capacitors**

A capacitor is an electrical device capable of storing electrical energy. In general, a capacitor consists of two metal plates insulated from each other by a dielectric. When a capacitor is connected in a circuit across a voltage source, the voltage forces electrons onto the surface of one plate and pulls electrons off the surface of the other plate resulting in a potential difference between the plates. The capacitance of a capacitor depends primarily upon its shape and size and upon the relative permittivity  $\epsilon_r$  of the medium between the plates. In vacuum, in air, and in most gases,  $\epsilon_r$  ranges from one to approximately one hundred or more.

Capacitors can be a possible alternative to batteries for energy-storage in some applications. However, the major advantages that super-capacitors offer must be balanced against some significant disadvantages. On the plus side, capacitors have a virtually unlimited lifetime of around 10,000,000 charge/discharge cycles, can charge and discharge at currents in excess of 1,000 Amperes, and are largely immune to temperature variations. However, they cannot compete with batteries in energy density or cost: Typically capacitors offer just 3-5% of the energy density of Li-Ion batteries and cost 10 to 15 times more.<sup>71</sup>

Capacitors present two significant design challenges in how they charge and retrieve energy. With charging, the challenge is to transfer energy to the capacitor when it is completely discharged (effectively presenting a short circuit), while retrieving energy also becomes progressively more difficult as the capacitor voltage approaches 0V.

Overcoming these two challenges is the main hurdle for the efficient use of supercapacitors as replacements to battery storage.<sup>71</sup>

### **Supercapacitors for Energy Storage**

Conventional batteries use a chemical reaction to produce energy. The problem is that after many charges and discharges the battery loses capacity to the point where the user has to discard it. However, capacitors contain energy as an electric field of charged particles created by two metal electrodes. Capacitors charge faster and last longer than normal batteries. The problem is that storage capacity is proportional to the surface area of the battery's electrodes, so even today's most powerful capacitors hold 25 times less energy than similarly sized standard chemical batteries. Thus, capacitors could be part of a solution to provide a better power source for a variety of applications.

At present, capacitors remain below batteries in specific energy stored but are superior in peak output, efficiency, and cycle time. The challenge for capacitors is to increase the stored energy without sacrifice of the other attributes. Considerable insight into capacitor design issues can be gained from even the most basic equation for capacitance. Consider a simple parallel plate capacitor, where the capacitance is given by Equation 6-1.

$$C = \frac{\epsilon A}{d} \tag{6-1}$$

In this equation  $C$  is the capacitance,  $\epsilon$  is the static dielectric constant,  $A$  denotes the electrode (plate) area, and  $d$  is the distance between plates. Clearly, a large dielectric constant ( $\epsilon$ ) and area ( $A$ ) are desirable while the distance between the electrodes ( $d$ ) should be as small as possible. The area and distance components can be optimized

using electrodes that are sized on the nanoscale. Such devices that have optimal values for these properties are called supercapacitors.

Electric double-layer capacitors are also known as supercapacitors, pseudocapacitors, electrochemical double layer capacitors (EDLCs), or ultracapacitors, and are electrochemical capacitors that have an unusually high energy density when compared to common capacitors, typically on the order of thousands of times greater than a high capacity electrolytic capacitor. For instance, a typical D-cell sized electrolytic capacitor will have a capacitance in the range of tens of millifarads. The same size electric double-layer capacitor would have a capacitance of several farads, an improvement of about two or three orders of magnitude in capacitance, but usually at a lower working voltage. This is why supercapacitors are great solutions for many energy storage applications, including (but not limited to) running vehicles and power regulation.

A fleet of seventeen buses near Shanghai has been running on supercapacitors for the past three years. Chinese company Shanghai Aowei Technology Development Company, along with its US partner Sinautec Automobile Technologies, predict that this approach will provide an inexpensive and energy efficient way to power city buses in the near future.<sup>72</sup> The biggest advantage of supercapacitors is that they can fully recharge in less than a minute, unlike lithium-ion batteries which can take several hours. The downside of using supercapacitors is that the buses currently have a very short range, providing a distance of only a few miles, due to the fact that supercapacitors can store only about 5% of the energy that lithium-ion batteries can hold. Although their short range makes supercapacitors impractical for cars, city buses have to stop frequently

anyway. By quickly recharging at bus stops, buses could take advantage of supercapacitors' other benefits: a bus with supercapacitors uses 40% less electricity compared to an electric bus with lithium-ion batteries, and requires just one-tenth the energy cost of a typical diesel-fueled bus, which would save about \$200,000 during the life of the vehicle.<sup>72</sup>

Supercapacitors can also be used for stabilizing and regulating existing power supplies. Despite the continuing growth of electricity demand, it is now increasingly difficult to construct more transmission lines and generating stations due to environmental and other constraints. Therefore, the maximum use of existing system is desirable but there is a concern of reduced stability in case of a system fault. The stabilization measure is important not only against a large disturbance such as short-circuit and ground fault, but also for small disturbance control in normal operation.<sup>73</sup>

### **Carbon Nanotube Electric Double-Layer Supercapacitors**

Currently, there is work being done on models similar to the system we study. Most are ball-and-stick simulations of charges and how they create a double charge layer, as opposed to our system that uses simulations of actual molecules. A summary of the literature is shown in Table 6-1.

In the work by Chen, et. al.<sup>74</sup>, a molecular dynamics model of the fluidic electrokinetic transport in a nanoscale channel with two bulk sinks was presented, and the process of ion transport in the nanochannel was simulated in this paper. The simulation model investigates the effects of the various physical parameters on the electroosmotic flow such as the surface charge density and the applied voltage. In this study, the concentration profiles determined by the molecular dynamics simulation were compared against the Poisson-Boltzmann equation and they found that with the

increase of the surface charge density, the exclusion of co-ions and enrichment of counterions become more remarkable, the number of cations passing through the pump region increases, and the number of anions decreases. Therefore, the transport efficiency of counterions (co-ions) in the nanochannel can be effectively controlled by changing the surface charge density.

Joly, et. al.<sup>75</sup> studied a system where the fluid (solvent and microions) was confined between two parallel solid substrates, composed of individual atoms on an fcc lattice (100 direction). They used molecular dynamics simulations to show that a finite slip effect for the solvent at a charged surface considerably enhances the measured electrokinetic effects. They created the density profiles and were also able to calculate velocity profiles from the data.

In another study, Yang et. al.<sup>76</sup> used the results of Monte Carlo simulations to compare the primitive (water being continuum) and non-primitive electric double-layer models with the classical Gouy–Chapman model in 10Å and 20Å slit-type nanopores. Their concentration profiles generated for varied surface charges show good agreement between the Gouy-Chapman and primitive models in both the 10Å and 20Å pore studies.

Joseph et. al.<sup>77</sup> studied the effects of nanoscale confinement and partial charges in silica slit channels filled with 1M KCl. They used partial charges of both bulk and surface atoms from ab initio quantum calculations that take into account bond polarization and electronegativity are used in molecular dynamics simulations to obtain ion and water concentration profiles for channel widths of 1.1, 2.1, 2.75, and 4.1 nm. First, the molecular electrostatic potential which accounts for the quantum effects at the silanol

surface is calculated using density functional theory. Partial atomic charges on the wall atoms are computed using a molecular electrostatic potential fit which were then used as inputs for the molecular dynamics calculations. Transport coefficients such as mobilities and diffusion coefficients were then computed from the molecular dynamics simulations. They were able to show that the partial charges from quantum calculations significantly alter transport properties of electrolytes in confined geometries.

In a final important paper, Qiao et. al.<sup>78</sup> investigated electroosmotic transport in a carbon nanotube using molecular dynamics calculations. The system consists of a (40,40) single-walled carbon nanotube that encloses a NaCl solution. Surface charge densities of +0.076 (where Cl<sup>-</sup> is the counterion) and - 0.076 C/m<sup>2</sup> (where Na<sup>+</sup> is the counterion) were observed in two separate simulations. The adsorption behavior of the Na<sup>+</sup> and Cl<sup>-</sup> counterions (which depends on the size of the counterion), the local electrostatic interactions between ion-water and ion-charged surface atoms and on the external electric field, were all found to be very different even though the magnitude of the charge density on the CNT surface was the same.

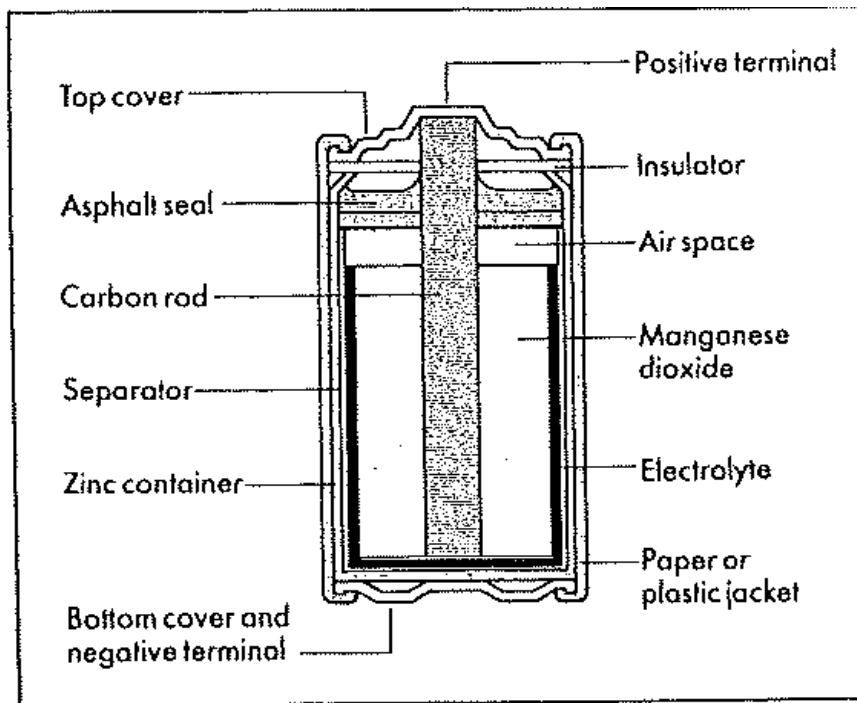


Figure 6-1. How a conventional dry cell battery works.<sup>70</sup>

Table 6-1. Summary of electric double-layer super capacitors literature review.

Primary Author	Method	Particles	Thermostat	Water Model	Coulomb	Miscellaneous
Chen	MD	~3000	Berendsen with a timestep of 0.1 ps	TIP4P with SETTLE	Ewald with slab correction	Equations of Motion were integrated using the leap-frog algorithm using a time step of 1-2 fs
Joly	MD	~10000	Hoover	N/A	Ewald	-
Yang	GCMC	Average of 350-1000	N/A	Primitive	Modified Charged Sheet (CS) method	-
	CMC	2400-5300	N/A	TIP4P-FQ		
Joseph	MD	-	Berendsen with a timestep of 0.1 ps	SPC/E with SHAKE	2D PME	MD simulations with partial charges (using DFT) were also included.
Qiao	MD	~4000	Berendsen with a timestep of 0.1 ps	SPC/E with LINCS	Particle Mesh Ewald (PME)	-

## CHAPTER 7 THEORETICAL BACKGROUND

In this chapter, we discuss the electrostatics behind capacitors and the theory behind the types of computational models we implement to study the capacitors.

### Electrostatics

Elementary electrostatics can be used to derive an expression for the electric field resulting from a single charged conducting plate of infinite extent via Gauss' Law as Equation 7-1,

$$E = \frac{\sigma}{2\epsilon_0} \quad (7-1)$$

where  $E$  is the electric field,  $\sigma$  is the surface charge density, and  $\epsilon_0$  is the electric permittivity of free space.<sup>79</sup> Similarly, the electric field outside of the surface of a conducting sphere is given by Equation 7-2,

$$E(r) = \frac{Q}{4\pi\epsilon_0 r^2} \quad (7-2)$$

where the electric field  $E$  is now a function of distance  $r$  from the centre of the sphere and  $Q$  is the total charge on the sphere. For a cylinder, the analogous expression is Equation 7-3,

$$E(r) = \frac{\lambda}{2\pi\epsilon_0 r} \quad (7-3)$$

where  $\lambda$  is the charge per unit length. Since electric field is an additive quantity, it follows that the electric field between two such oppositely charged plates is simply given by superposition as Equation 7-4.

$$E = \frac{\sigma}{\epsilon_0} \quad (7-4)$$

The models treated here describe shaped electrodes formed from an array of closely spaced point charges. For example, the plate geometry is represented by a square of point arrays lying in a common plane. In this case, the electric field at an arbitrary point in space is given from Coulomb's Law, Equation 7-5,

$$E = \sum_i \frac{q_i}{4\pi\epsilon_0 r_i^2} \quad (7-5)$$

where the sum is over all point charges  $i$  having point charge  $q_i$  and distance from the arbitrary point  $r_i$ . By a comparison with the conducting plate model, an estimate of the error in the calculation of the electric field using the discrete model can be estimated.

### **Computational Modeling**

Computational chemistry is a branch of chemistry that uses principles of computer science to assist in solving chemical problems. From modeling a system, we get an atomic-level description of what is going on in a system that could explain bulk effects. Also, a theoretical environment has the advantage that the system can be controlled precisely as opposed to an experiment where certain variables may be fixed or unable to be controlled accurately. Computational chemistry uses the results of theoretical chemistry, incorporated into efficient computer programs, to calculate the structures and properties of molecules and solids. While its results normally complement the information obtained by chemical experiments, it can in some cases predict as of yet unobserved chemical phenomena. It is widely used in the design of new drugs and materials. Examples of such properties simulated are structure (i.e. the expected positions of the constituent atoms), absolute and relative (interaction) energies, electronic charge distributions, dipoles and higher multipole moments, vibrational frequencies, reactivity or other spectroscopic quantities, and cross sections for collision

with other particles. In this study, a few types of simulation methods in particular are used and are described in the following sections. Simulations on the carbon nanotubes were done using molecular dynamics calculations; and the CO calculations use density functional theory approximations.

### **Molecular Dynamics Calculations**

Using molecular dynamics simulations, researchers can get an accurate look at what happens to individual atoms and molecules during experiments. Quantum molecular dynamics is quite different from classical molecular dynamics, which is primarily concerned with the classical motion of atoms interacting with a given potential. Physicists developed quantum mechanics early in the 20th century to appropriately describe the physics and chemistry of matter at the microscopic level. Quantum mechanical methods are very powerful but computationally expensive, while the classical or molecular mechanics methods are fast but suffer from several limitations (require extensive parameterization; energy estimates obtained are not very accurate; usually cannot be used to simulate reactions where covalent bonds are broken/formed; and are limited in their abilities for providing accurate details regarding the chemical environment).

Molecular dynamics simulations calculate the time dependent behavior of a molecular system. They generate information at the microscopic level, including atomic positions and velocities. The conversion of this microscopic information to macroscopic observables such as pressure, energy, heat capacities, etc., requires statistical mechanics, another field of computational chemistry.

Since the first dynamical calculation of a simple liquid of hard spheres by Alder and Wainwright<sup>80-83</sup>, molecular dynamics simulations have grown rapidly in

complexity. These calculations have provided detailed information on the fluctuations and conformational changes of proteins and nucleic acids. These methods are now routinely used to investigate the structure, dynamics and thermodynamics of biological molecules and their complexes. They are also used in the determination of structures from x-ray crystallography and from NMR experiments.

### **Density Functional Theory**

The mathematical expressions that describe a molecular system are described in quantum mechanics.<sup>84-86</sup> The most important parameter is the wave function from the time-independent Schrödinger equation, Equation 7-6.

$$H\psi = E\psi \quad (7-6)$$

In this equation,  $\psi$  is the wave function that completely determines given physical system,  $H$  is the Hamiltonian operator that represents the energy of the system as a sum of kinetics and potential energy, and  $E$  is the energy of the system obtained as an eigenvalue to the Hamiltonian. The equation cannot be solved exactly for systems larger than two particles. Since the real chemical systems are quite complicated, solving the Schrödinger equation for them requires approximations.

Depending on the desired accuracy, the approximations made in wave function-based methods can be more or less sophisticated. In general, to obtain the high accuracy needed to describe reaction energy profiles and other properties of a system one typically has to use methods that are quite expensive from computational point of view. Therefore, one is limited to treat only relatively small systems. An alternative way to express the energy of the system is by its electron density instead of the wave function.<sup>87,88</sup> The method that uses electron density to determine molecular properties is

Density Functional Theory, which can be very accurate for little computational cost.

Some methods combine the density functional exchange functional with the Hartree–Fock exchange term and are known as hybrid functional methods (such as the B3LYP method used in this study).

## CHAPTER 8 NANOSCALE SHAPED ELECTRODES

The efficiency of the oxygen reduction reaction in the electrolysis of water is a significant barrier to the widespread adoption of fuel cell technology for renewable energy storage. Methods of overcoming this problem are an area of current research and include the use of novel supports for the active component of the metal electrode and introduction of nanoparticles as electrodes. The move to the nanoscale is of particular interest as it not only provides a high surface area for the catalytic processes to occur but also offers the possibility of high electric fields at the electrode surface.

In this chapter, we study these high electric fields near the electrode surface at the nanoscale. We employ computational techniques to study the effects of an electric field on the stability of a carbon monoxide (CO) molecule near nanoscale electrodes shaped as a plate, a cylinder, and a sphere, which (when charged) generate fields with varying electric field gradients. The effect of the electric field gradient on how the CO bond breaks is studied. We also investigate its effects on the molecular orbital energies and the electron density to further understand the process.

### **Introduction**

Carbon monoxide has been the subject of numerous quantum chemical studies with the correct calculation of the dipole moment being a particularly challenging target. However, recent work has shown good agreement with electrostatic properties, such as dipole moments, polarizabilities and hyperpolarisabilities.<sup>89</sup> It can be noted for example, that calculations at the Hartree Fock level predict the incorrect sign for the dipole, whereas the use of correlated methods correct this problem.

A detailed experimental and computational study of the behavior of CO in strong electric fields was performed by Hush and Williams.<sup>90</sup> They performed Finite-Field CNDO-II calculations to produce information on optimized geometries and vibrational modes to compare to infra-red absorption measurements. In their calculations, they find an equilibrium bond length for CO of 1.191Å and measure the bond length in fields up to 100 V/nm where the bond length was calculated to be 1.212Å. Our study uses a more sophisticated theoretical model than their study from the 1970s, and therefore has more accurate results.

### Methods and Models

The calculations presented here were performed using the three-parameter B3LYP hybrid functional<sup>91,92</sup> as implemented in the Gaussian09 software.<sup>93</sup> A constrained energy minimization of the carbon monoxide molecule was performed such that the midpoint of the molecule was held fixed. A 6-311+G\*\* basis set was used for both carbon and oxygen. An additional calculation at the Coupled Cluster Singles and Doubles (CCSD) level of theory with an aug-cc-pVQZ basis set was performed on the CO molecule for comparison with the density functional calculation.

The Gaussian09 software provides two features that are vital for the models: firstly, the ability to specify uniform electric field at any arbitrary orientation across the molecule, and secondly to specify an arbitrary point charge array. A schematic of this model is shown in Figure 8-1. The center of the CO molecule is placed a distance  $r_1$  from the flat plate electrode and a distance  $r_2$  from the second electrode which can be a second plate, sphere or cylinder such that the molecule is oriented along a surface normal to the plate and bisecting the second electrode. Each electrode is made up from a regularly spaced array of point charges on the surface of plate, sphere and cylinder

respectively, as depicted in Figure 8-2. The total charge on the plate is distributed equally over the point charge surfaces. A description of each electrode shape is summarized in Table 8-1. The set-up of the calculations showing the placement of the CO molecule between each set of electrodes is shown in Figure 8-3.

For example, for the case of a spherical electrode and planar electrode, the electric field at the center of the C–O bond can then be formulated as Equation 8-1,

$$E = \sum_a \frac{q_a}{4\pi\epsilon_0 r_a^2} + \sum_b \frac{q_b}{4\pi\epsilon_0 r_b^2} \quad (8-1)$$

where  $a$  runs over the point charges,  $q_a$ , at distances  $r_a$  from the center of the sphere and  $b$  runs over the point charges on the plane.

In this study, the dissociation of a simple molecule, CO, with a small dipole moment, in the presence of an electric field is investigated. Both a uniform electric field and the electric fields resulting from electrodes of varying geometric shape are considered. Also, the change in electronic structure as a function of field is computed. Finally, the effect of the electric field gradient on the dissociation is examined. The resulting electric field for each of the geometries is shown in Figure 8-4. In the area of the CO molecule, the electric field is uniform between the two plates and the electric field is curved between the sphere and the plate.

## Results and Discussion

### CO in Absence of an Electric Field

As a starting point, geometry optimization calculations were performed on the CO molecule in the absence of an applied electric field both using the B3LYP hybrid functional and the coupled cluster level of theory. The results are summarized in Table 8-2. The electronic structure of CO is a classic problem in quantum chemistry. For many

years, it was difficult to calculate the dipole moment of the molecule correctly. For example, at the Hartree Fock level of theory, the dipole is predicted to point in the incorrect direction – with the negative charge on the oxygen.<sup>94</sup> As can be seen from the table, using the B3LYP functional, the results are comparable with the more expensive coupled cluster calculation.

With no applied field, the bond length of the CO molecule was calculated to be 1.128Å. We have studied the effects of the magnitude of an electric field is needed to break the CO triple bond for each geometry. For these systems, we have studied the effects on the energies of the molecular orbitals and the electron densities and compared these results to a molecule without a dipole, N<sub>2</sub>. These effects can be explained by the change in the electric field gradient as a result of having a nanoscale shaped electrode.

### **Applied Field to Break CO Bond**

The behavior of CO was investigated when a uniform electric field was applied directed along the CO bond axis. An increasing electric field was applied and a geometry optimization performed under the constraint that the center of the molecule remains fixed. The charge on the point charges that make up the electrodes was gradually increased and the bond length was calculated at several increments of charge. The variation of the CO bond length with applied field in a field between two plates, a cylinder and a plate, and a sphere and a plate are shown in Figure 8-5, Figure 8-6, and Figure 8-7. In the calculation with the CO molecule between two plates, it was found that the applied electric field needed to break the CO triple bond was 101.9V/nm in the case where the carbon atom of the CO molecule was closest to the positively charged plate and 98.5V/nm in the case where the oxygen atom was closest to the

positively charged plate. These calculations were confirmed by performing a Gaussian calculation with a uniform applied field generated by the software as opposed to creating a field with two plates with point charges. In this case, the calculated field required to break the bond was 95.2V/nm in the case where the oxygen atom was closest to the positively charged plate. This value is approximately 3% lower than the value calculated with the field coming from two charged plates, showing good correlation. Calculations were also performed where the CO molecule was free to move, and similar results were found.

In the calculation when the CO molecule was placed between a positively-charged plate and a negatively charged cylinder, it was found that the applied electric field needed to break the CO triple bond was 100.2V/nm in the case where the carbon atom of the CO molecule was closest to the positively charged plate and 95.0V/nm in the case where the oxygen atom was closest to the positively charged plate. In the calculation with the CO molecule between a positively-charged plate and a negatively-charged sphere, it was found that the applied electric field needed to break the CO triple bond was 84.5V/nm in the case where the carbon atom of the CO molecule was closest to the positively charged plate and 74.0V/nm in the case where the oxygen atom was closest to the positively charged plate. In the scenario where the oxygen atom is closest to the negative electrode, the charge required to break the bond was decreased by 24.9% when a spherical electrode was used instead of a plate. In addition to less applied field need, the case with the spherical electrode moved the carbon and oxygen atoms further apart after the bond broke than in the case with plate electrodes. For all

geometries, less applied charge was necessary to break the bond in the case when the oxygen atom was closer to the positive electrode.

### **Electric Field Gradient**

The electric field gradient of a uniform field (like the one between two charged plates) is zero. For fields created by shaped electrodes, the electric field gradient can be calculated by taking the derivative of the calculated electric field numerically. In the case where the electric field is generated between a charged cylinder and a charged plate, the electric field gradient was found to be  $-10.19 \text{ V/nm}^2$ . The field gradient was larger in the case where the electric field is generated between a charged sphere and a charged plate, at  $-20.38 \text{ V/nm}^2$ . This difference in the gradient of the electric field explains the phenomenon where the CO bond breaks in a field generated by a shaped electrode at a lower applied charge than in a uniform field.

### **Molecular Orbital Energies**

The molecular orbitals of CO are well established and summarized in Figure 8-8. The highest occupied molecular orbital is a  $\sigma$  bond, whereas the  $\pi$  orbitals lie at a slightly lower energy. An analysis of the molecular orbital energies as a function of field is instructive in the examination of the dissociation process. Figure 8-9 shows the energies of the molecular orbitals (labeled MO 3-8) as the applied field on the molecule is increased. Molecular orbitals 3 and 4 are the  $\sigma$  and  $\sigma^*$  orbitals from the 2s electrons on the carbon and oxygen atoms. Molecular orbitals 5 and 6 are the  $\pi$  bonding orbitals from the 2p electrons on the carbon and oxygen atoms. Molecular orbital 7 is the  $\sigma$  bonding orbital, which is the HOMO level. Molecular orbital 8 is the  $\pi^*$  antibonding orbital, which is the LUMO level. Initially, the pi bonding orbitals in the CO molecule are at a lower energy than the sigma orbital. As a stronger electric field is applied, the CO

bond breaks and the pi orbitals move to a higher energy than the sigma orbitals. In the scenario shown in Figure 8-9, the bond breaks at an applied field of 0.585 (arbitrary units).

### **Electron Density**

The shapes of the molecular orbitals along with the electron density was also studied. The discussion of these effects is all based on Figure 8-10. The top two pictures (A1 and A2) show the shape of the molecular orbital and the electron density when there is no charge applied to the CO molecule. The graphic of the shape of the HOMO (A1) shows a sigma-type bond where the majority of the charge is on the carbon atom (gray). The electron density picture (A2) shows the total electron density projected onto a surface inside which the majority of the electron density resides. The “striped” pattern comes from the quadrupole of the CO molecule.

In graphics B1 and B2 of Figure 8-10, there is a very small applied field of -17V/nm. Already, the electron density has shifted to the carbon atom and the pattern indicates a dipole instead of a quadrupole. The bond length is still approximately the same as it is with no charge applied. As the applied field is increased to -84V/nm (C1 and C2), the molecular orbitals now look like a pi-type bond when enough charge has been applied so the bond is about to break. Finally in graphics D1 and D2, the bond is broken and the carbon and oxygen atoms are far apart as the applied field is increased to -86V/nm.

### **Dinitrogen**

The same calculations as described above were also performed on a dinitrogen molecule ( $N_2$ ). Obviously, this molecule is not polar like the CO molecule. The results for the applied electric field necessary to break the dinitrogen triple bond in a uniform

Gaussian field, a field generated by two charged plates, in a field generated by a charged cylinder and a charged plate, and in a field generated by a charged sphere and a charged plate is shown in Table 8-3. The difference between the calculation with a uniform field generated by Gaussian and a field generated by two plates is only 2%, again showing good correlation. In the case of the dinitrogen molecule, the applied field necessary to break the N-N triple bond was 24% less than the field needed to break the bond in a uniform field which is in agreement with our previous results with the CO molecule. As expected, a higher field was needed to break the dinitrogen bond because it is stronger than the CO bond.

### **Conclusions**

In this chapter we have presented a detailed account of what occurs as the triple bond of a carbon monoxide (CO) molecule breaks in a field with and without an electric field gradient. We have shown that the HOMO energy level switches from a sigma orbital to a pi orbital as a higher field is applied and the bond breaks. Also, the applied field necessary to break the bond decreases by 25% when the electrode is changed from a plate shape with a uniform electric field to a sphere shape. These results were confirmed for a study of a dinitrogen (N<sub>2</sub>) molecule as well.

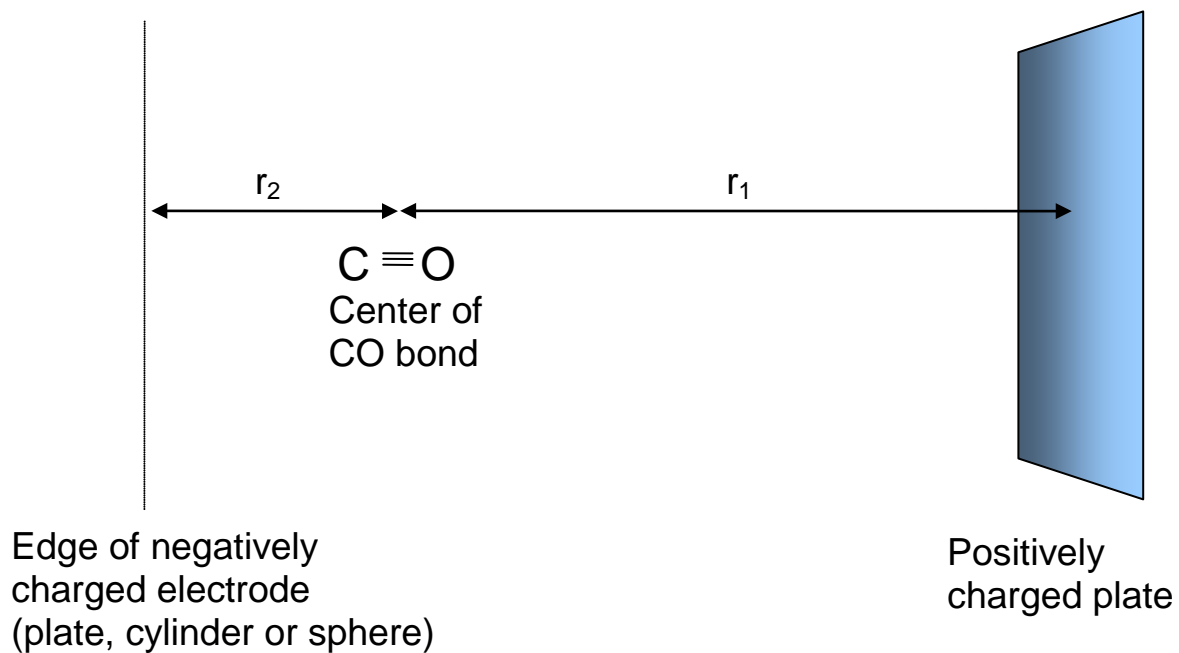


Figure 8-1. Schematic of model electrode setup

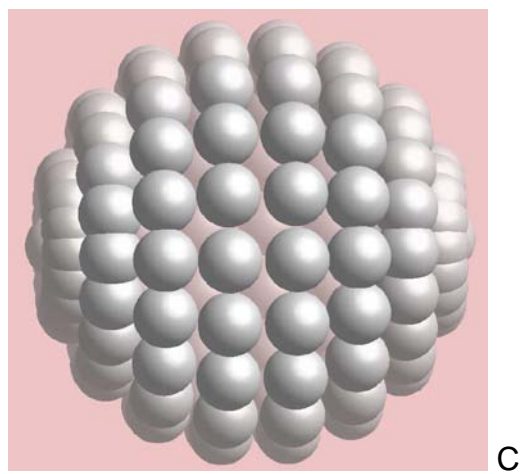
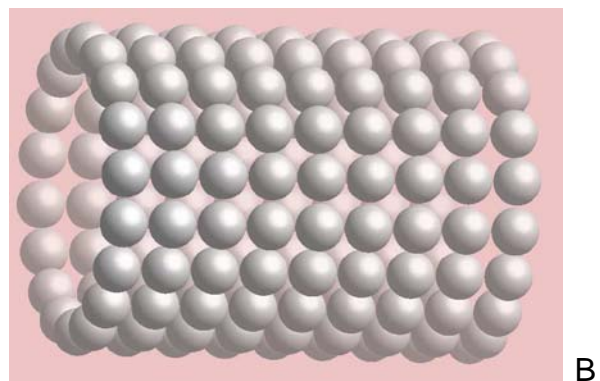
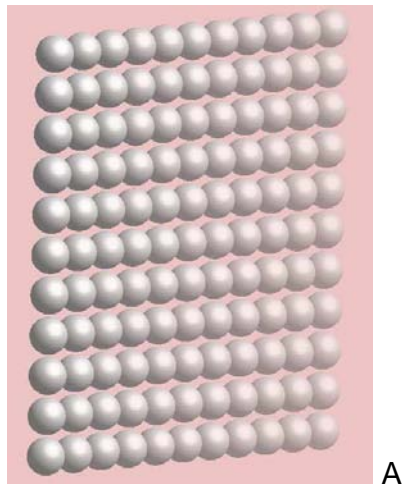


Figure 8-2. Electrode shapes consisting of point charge arrays. A) plate, B) cylinder, C) sphere.

Table 8-1. Summary of electrode shapes made from point charges

Electrode Shape	Dimensions	Number of Point Charges
plate	25 x 25Å	121
cylinder	14Å diameter, 20Å length	162
sphere	14Å diameter, 20Å length	146

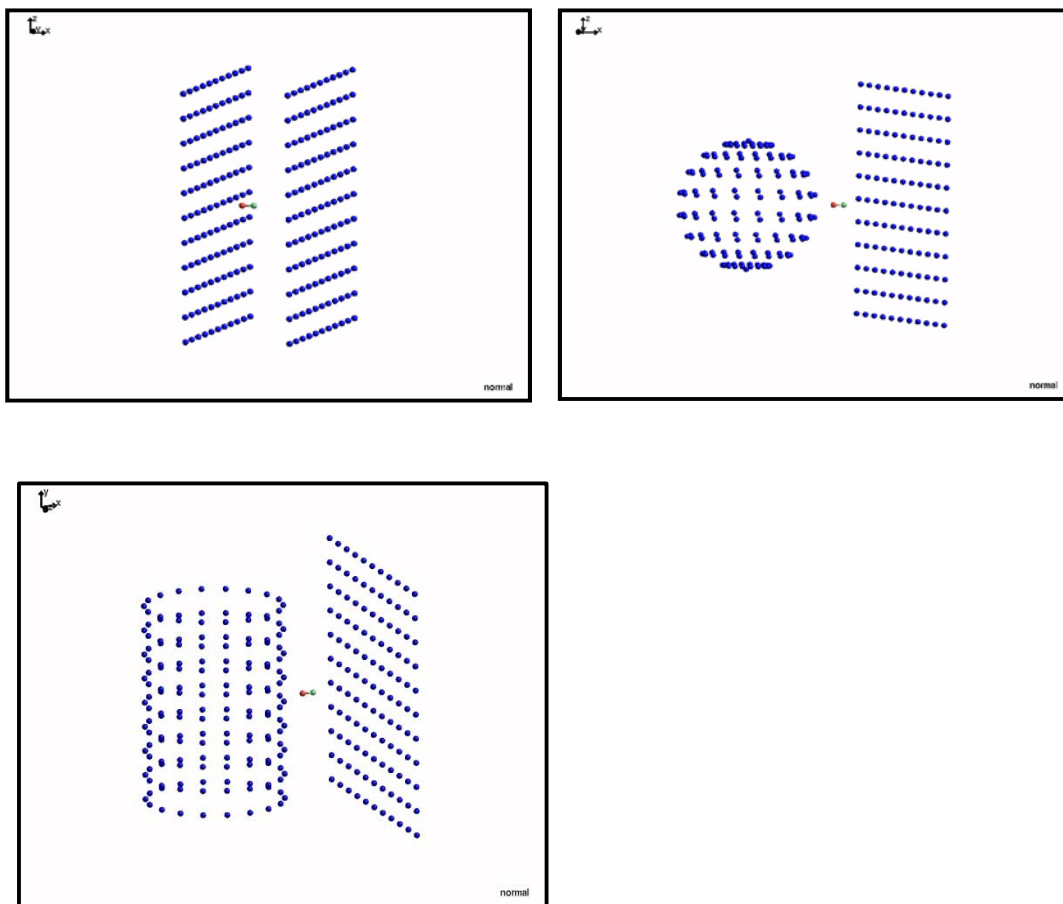


Figure 8-3. Diagram of calculation set-up for CO molecule between two charged electrodes of different geometries

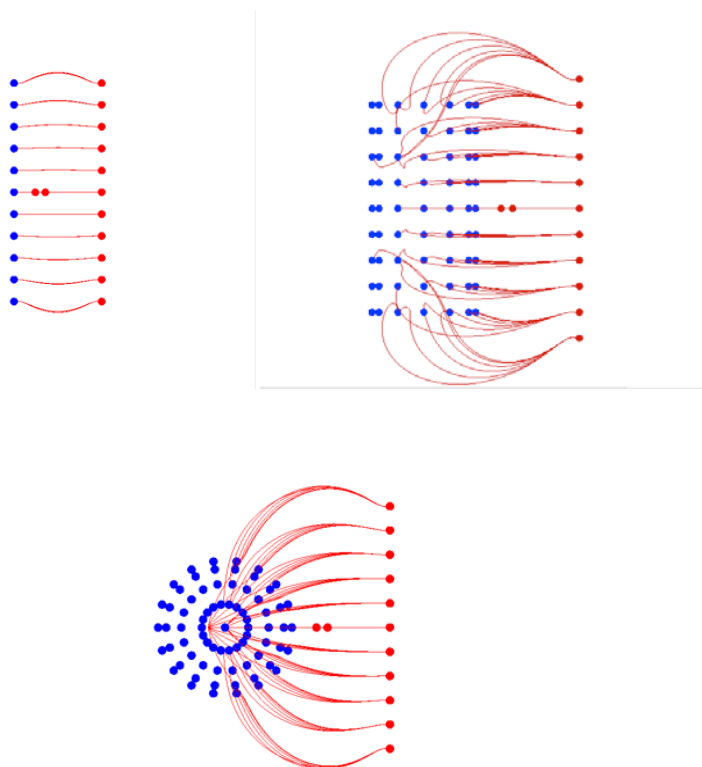


Figure 8-4. Uniform electric field between two plates, and curved electric field between a sphere and a plate. The blue electrode is negatively charged, red electrode is positively charged, and the CO molecule is neutral.

Table 8-2. Summary of results of calculations in absence of an applied electric field

	$r(\text{C-O})$ [Å]	Dipole Moment [D]	$\omega_{\text{CO}}$ [ $\text{cm}^{-1}$ ]
B3LYP/6-311+G**	1.128	0.0714	TBD
CCSD/aug-cc-pVQZ	1.125	0.0712	-
CNDO-II <sup>90</sup>	1.191		3227
experiment <sup>95</sup>	1.128	0.112	2143

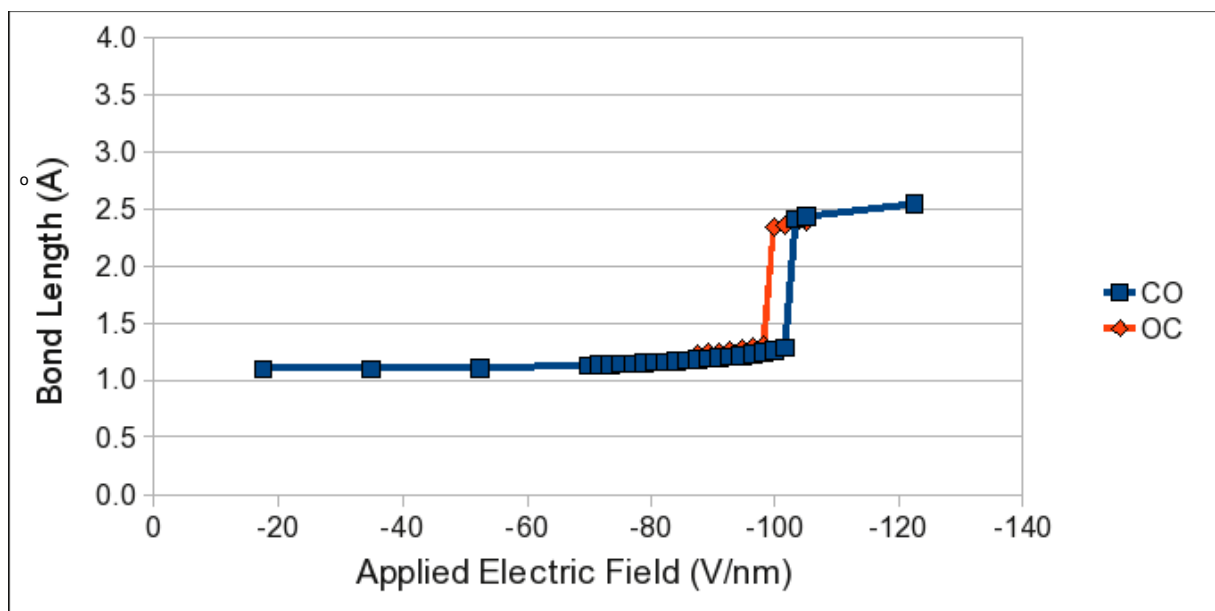


Figure 8-5. Bond length of CO molecule plotted against applied electric field for field created between two charged plates. The blue line shows the results when the carbon atom of the CO molecule is closest to the negatively charged plate, and the red line shows the results when the oxygen atom of the CO molecule is closest to the negatively charged plate.

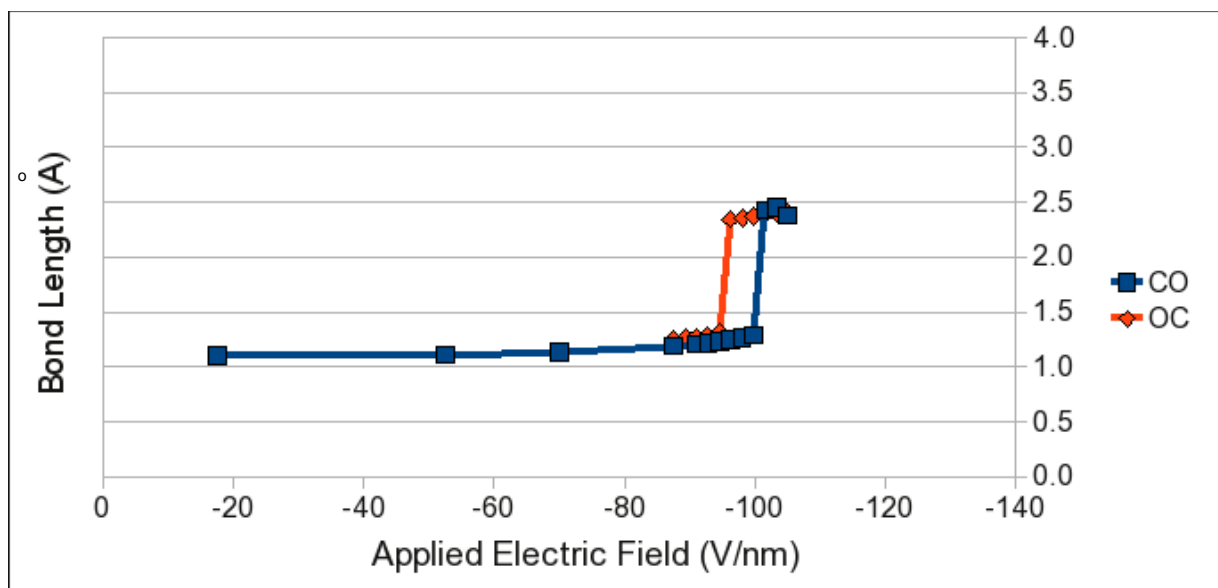


Figure 8-6. Bond length of CO molecule plotted against applied electric field for field created between a charged plate and a charged cylinder. The blue line shows the results when the carbon atom of the CO molecule is closest to the negatively charged plate, and the red line shows the results when the oxygen atom of the CO molecule is closest to the negatively charged plate.

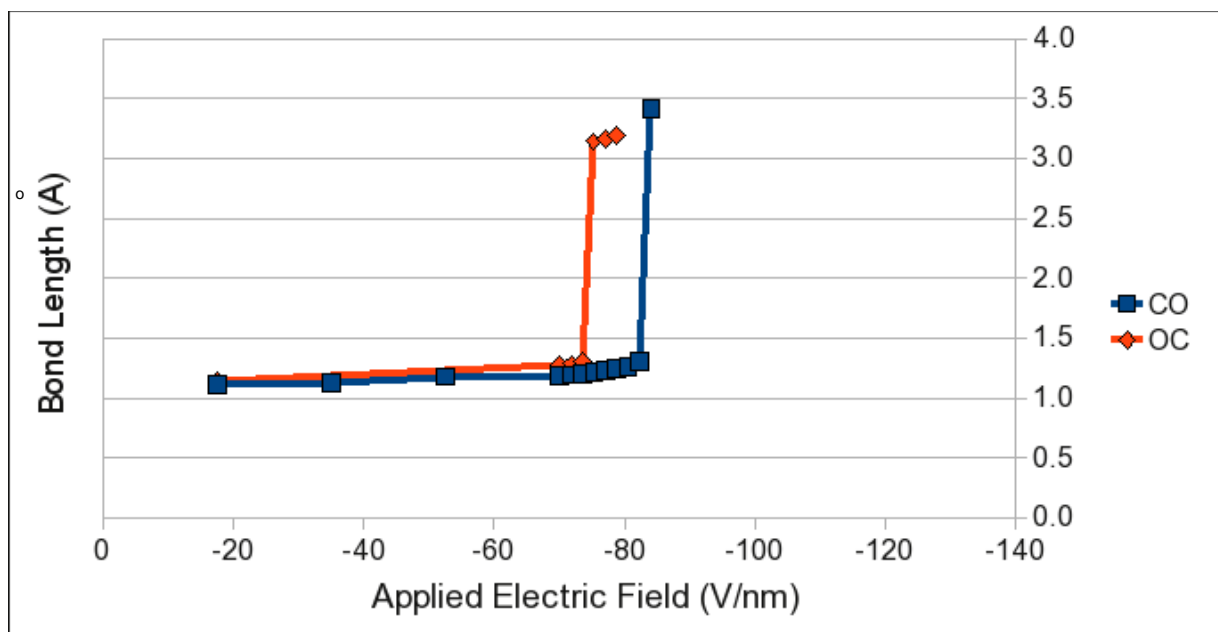


Figure 8-7. Bond length of CO molecule plotted against applied electric field for field created between a charged plate and a charged sphere. The blue line shows the results when the carbon atom of the CO molecule is closest to the negatively charged plate, and the red line shows the results when the oxygen atom of the CO molecule is closest to the negatively charged plate.

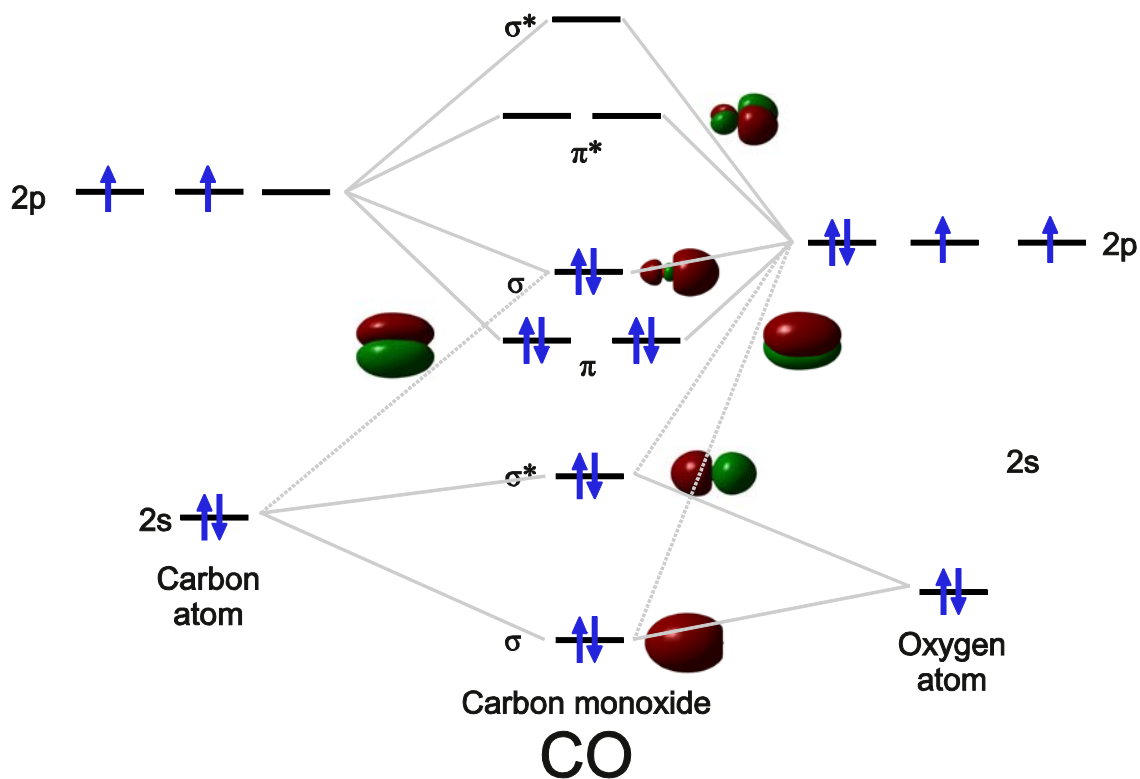


Figure 8-8. Molecular orbital diagram for carbon monoxide. Graphics next to the energy levels show representations of the shapes of the molecular orbitals with the two phases marked in different colors.

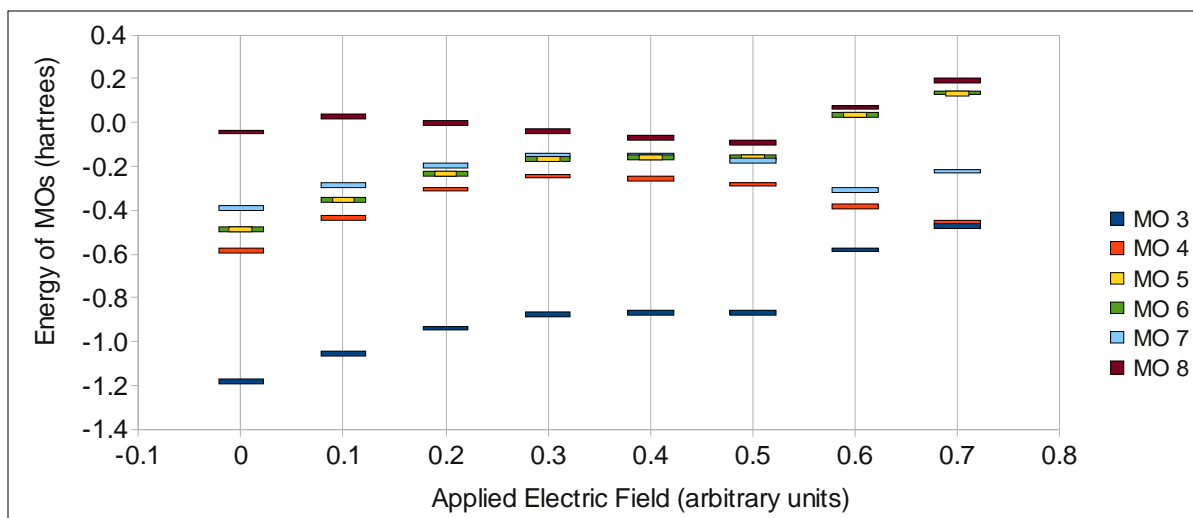


Figure 8-9. Energy of the molecular orbitals in the CO molecule as an external, axial electric field is applied. Note that the pi bonding orbitals (MO5 and MO6, green and yellow) begin at a lower energy than the sigma orbital (MO7, light blue), and then switch to a higher energy as the bond breaks. In this scenario, the bond breaks at an applied electric field of 0.585.

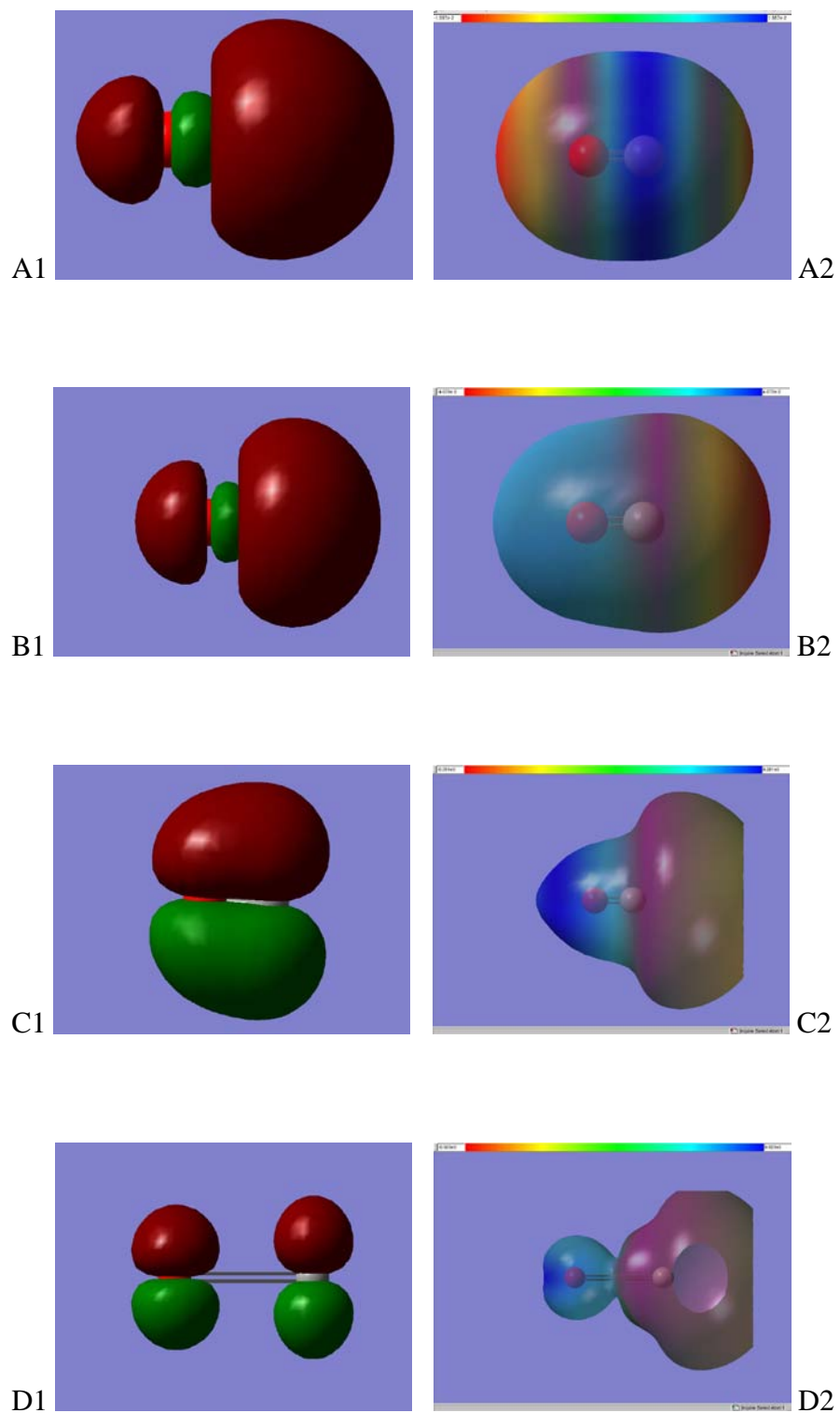


Figure 8-10. The figures in the left column (1) show the shapes of the highest occupied molecular orbitals, and the figures in the right column (2) show the total electron density projected onto a surface where the blue end of the spectrum

is a negative charge and red is a positive charge. The applied field is increased as the figures progress. In A, there is no applied field. In B, the applied field is -17V/nm. In C, the applied field is -84V/nm which is just before the bond breaks. In D, the applied field is -86V/nm which is just after the bond breaks. In all figures, the carbon atom is shown in gray and the oxygen atom is shown in red.

Table 8-3. Calculation summary for dinitrogen molecule.

<b>Calculation</b>	<b>Applied Electric Field to Break CO Bond [V/nm]</b>
Gaussian uniform field	118.2
Two plates	121.1
Plate and cylinder	115.9
Plate and sphere	91.5

## CHAPTER 9 CARBON NANOTUBE SUPERCAPACITORS

Described here are molecular dynamics simulations of supercapacitors based on carbon nanotube forests modeled at a molecular level. Results from calculations focusing on the ionic response of the nanotube-electrolyte assembly in the presence of an applied electric field are presented. Since the various factors included in these simulations are precisely defined, these results can be helpful in disentangling distinct physical factors which contribute to the performance of these materials.

### **System Composition**

A typical capacitor has two plates with an electrolyte between them (where the energy is stored) that is made up of a dielectric and an ionic liquid. When one of the plates on the capacitor is charged, the ions of opposite charge are attracted to the plate, forming a charge layer. On the outside of this layer ions of the opposite charge of the charge layer (the same charge as the electrode) are then attracted, forming a double-charge layer. This is depicted in Figure 9-1. The Debye screening length is the length where we no longer see the effect of the charge on the plate, and the electrolyte looks more like it would in an uncharged capacitor. In other words, the Debye length is the scale over which mobile charge carriers (e.g. electrons) screen out electric fields or the distance over which significant charge separation can occur.

We used a charged carbon nanotube (CNT) as the electrode. The main electrolyte system that we tested was made up of acetonitrile as the dielectric ( $\text{CH}_3\text{CN}$ , abbreviated ACN), and boron tetrafluoride ( $\text{BF}_4^-$ ) with tetraethylammonium ion ( $\text{C}_8\text{H}_{20}\text{N}^+$ , abbreviated TEA<sup>+</sup>) as the ionic liquid. Pictures of these molecules are shown in Figure 9-2. A view of the entire system put together with the electrolyte surrounding the CNT is shown in

Figure 9-3. The system components are placed in a periodic box that is  $25\text{\AA} \times 25\text{\AA} \times 25\text{\AA}$  and filled with the electrolyte with the molecules placed randomly, which were generated by packmol,<sup>96</sup> a program for packing optimization for molecular dynamics simulations.

### Calculation Details

We used a section of (5,5) armchair CNT comprising 390 carbons with a C–C tube diameter of 0.67 nm and length of 4.7 nm. A total charge of  $Q = ne$ , with  $n$  and other simulation details listed in Table 9-1, was distributed uniformly among the 390 CNT atoms so that each atom carried a charge of  $ne/390$ , to mimic the charged/discharged behavior of the capacitor. These charged conditions represent a charge density ranging from  $-0.23$  to  $0.23$  C/m<sup>2</sup>. Partial charges are assigned to atomic sites TEA<sup>+</sup> and BF<sub>4</sub><sup>-</sup> ions according to the recommendations of Luzhkov et al.<sup>97</sup> and Andrade et al.,<sup>98</sup> respectively. All the other parameters are taken from general AMBER force field (GAFF).<sup>99</sup> After the number of dielectric molecules were chosen to represent various densities, the numbers of BF<sub>4</sub><sup>-</sup> or TEA<sup>+</sup> ions were adjusted to constitute a neutral system including the charge  $n$  on CNT. We typically sought bulk electrolyte concentrations in the middle of the pores (the space between the tubes) near 1.0 M.<sup>100</sup> Table 9-1 gives specific ion/molecule numbers; note that cases 6 and 10 correspond to significantly higher concentrations. To investigate the effect of pore size, we simulated smaller systems, with shorter CNT–CNT distances, containing therefore less ACN and fewer TEA<sup>+</sup> BF<sub>4</sub><sup>-</sup> ions, as listed in Table 9-1. Trajectories were constructed with a time step of 2 fs, using the isothermal ensemble with the Langevin thermostat. Temperature and pressure were 300 K and 1 atm. The simulations were performed with AMBER9.<sup>101</sup>

Electrostatic interactions were calculated using particle mesh Ewald with a grid spacing of 1 Å. All simulations lasted 30 ns, with the first 10 ns discarded as aging. We confirmed that this equilibration was satisfactory by extending one calculation (Case 3) for another 5 ns using parallel tempering utilizing temperatures of 300, 325, 345, and 360 K. Study of systems with the same electrolyte concentration and CNT charge density but with a CNT length of 9.6 nm confirmed that the present results do not depend on CNT length. Separate calculations on homogeneous liquid propylene carbonate verified that this model gives an accurate value for the linear response dielectric constant and its temperature dependence.<sup>102</sup> Results were analyzed by calculating the radial distribution of ions and investigating how the double layer changed based on a variety of effects relating to the charge on the CNT, density of ions present, etc. The time dependence of these effects was also analyzed. Based on the radial distribution function, the charge density was calculated and Poisson's equation was used to calculate the electric field.

## **Results and Discussion**

### **Acetonitrile Electrolyte System**

In this section, the results for the electrolyte system consisting of tetraethylammonium ion ( $\text{TEA}^+$ ), boron tetrafluoride ion ( $\text{BF}_4^-$ ), and acetonitrile (ACN) are discussed. Table 9-1 gives the specific ion/molecule numbers used in each case as well as the charge on the CNT. We typically sought bulk electrolyte concentrations near 1.0M.<sup>100</sup>

### **Difference between positively and negatively charged CNT**

In Figure 9-4A, the CNT is negatively charged which means that the  $\text{TEA}^+$  ions are attracted to the CNT. The large  $\text{TEA}^+$  ions take up all the space in the radii closest to

the CNT. Moving outwards, next there is a small peak of ACN molecules trapped between the  $\text{TEA}^+$  and  $\text{BF}_4^-$  layers. After the two charged layers, there is hardly any concentration of charged ions and the ACN is distributed relatively evenly throughout the rest of the solvent. In Figure 9-4B, the CNT is positively charged which means the  $\text{BF}_4^-$  ions are attracted to the CNT. In this case, it appears that the ACN molecules were polarized and also attracted to the CNT and are “pinned” near the CNT wall. This is possible because the  $\text{BF}_4^-$  molecules are smaller and can move through gaps in the array formed by ACN molecules. This is not possible in the opposite case since the relative size of the  $\text{TEA}^+$  molecules is so large. Also, in the positively-charged CNT case, there are no ACN molecules in between the charged layers.

When the CNT is negatively charged (Figure 9-5A), there is a  $\text{TEA}^+$  peak for about 1000 times the bulk density. The same is seen in a positively charged CNT (Figure 9-5B) with a  $\text{BF}_4^-$  peak of about 1000 times the bulk density. However, in the second case, we see a more pronounced  $\text{TEA}^+$  forming the double charge layer. This is because of the relative sizes of the ions as described above.

### **Decreasing charge on CNT**

In Figure 9-6, the charge on the CNT is decreasing and (to compensate for an overall balanced charge) the number of  $\text{BF}_4^-$  ions is increasing. The decreasing charge on the CNT has an effect that one would expect. The ratio of the density of  $\text{BF}_4^-$  at a radius close to the CNT to the bulk density decreases as the charge on the CNT is decreased. We also start to see a double layer formed as the number of  $\text{BF}_4^-$  ions is increased. When the charge on the CNT is increased from -5 to -14, the density/bulk

density ratio gets 4.5 times larger; this shows what a strong effect charge has on the density of the ions.

### **Discharged CNT**

Figure 9-8 shows the radial distribution of the molecules from the center of a discharged CNT. In the case, we still see a peak of TEA<sup>+</sup> ions after the ACN molecules closest to the nanotube. This peak is small compared to when the CNT is charged (here, ~5 times the bulk density and in the range of several thousand times the bulk density when the CNT is charged). Favorable electrostatic interactions with this initial TEA<sup>+</sup> layer then serve to position the BF<sub>4</sub><sup>-</sup> layer. With no charge on the system, we do not see a double layer. Instead we see the same effect as in other liquid systems, where there is short-range order and long-range disorder.

### **Electric Field of Total System**

In Figure 9-9, the blue line shows the strength of the electric field on the total system as the distance is increased traveling away from the CNT. The contribution coming from the yellow line (positively charged ion, TEA<sup>+</sup>) and the green line (negatively charged ion, BF<sub>4</sub><sup>-</sup>) roughly cancel each other out. The red line (CNT) shows that the electric field is strongest closest to the nanotube, and then decreases with distance. This graph shows that the electric field of the whole system is dominated by the electric field of the CNT when close to the nanotube, and is dominated by the ACN when further away from the nanotube.

Figure 9-10A shows the ion concentration for Case 5, and Figure 9-10B shows the total system line from the same calculation set-up. The positive peak at 7Å in the electric field graph corresponds with the TEA<sup>+</sup> peak at 7Å in the ion density graph. There is also a correlation of negative electric field for the BF<sub>4</sub><sup>-</sup> peak. The oscillations in

the total electric field between positive and negative clearly show the double charge layer.

The effect of increased charge on the CNT on the electric field was also studied. Figure 9-11 shows the electric field calculations for Cases 2, 4, and 5. As one would expect, as the charge on the CNT is increased, the electric field is increased in magnitude, but keeps the same shape.

### **Time dependence of ion distribution**

The time dependence of the TEA<sup>+</sup> ion distribution for Case 3 is shown in Figure 9-12. At the beginning of the calculation, the density of the TEA<sup>+</sup> ions is high, and as the time steps are increased, the peak becomes smaller and smaller. The TEA<sup>+</sup> densities in all the other graphs that we have looked at is the time-averaged density, so it would fall somewhere in the middle of these peaks. This time-dependence was not observed in the BF<sub>4</sub><sup>-</sup> or ACN densities. Overall, it was observed that the time dependence of the formation of the double layer is unimportant. In practice, the rate-determining step for electric double-layer supercapacitors is the flow of the electrolyte between the nanotubes. Once the electrolyte is already surrounding the capacitors, the time for the charging process is negligible.

### **Time dependence of electric field strength**

The time dependence of the TEA<sup>+</sup> ion distribution for Case 3 is shown in Figure 9-13. Corresponding to the time dependence of the ion density, the strength of the electric field created by the TEA<sup>+</sup> ions decreased as time went on. There was also no time dependence observed in the total electric field on the system or the electric field from the CNT and ACN. The greatest effect of time dependence was observed for the TEA<sup>+</sup> ions and the BF<sub>4</sub><sup>-</sup> ions, whose effects likely cancel out.

## Effects of each component

The effect of the dielectric on this system is demonstrated in Figure 9-14. Figure 9-14A shows a charged system with 100 ACN molecules, 26 TEA<sup>+</sup> ions and 12 BF<sub>4</sub><sup>-</sup> ions. Figure 9-14B shows the same system, but without the ACN. In the first case, the TEA<sup>+</sup> and BF<sub>4</sub><sup>-</sup> peaks are separated by the ACN peak. The ACN “fits” in between the two ions because it is the smallest molecule in the system. In the second case the BF<sub>4</sub><sup>-</sup> peak has shifted to the left, closer to the CNT. Now that there is no ACN in the system, the BF<sub>4</sub><sup>-</sup> peak is wider and right next to the TEA<sup>+</sup> ions. The TEA<sup>+</sup> peak has not changed.

Figure 9-15 shows the difference between a charged and uncharged system with only the ions surrounding the CNT. Figure 9-15A has no charge on the CNT, and Figure 9-15B has a charge of -14. When the charge is applied, a double charge layer is clearly formed even without the presence of a dielectric (ACN).

Finally, a system with only the dielectric and no charge is studied in Figure 9-16. Even in a system with only ACN and no charge, the ACN still stays close to the edge of the CNT, which is the effect we saw when there were other components in the electrolyte as well. This is likely due to electrostatic attraction by surface charges.

## Water Electrolyte System

Another system with a different electrolyte made up of potassium ion (K<sup>+</sup>), sulfate ion (SO<sub>4</sub><sup>-2</sup>), and water (H<sub>2</sub>O) was also studied. Potassium sulfate was chosen based on experiments currently being performed by our experimental collaborators in MPA-STC and MPA-11 at Los Alamos National Laboratory (LANL). Table 9-2 shows the ratios of ions that were tested, corresponding to molarities of 0.1, 0.5, and 1.0M.

In this system, it was found that at higher molarity, ion pairs are formed near the nanotube, followed by a layer of positive ion, and then ion pairs again when the nanotube was negatively charged (shown in Figure 9-17). The results for when the nanotube is negatively charged is shown in Figure 9-18. Here, at low molarity, we see an  $\text{SO}_4^-$  peak next to the positively charged nanotube followed by a layer of paired ions. At higher molarity, we see a much smaller peak in the negative ion close to the nanotube. The peak is now relatively the same height as the water peak. Like in the lower molarity case, this initial negative peak is followed by a layer of paired ions.

The graphs in Figure 9-19 show systems at the same molarity with a different charge on the nanotube. In both the negatively and positively charged case, there is a small layer of water followed by a layer of paired ions. However, in the case of the positively charged nanotube, there is more water near the nanotube wall and the layer is thicker. When there is no charge on the nanotube, as in Figure 9-20, we see that there is a layer of water before there is a layer of ions. Also, all three species are approximately at the bulk density throughout the whole system.

Figure 9-21 shows the electric field of the total system with a negatively charged CNT (A) and a positively charged CNT (B). The blue line is the electric field of the total system and the other colored lines each represent the contribution of each species to the electric field. The effects of the positive and negative ions (yellow and green lines, respectively) roughly cancel each other out. Therefore, the electric field of the entire system is mainly dependent on the water. The same is true when there is a positive charge on the carbon nanotube: The electric field of the entire system when there is no charge applied to the nanotube is shown in Figure 9-22. The charge here is solely from

the ions. Here we see charge layers forming even without applied charge. It appears that there is a layer of positive ions close to the nanotube wall followed by a layer of negative ions, and two small echoing charge layers as well. There is no net electric field far away from the nanotube wall.

## Polarization

In the previous calculations, the effect of the polarization on each molecule was not represented in the force field. Different calculations, like the ones described below, need to be done in order to take this effect into account. This will help determine which molecules are more polarizable so we can focus on these molecules (if there is an effect) when modifying the force field in future work in order to have a more complete understanding of how the molecules in an actual carbon nanotube supercapacitor would behave.

The polarization on each molecule was calculated by the *Gaussian 09* software<sup>93</sup> using a 6-311+G\*\* basis set and a PBE1PBE functional. This software calculates the polarization using Equation 9-1.

$$\hat{H} = \hat{H}_0 - \sum_q \hat{\mu}_q \varepsilon_q - \frac{1}{3} \sum_{q,q'} \hat{\Theta}_{q,q'} \frac{\partial \varepsilon_q}{\partial q'} - \dots \quad (9-1)$$

The additional term added to the Hamiltonian reflects the interaction of the molecular electron density with the external field,  $\varepsilon$ . The electron density is expressed as a multipole expansion: the first term is the dipole operator, the second term is the quadrupole moment operator, and so on.

We tested each molecule by itself 7Å away from the center of a cylinder made up of point charges representing a CNT. The electron density of each molecule is shown in Figure 9-23. When an ACN molecule was placed next to a CNT, with the long axis of

the molecule pointed towards the nanotube, there was no change in the dipole moment regardless of the charge on the CNT (~4.06 Debye). However, the molar volume was increased (from 430 cm<sup>3</sup>/mol to 462 cm<sup>3</sup>/mol, which is an increase of 7%) when the positive dipole of the molecule was aligned closest to the negatively charged CNT, and vice versa. The smaller molecular volume was calculated when the dipole was aligned so that the charge closest to the CNT was the same sign as the charge on the CNT. No change in molecular volume or dipole was observed when the dipole was aligned along the perpendicular axis to the CNT surface.

In the calculation done with BF<sub>4</sub><sup>-</sup> and a charged CNT, it was found that the dipole and molar volume both increased for both a negatively and positively charged CNT (0.3409 Debye and 45 cm<sup>3</sup>/mol) when compared to the dipole and molar volume of a BF<sub>4</sub><sup>-</sup> molecule on its own (0.0042 Debye and 41 cm<sup>3</sup>/mol). So, the molar volume was slightly larger (9% increase) and the dipole was increased by more than 80 times when the BF<sub>4</sub><sup>-</sup> molecule was placed near a charged CNT. Calculations done on a sulfate molecule (SO<sub>4</sub><sup>-2</sup>) had similar results, as the molecules are very similar. The same effect was seen for the TEA<sup>+</sup> ion: with a normal molecular volume of 1472 cm<sup>3</sup>/mol and a molecular volume of 1516 cm<sup>3</sup>/mol when placed near a charged CNT (3% increase), and a normal dipole moment of 0.0002 Debye and a dipole moment of 0.1003 Debye when placed near a CNT (500 times larger than when not near a charged CNT).

### **Conclusions**

We studied the effects on the molecules in the electrolyte surrounding a charged carbon nanotube. We were able to see a clear charge double layer in CNT when a field was applied. Differences in the distribution of the ions were found for positively and

negatively charged systems that were found to be dependent on the relative size of the ions in the electrolyte. It was also found that the total electric field on the system was controlled by the charge on the CNT at a short range and then by the charge on the dielectric at a long range. Similar effects were seen for both the acetonitrile electrolyte system and the water electrolyte system. The effects of the polarization of each individual molecule were studied, and it was found that the dipole on the ions when near a charged CNT was 80-500 times larger than the dipole of the atoms normally. No significant change in the molar volume of the electrolyte molecules due to the charged CNT was calculated.

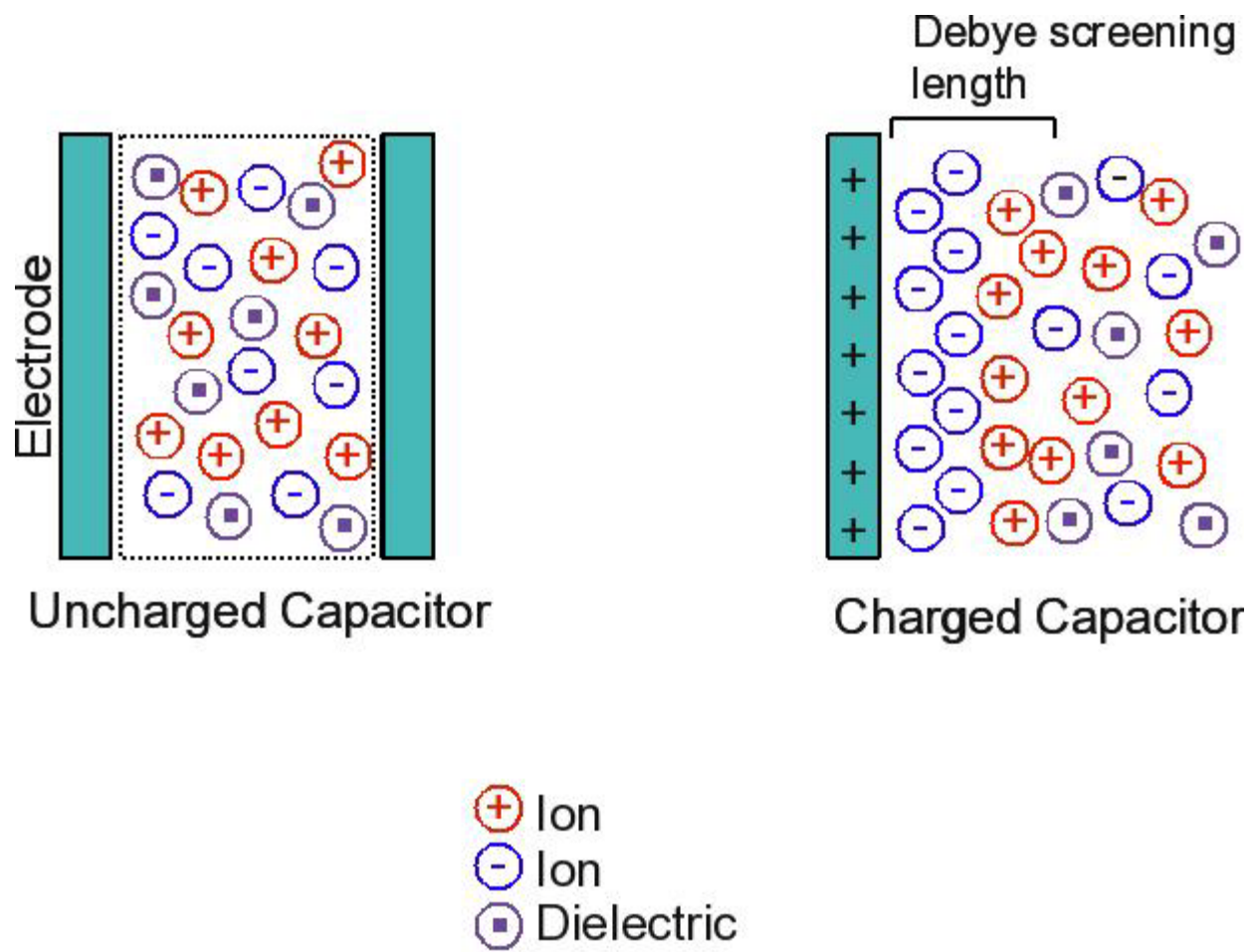
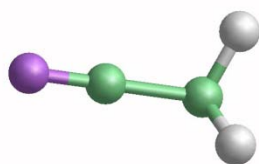
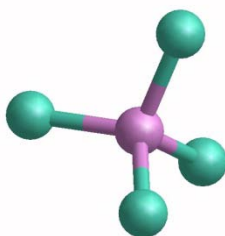


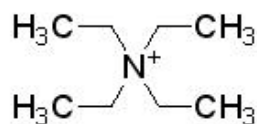
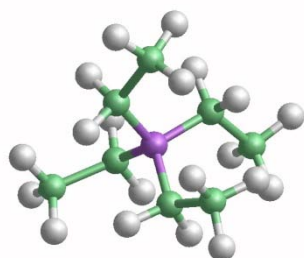
Figure 9-1. Uncharged and charged capacitors. A double layer can be seen formed in the charged capacitor.



A



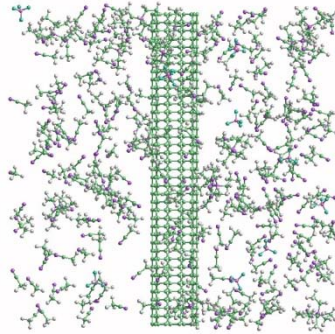
B



C

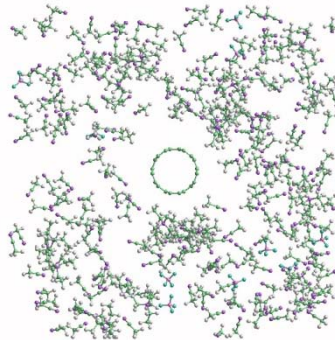
Figure 9-2. Molecules that make up the electrolyte solution surrounding the carbon nanotube. A) acetonitrile ( $\text{CH}_3\text{CN}$ , abbreviated ACN) where C atoms are green, N atoms are purple, and H atoms are white, B) boron tetrafluoride ( $\text{BF}_4^-$ ) where B atoms are pink and F atoms are teal, C) tetraethylammonium ion ( $\text{N}(\text{C}_2\text{H}_5)_4$ , abbreviated  $\text{TEA}^+$ ) where C atoms are green, N atoms are purple, and H atoms are white.

z  
y  
x



normal A

z  
y  
x



normal B

Figure 9-3. Entire carbon nanotube supercapacitor system with carbon nanotube in center surrounded by electrolyte. Diameter of CNT is 0.67 nm and length is 4.7 nm. A) view from side, B) view from top.

Table 9-1. Calculation summary.

Case #	Charge on CNT	Number of ACN	Number of TEA <sup>+</sup>	Number of BF <sub>4</sub> <sup>-</sup>
1	-14	500	26	12
2	-14	250	15	1
3	14	500	12	26
4	-10	250	15	5
5	-5	250	15	10
6	-14	100	26	12
7	0	500	26	26
8	0	0	26	26
9	-14	0	12	26
10	0	100	0	0

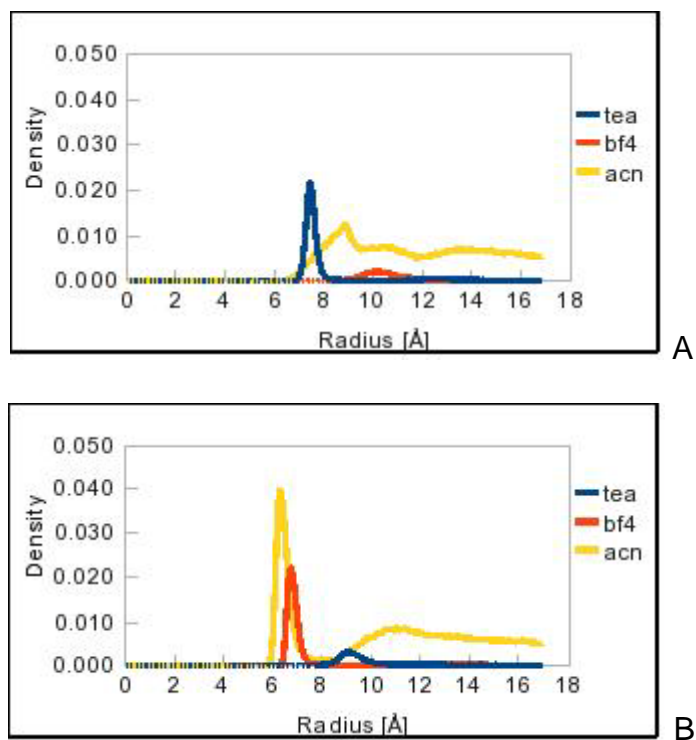


Figure 9-4. Difference between positively and negatively charged CNT. A) Case 1 (charge is -14, 500 ACN, 26 TEA, 12 BF<sub>4</sub>), B) Case 3 (charge is +14, 500 ACN, 26 TEA, 12 BF<sub>4</sub>).

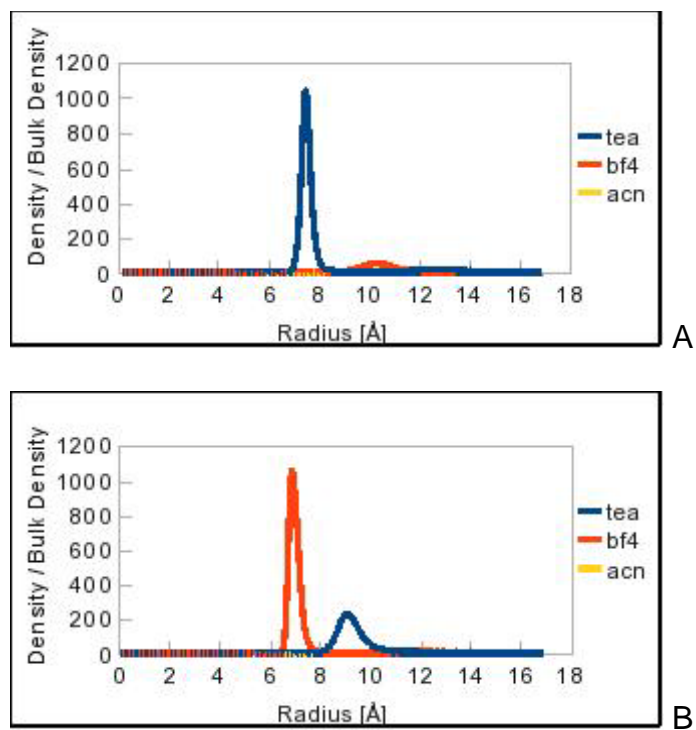


Figure 9-5. Difference between positively and negatively charged CNT, density / bulk density. A) Case 1 (charge is -14, 500 ACN, 26 TEA, 12 BF<sub>4</sub>), B) Case 3 (charge is +14, 500 ACN, 26 TEA, 12 BF<sub>4</sub>).

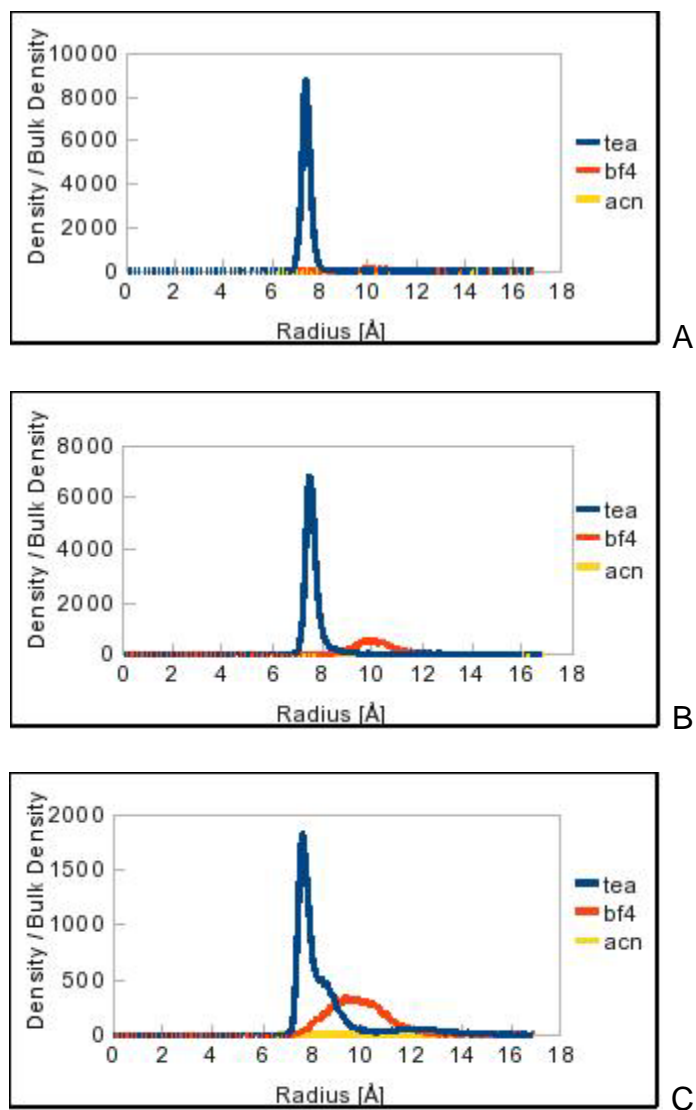


Figure 9-6. Decreasing charge on CNT. A) Case 2 (charge is -14, 250 ACN, 15 TEA, 1 BF<sub>4</sub>), B) Case 4 (charge is -10, 250 ACN, 15 TEA, 5 BF<sub>4</sub>), C) Case 5 (charge is -5, 250 ACN, 15 TEA, 10 BF<sub>4</sub>).

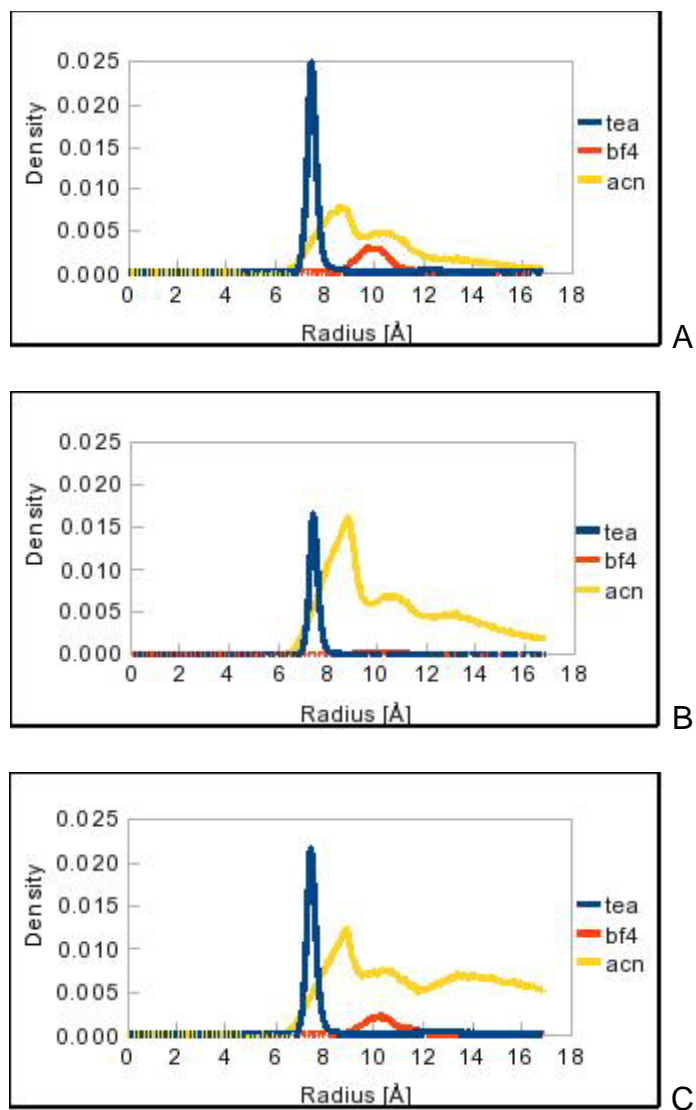


Figure 9-7. Increasing density. A) Case 6 (charge is -14, 100 ACN, 26 TEA, 12 BF<sub>4</sub>), B) Case 2 (charge is -14, 250 ACN, 15 TEA, 1 BF<sub>4</sub>), C) Case 1 (charge is -14, 500 ACN, 26 TEA, 12 BF<sub>4</sub>).

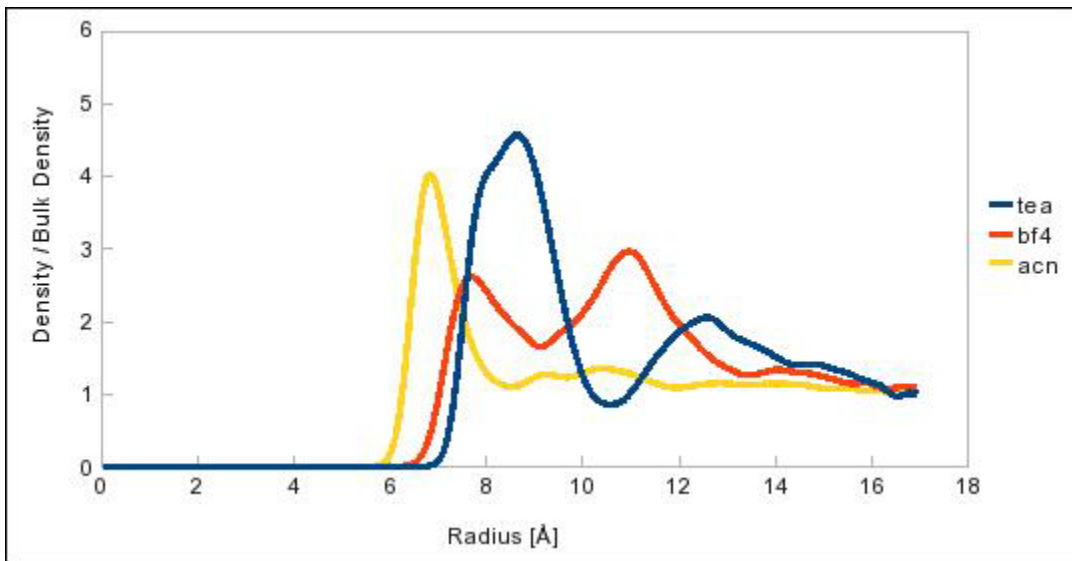


Figure 9-8. Discharged CNT (Case 7, no charge, 500 ACN, 26 TEA, 26 BF<sub>4</sub>).

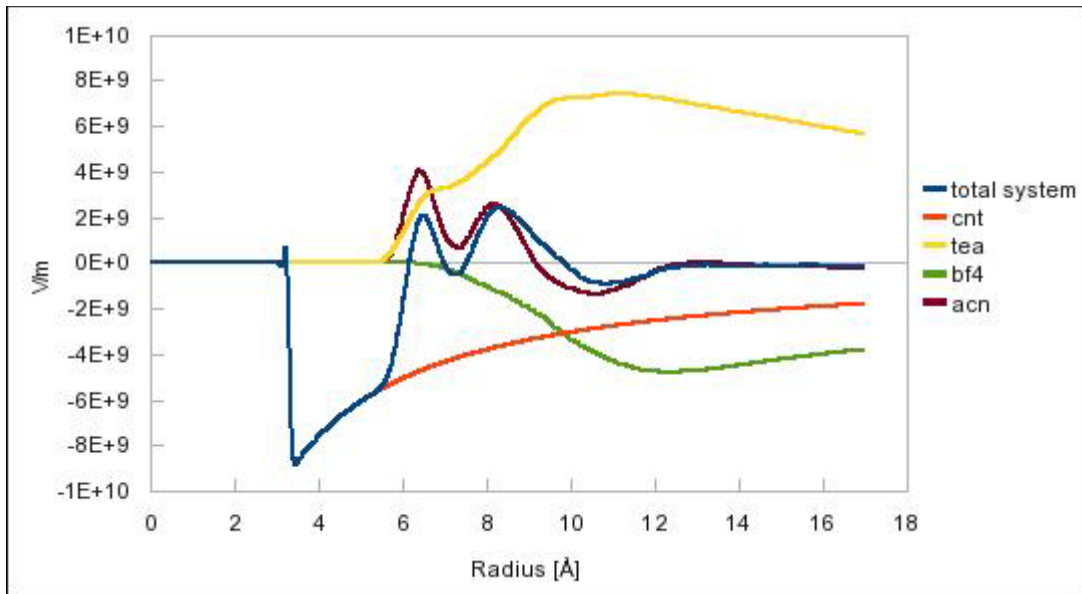


Figure 9-9. Electric field of total system (Case 5, charge is -5, 250 ACN, 15 TEA, 10 BF<sub>4</sub>).

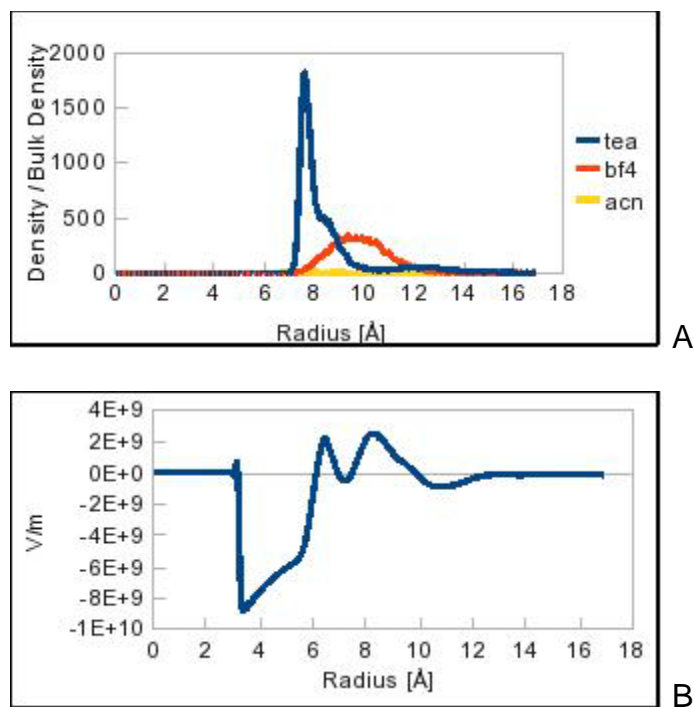


Figure 9-10. Electric field effects. A) Radial distribution function for Case 5 (charge is -5, 250 ACN, 15 TEA, 10 BF<sub>4</sub>), B) Charge on Case 5 (charge is -5, 250 ACN, 15 TEA, 10 BF<sub>4</sub>).

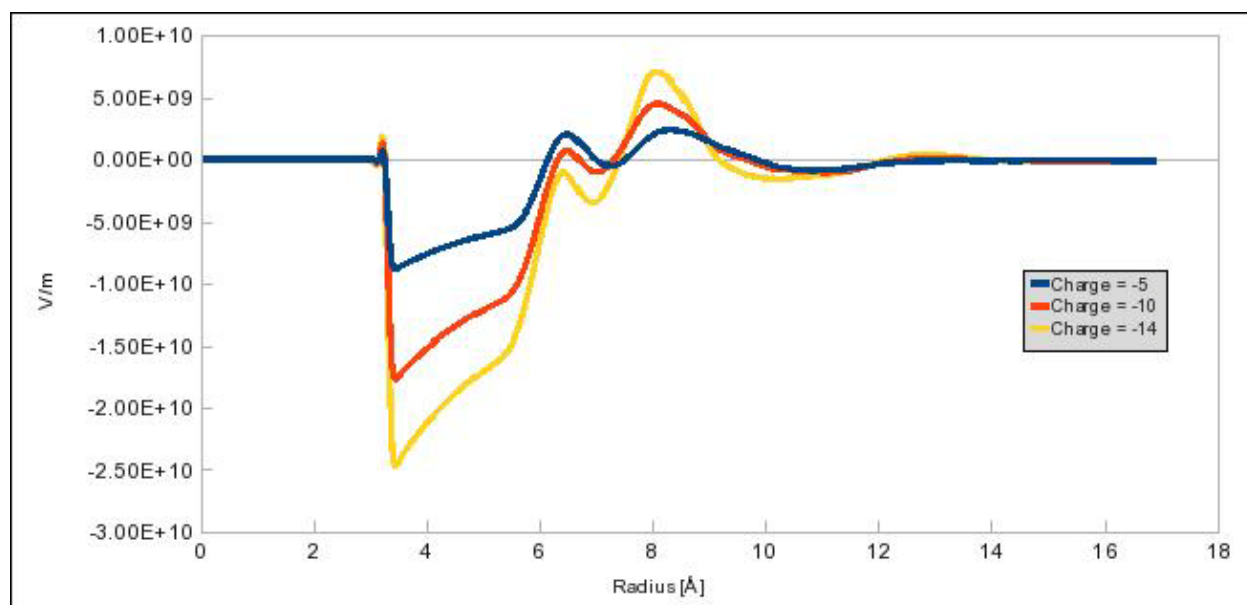


Figure 9-11. Effect of increased CNT charge on applied field. (Case 2, charge is -14, 250 ACN, 15 TEA, 1 BF<sub>4</sub>), (Case 4 charge is -10, 250 ACN, 15 TEA, 5 BF<sub>4</sub>), (Case 5, charge is -5, 250 ACN, 15 TEA, 10 BF<sub>4</sub>).

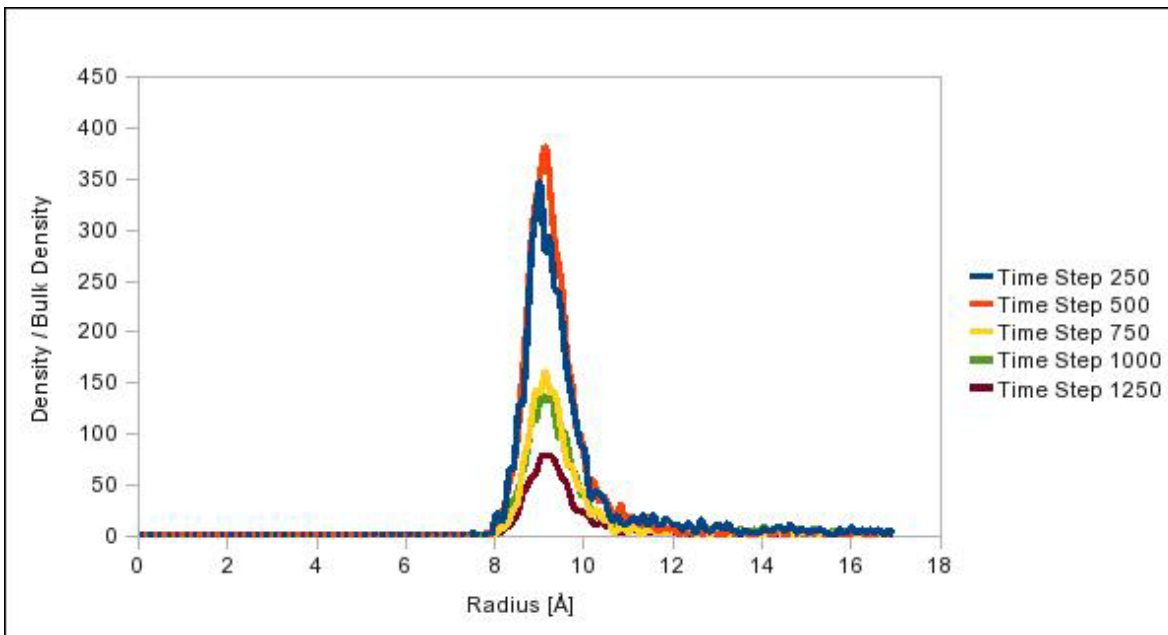


Figure 9-12. Time dependence of the distribution of ions for Case 3 (charge is 14, 500 ACN, 12 TEA, 26  $\text{BF}_4$ ).

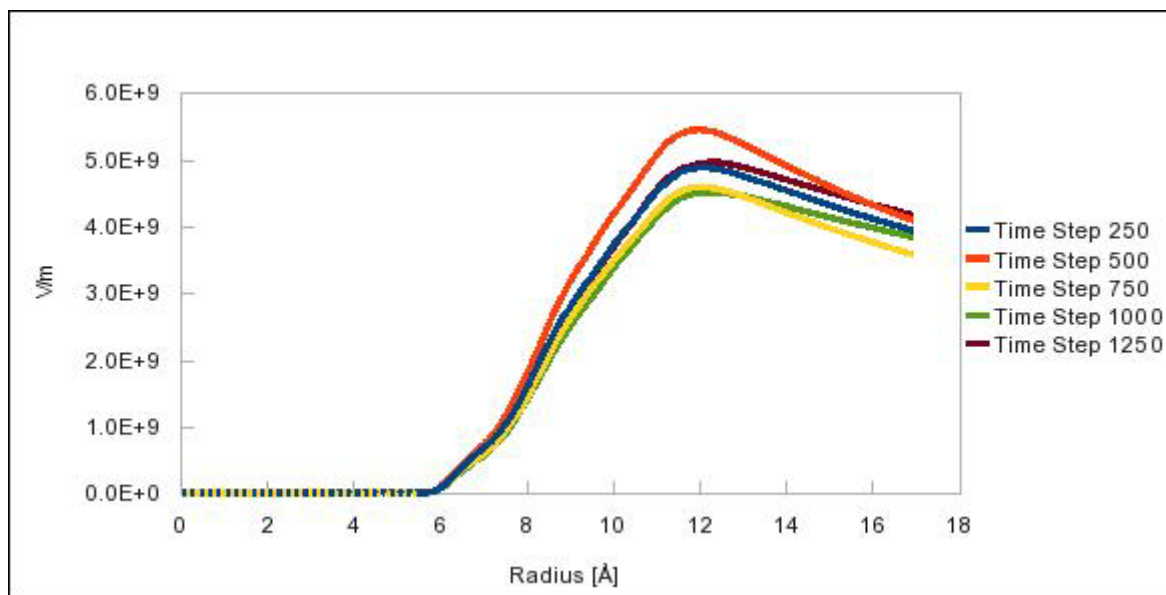


Figure 9-13. Time dependence of the electric field strength for Case 3 (charge is 14, 500 ACN, 12 TEA, 26  $\text{BF}_4$ ).

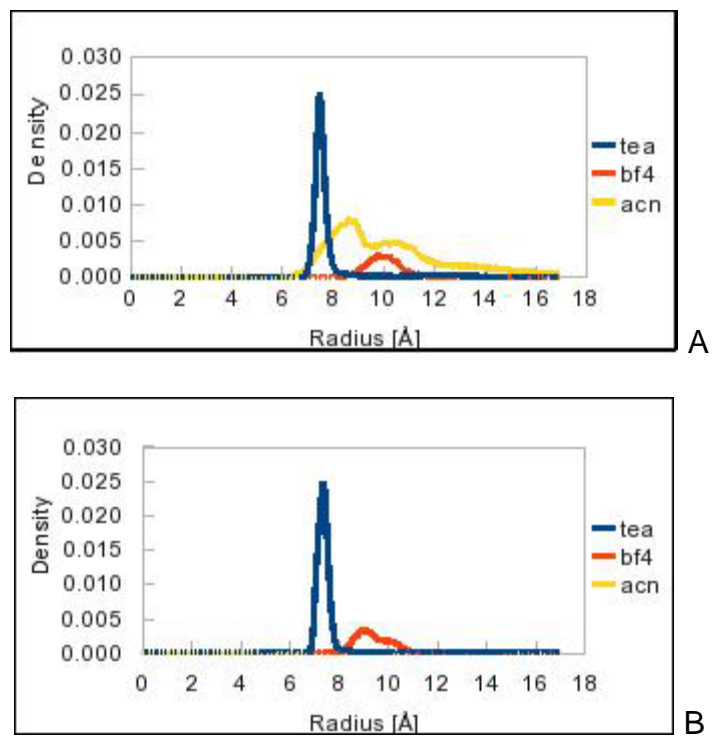


Figure 9-14. System with and without dielectric present. A) Case 6 (charge is -14, 100 ACN, 26 TEA, 12 BF<sub>4</sub>), B) Case 9 (charge is -14, 0 ACN, 26 TEA, 12 BF<sub>4</sub>).

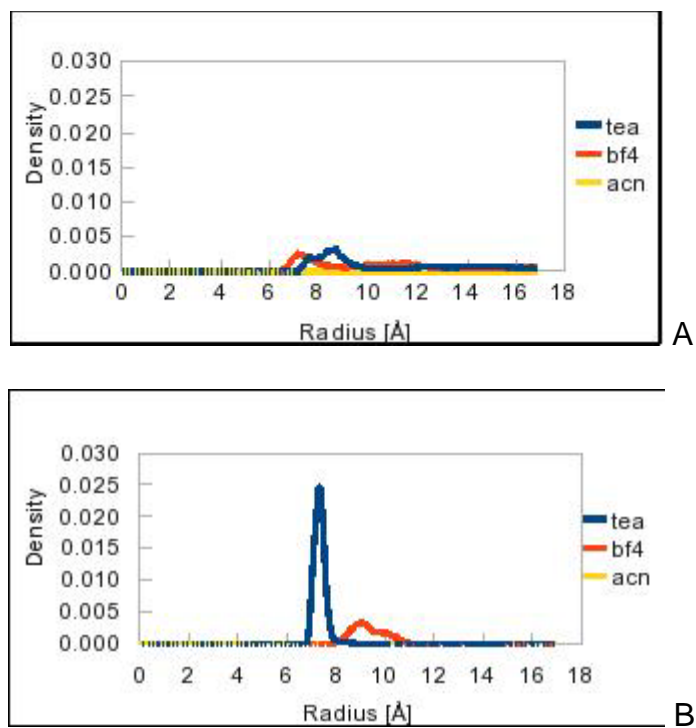


Figure 9-15. Charge and uncharged system with ions only, no dielectric. A) Case 8 (no charge, 0 ACN, 26 TEA, 26 BF<sub>4</sub>), B) Case 9 (charge is -14, 0 ACN, 26 TEA, 12 BF<sub>4</sub>)

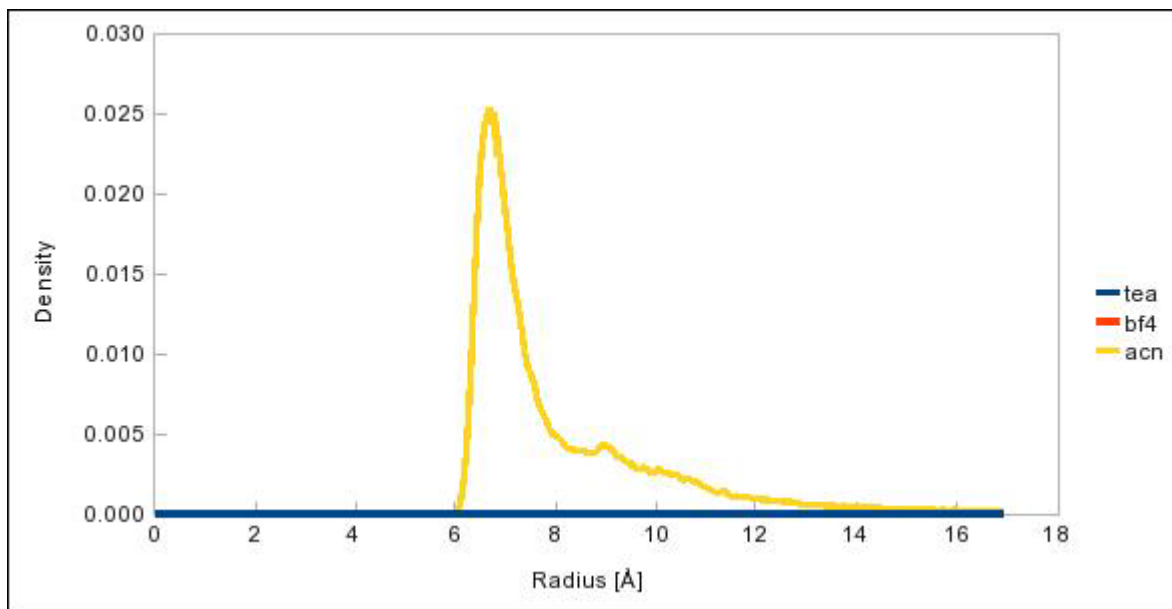


Figure 9-16. Surface attraction for Case 10 (no charge, 100 ACN, 0 TEA, 0 BF<sub>4</sub>).

Table 9-2. Calculation Summary for K<sub>2</sub>SO<sub>4</sub> electrolyte

Case #	Charge on CNT	Number of H <sub>2</sub> O	Number of K <sup>+</sup>	Number of SO <sub>4</sub> <sup>-</sup>	Molarity [M]
1	-14	3342	26	6	0.1
2	-14	3342	74	30	0.5
3	-14	3342	134	60	1
4	14	3342	12	13	0.1
5	14	3342	60	37	0.5
6	14	3342	120	67	1
7	0	3342	12	6	0.1

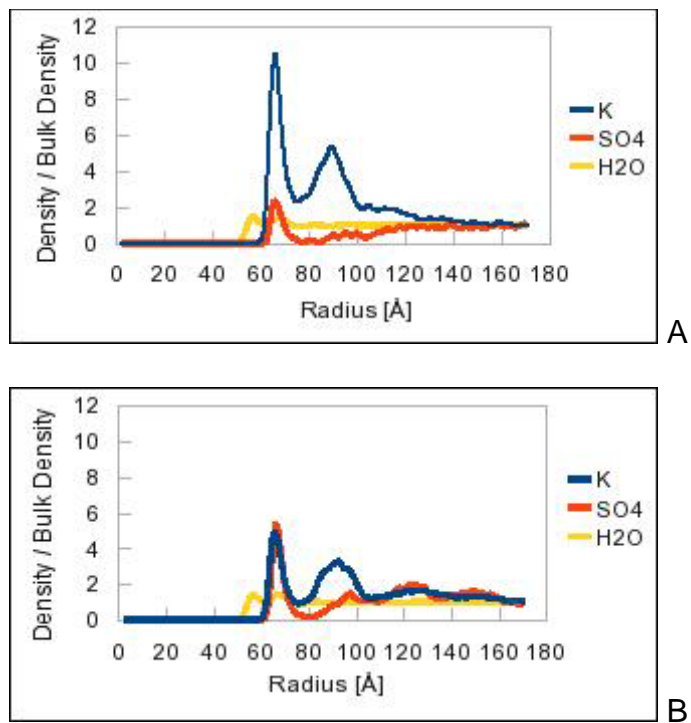


Figure 9-17. Effect of increasing molarity for a negatively charged nanotube. A) Case 1 (charge is -14, 34 K<sup>+</sup>, 6 SO<sub>4</sub>, 0.1M), B) Case 2 (charge is -14, 74 K<sup>+</sup>, 30 SO<sub>4</sub>, 0.5M).

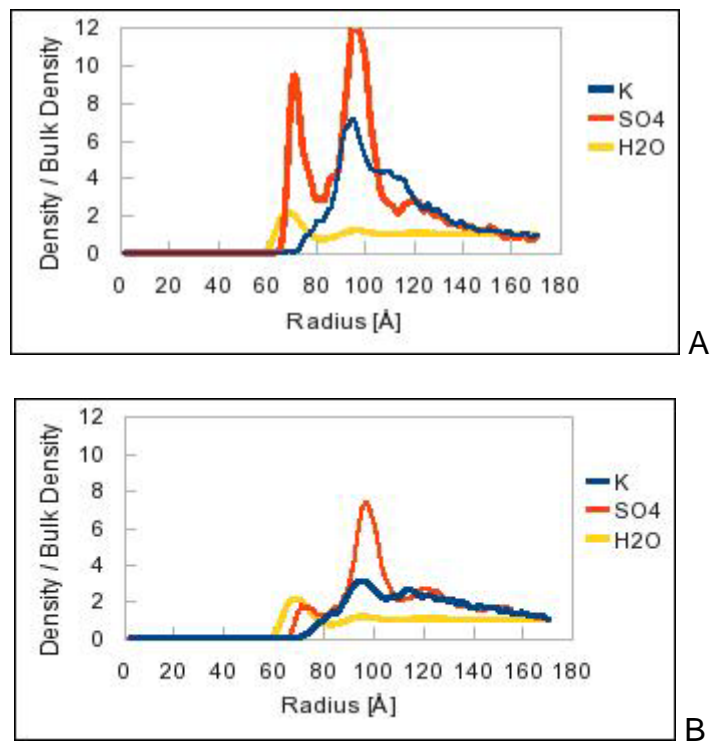


Figure 9-18. Effect of increasing molarity for a positively charged nanotube. A) Case 4 (charge is 14, 12 K<sup>+</sup>, 13 SO<sub>4</sub>, 0.1M), B) Case 5 (charge is 14, 60 K<sup>+</sup>, 37 SO<sub>4</sub>, 0.5M).

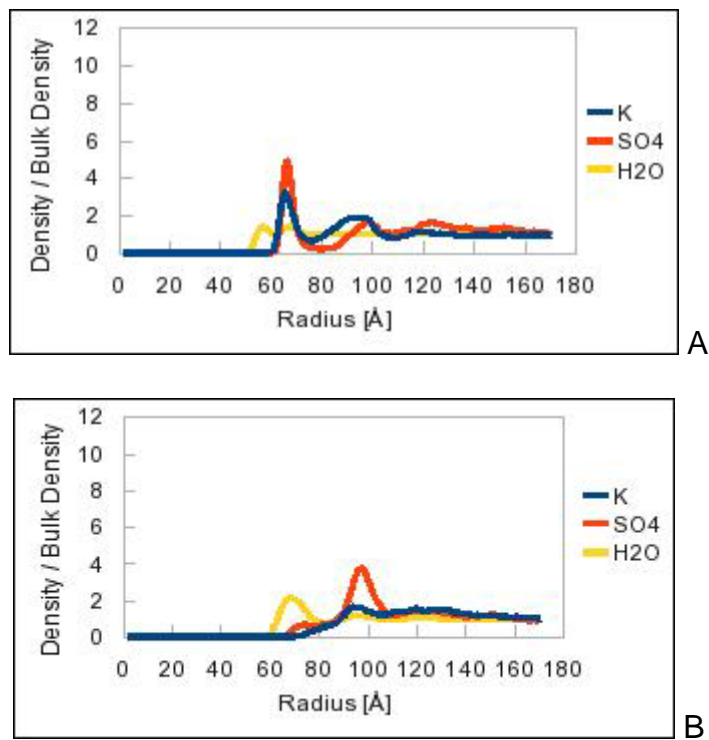


Figure 9-19. Difference between positively and negatively charged nanotube at the same molarity. A) Case 3 (charge is -14, 134  $K^+$ , 60  $SO_4$ , 1.0M), B) Case 6 (charge is 14, 120  $K^+$ , 67  $SO_4$ , 1.0M).

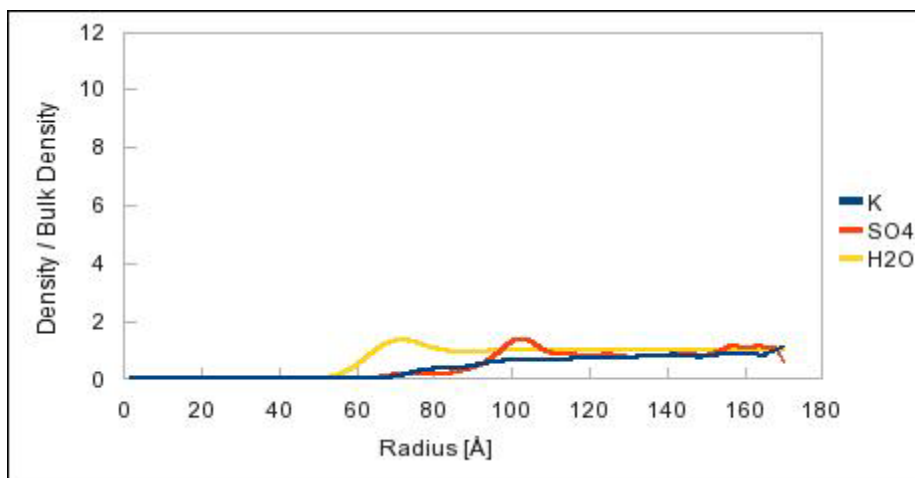
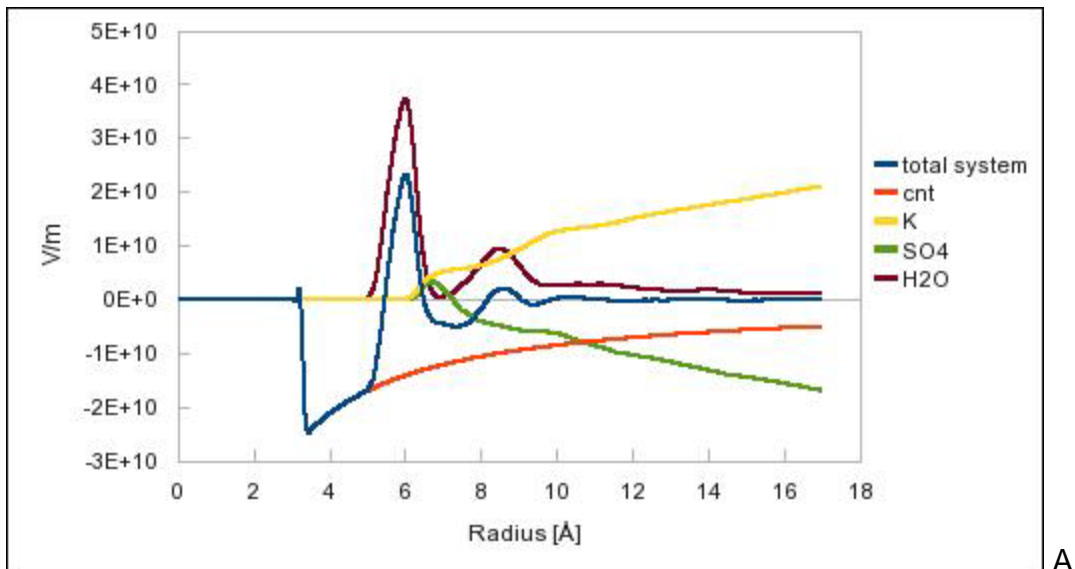
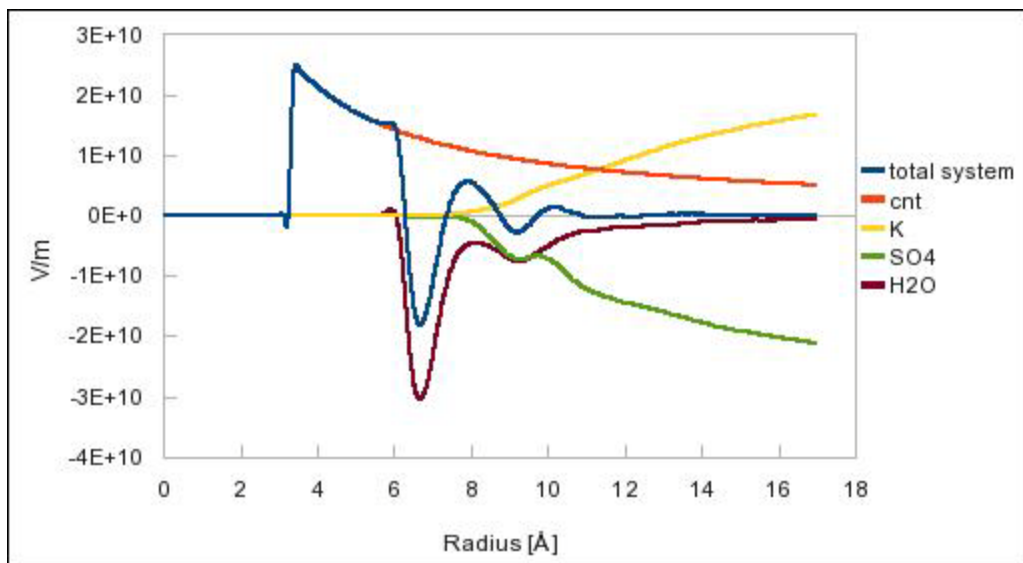


Figure 9-20. Radial distribution of nanotube with no applied charge (Case 7, no charge, 12  $K^+$ , 6  $SO_4$ , 0.1M).



A



B

Figure 9-21. Electric field of total system. A) Case 3 (charge is -14, 134  $K^+$ , 60  $SO_4$ , 1.0M), B) Case 6 (charge is 14, 120  $K^+$ , 67  $SO_4$ , 1.0M).

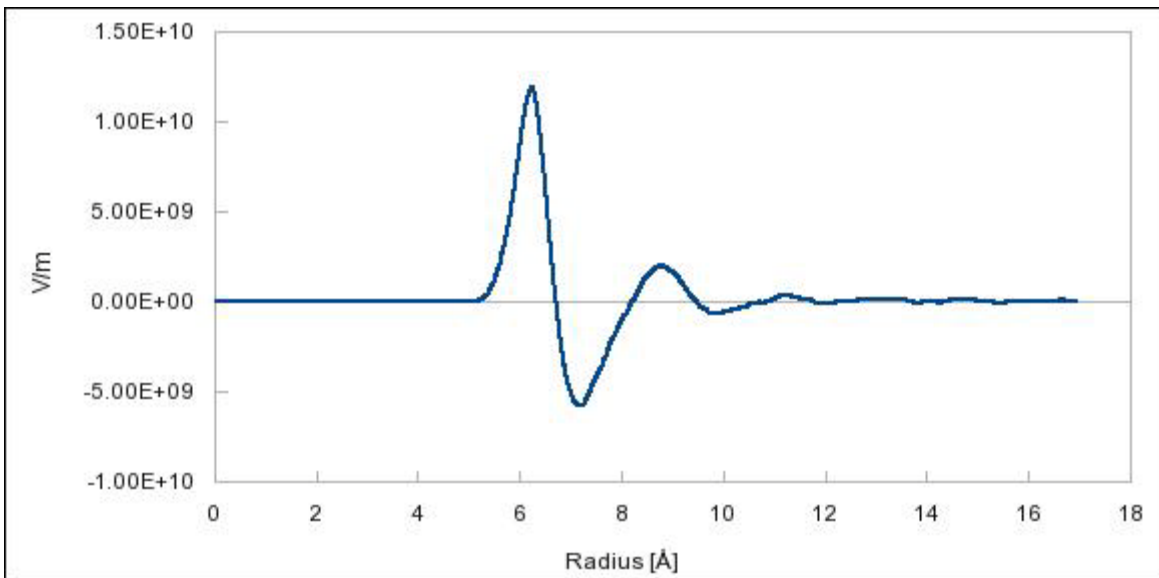
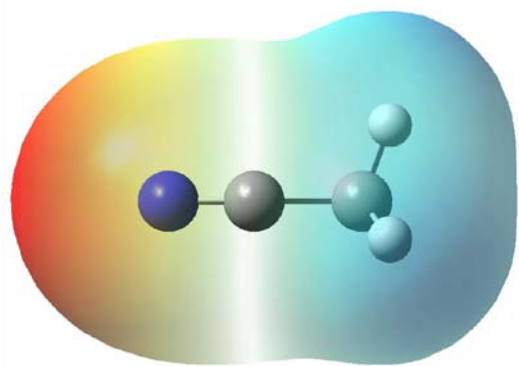
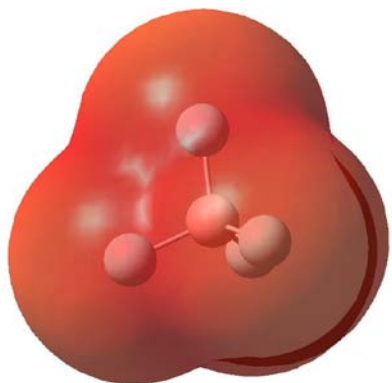


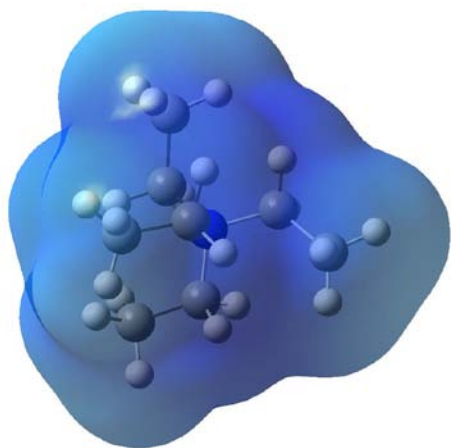
Figure 9-22. Electric field on discharged system (Case 7, no charge, 12 K<sup>+</sup>, 6 SO<sub>4</sub>, 0.1M).



A



B



C

Figure 9-23. Electron density of: A) acetonitrile (CH<sub>3</sub>CN, abbreviated ACN), B) boron tetrafluoride (BF<sub>4</sub><sup>-</sup>), C) tetraethylammonium ion (C<sub>8</sub>H<sub>20</sub>N<sup>+</sup>, abbreviated TEA<sup>+</sup>) where the blue end of the spectrum is a negative charge and red is a positive charge.

## CHAPTER 10 CONCLUSIONS

In this work, we studied the effect of using nanostructured materials on the design of radiation detection devices (by performing experiments on photoconductors) and energy storage devices (by performing computational calculations on capacitors).

First, we investigated replacing the photomultiplier tubes in scintillators with photoconductors to make radiation detectors more portable. The organic photoconductors developed in this study could provide a low cost, large area ( $>10\text{cm}^2$ ) alternative to conventional silicon photodiodes for readout of large scintillators that are used at border crossings, ports, toll plazas, nuclear facilities, etc. for monitoring the movement of radioactive material and distinguishing threats from non-threats. Lateral photoconductors with interdigitated electrodes and organic materials used for the active layer were studied. In order for these types of devices to be competitive with the photomultipliers currently in use in radiation detectors, they need to have high quantum efficiency. We studied photoconductors with bulk and planar heterojunctions to find which steps in the transport process limit the quantum efficiency in each type of device.

Second, we studied capacitors as efficient electrical energy storage devices. Conventional batteries use a chemical reaction to store energy, but after many charge-discharge cycles the battery loses capacity to the point where the user has to discard it. However, capacitors store energy as an electric field of charged particles created by two metal electrodes and therefore have a significantly longer lifetime. Capacitors also charge faster and last longer than normal batteries. The problem is that storage capacity is proportional to the surface area of the capacitor's electrodes, so even today's most powerful capacitors hold 25 times less energy than similarly sized standard

chemical batteries. We studied nanoscale capacitors because they have large surface to volume ratio and a small distance between electrodes, which creates a very high storage capacity. We used computational models to gain an atomic-level understanding of how molecules behave in electric fields generated by the capacitor in order to relate them to bulk effects.

### **Organic Electronic Photoconductors**

Organic semiconductors are promising materials for large area photodetectors not only because of their low cost and large area processability, but also because they can have relatively large bandgaps and low dielectric constants which enable low capacitance (and hence low noise) interdigitated device structures. In a bulk heterojunction, an electron-accepting and an electron-donating material are blended together. If the length scale of the blend is similar to the exciton diffusion length, then excitons are photogenerated in either material and are able to diffuse to an interface and dissociate. In a planar heterojunction, the organic donor–acceptor interface separates excitons much more efficiently than the organic–metal interfaces in a single layer device and evaporate materials have a higher purity (as compared to spin-coating), so more efficient devices may be made.

#### **Bulk Heterojunction**

Devices with a bulk heterojunction made with a spin-coated blend of a poly[2-methoxy-5-(2-ethylhexyl-oxy)-1,4-phenylene-vinylene] [MEH-PPV] and {6}-1-(3-(methoxycarbonyl) propyl)-{5}-1-phenyl-[6,6]-C61 [PCBM] were tested. Quantum efficiencies over 70% were demonstrated in these devices. It was also found that the absorption in the MEH-PPV/PCBM films could be fit with a linear sum of the absorption of MEH-PPV and PCBM films. We found that the quantum efficiency spectra followed

the absorption spectra for films with optical densities less than one. In these bulk heterojunction devices, the quantum efficiency was limited by the dissociation of the excitons. The field dependence of the dissociation of the excitons was explained using a modified Onsager model for charge dissociation.

### **Planar Heterojunction**

Planar heterojunction evaporated devices were made from layers of alpha-sexithiophene [ $\alpha$ -6T] and C<sub>60</sub>. It was found that trap sites in the active layer limited the quantum efficiency in these types of devices. By modeling the quantum efficiency based on exciton diffusion to the interface and the dissociation of the excitons, the experimental quantum efficiency was explained by a trapping model with a charge carrier lifetime of 0.002s. Heterojunction energy offsets were also studied utilizing several different polymers as the hole-transporting material in the planar heterojunction devices: poly(2-methoxy-5-(2'-ethyl)hexoxy-phenylenevinylene) (MEH-PPV), poly[2-methoxy-5-(2-ethylhexyloxy)- $\alpha$ -cyano-p-phenylene vinylene] (MEH-CN-PPV), poly(9,9-dioctylfluorene-co-benzothiadiazole) (F8BT), and poly(9,9-dioctylfluorene) (PFO), and it was found that a larger offset leads to higher quantum efficiency per absorbed photon.

### **Future Work**

Since carrier transport in the organic materials was determined to be a significant factor in device performance, studies to measure the carrier mobility of the materials in the bulk and planar heterojunction devices could be done to further understand the transport process. Mobility is calculated from the speed of the response of the photoconductivity, usually under such conditions that only one type of carrier dominates. Measurements could be performed using the time-of-flight method or by dark injection.

The results from these measurements on similar sets of devices to the previous experiments (with varying organic materials used, electrode spacing, polymer thickness, applied field, etc.) would provide insight into which parts of the carrier transport process (absorption, excitons reaching the interface of the two transport materials, dissociation of the exciton, or transport of the charge carriers to the electrodes without recombining at trap sites) has the greatest effect on device performance (quantum efficiency).

### **Capacitors for Energy Storage**

At present, the specific energy density of capacitors remains less than that for batteries. However they are superior in peak output, efficiency, and cycle time. The challenge is to develop new capacitors with increased energy storage density without sacrificing the other attributes. The move to the nanoscale is of particular interest as it provides a high surface to volume ratio which allows small electrode separations to be realized. We studied the effects of an applied electric field on both a single molecule and an electrolyte solution surrounding an electrode.

### **Electrode Geometry**

Density functional theory calculations using the B3LYP hybrid functional were performed on a carbon monoxide (CO) molecule in an applied electric field. The field was generated by charged electrodes consisting of point charges shaped as a plate or hollow cylinder or sphere. It was found that that the CO bond breaks at an applied field of 98.5V/nm in a uniform axial electric field, whereas in a field created by a sphere and plate the CO bond breaks at an applied field of 74.0V/nm, a 25% reduction. This difference can be accounted for by the electric field gradient. The energies of the molecular orbitals were studied during the bond breaking and it was found that the pi orbitals, originally at a lower energy, switch energy levels with the sigma orbitals as the

bond breaks. Similar behavior was found for the dinitrogen ( $N_2$ ) molecule. Electron density and molecular orbital shapes were also investigated during the bond-breaking process and the results are discussed.

### **Electric Double-Layer Carbon Nanotube Supercapacitors**

We studied the effects of an applied electric field on the dynamics of an electrolyte surrounding a charged carbon nanotube (CNT). We were able to see the charge double layer formation when a field was applied. Differences in the distribution of the ions were found for positively and negatively charged systems and were dependent on the relative size of the ions in the electrolyte. It was also found that the total electric field on the system was controlled by the charge on the CNT at a short range and then by the charge on the dielectric at a long range. Similar effects were seen for both the acetonitrile electrolyte system and the water electrolyte system. The effects of the polarization of each individual molecule were studied, and it was found that the dipole on the ions when near a charged CNT was 80-500 times larger than the dipole of the atoms normally. No significant change was seen in the molar volume of the electrolyte molecules due to the charged CNT.

### **Future Work**

We have only begun to study electric double-layer supercapacitors at the molecular level. There are many additional areas to be investigated to have a more full understanding of how the capacitor systems work. The effects of temperature on the charge double-layer could be studied. The diffusion coefficients of one species in another could be calculated using the same type of calculations that we have performed. Also, we study a system that already has an applied charge; the dynamics of charging and discharging is an appealing topic that would need to be addressed

before these devices could be used in real-world applications. Finally, it would be of interest to work on the development of a force field that takes into account the polarization effects on the individual molecules. This would tie the calculations done on the CO molecule in an applied field to the results for the carbon nanotube supercapacitor system.

## LIST OF REFERENCES

- 1 Shull, R. D. Nanostructured Materials. *NIST Nanosturcutred Materials Program Overview* (1997).
- 2 Moriarty, P. Nanostructured Materials. *Reports on Progress in Physics* **64**, 297-381 (2001).
- 3 Schoonman, J. Nanostructured materials in solid state ionics. *Solid State Ionics* **135**, 5-19, doi:Doi: 10.1016/s0167-2738(00)00324-6 (2000).
- 4 Li, R. *et al.* UV-shielding properties of zinc oxide-doped ceria fine powders derived via soft solution chemical routes. *Materials Chemistry and Physics* **75**, 39-44, doi:Doi: 10.1016/s0254-0584(02)00027-5 (2002).
- 5 Buffat, P. & Borel, J. P. Size effect on the melting temperature of gold particles. *Physical Review A* **13**, 2287 (1976).
- 6 Dallas, P. *et al.* Synthesis, characterization and thermal properties of polymer/magnetite nanocomposites. *Nanotechnology* **17**, 2046-2053 (2006).
- 7 Talwar, S., Hinestroza, J. Pourdeyhimi, B., Khan, S. Associative Polymer Facilitated Electrospinning of Nanofibers. *Macromolecules* **41**, 4275-4283 (2008).
- 8 *NanoTex*, <<http://www.nano-tex.com/>>
- 9 *Argonide Filtration*, <[www.arognide.com](http://www.arognide.com)>
- 10 Geelhood, B. D. *et al.* in *Nuclear Science Symposium Conference Record, 2003 IEEE*. (ed J. H. Ely) 513-517 Vol.511.
- 11 Knoll, G. F. *Radiation Detection and Measurement, 3rd ed.*, 287-292 (Wiley, 2000).
- 12 Suffert, M. SILICON PHOTODIODE READOUT OF SCINTILLATORS AND ASSOCIATED ELECTRONICS. *Nuclear instruments & methods in physics research. Section A, Accelerators, spectrometers, detectors and associated equipment* **322**, 523-528 (1992).
- 13 Svensson, M., Zhang, F., Inganas, O. & Andersson, M. R. Synthesis and properties of alternating polyfluorene copolymers with redshifted absorption for use in solar cells. *Synthetic metals* **135-136**, 137-138 (2003).
- 14 Zhu, R. y. Radiation damage in scintillating crystals. *Nuclear Instruments and Methods in Physics Research Section A: Accelerators, Spectrometers, Detectors and Associated Equipment* **413**, 297-311 (1998).

- 15 Biagtan, E., Goldberg, E., Harmon, J., and Stephens, R. Effect of gamma radiation dose rate on the light output of commercial polymer scintillators. *Nuclear Instruments and Methods in Physics Research B* **93**, 296-301 (1994).
- 16 Bross, A. D. & Pla-Dalmau, A. Radiation damage of plastic scintillators. *Nuclear Science, IEEE Transactions on* **39**, 1199-1204 (1992).
- 17 Kryshkin, V. I., Turchanovich, L. K. & Vasil'chenko, V. G. Light yield dependence of a plastic scintillator excited with UV laser and radioactive source on radiation dose. *Nuclear Instruments and Methods in Physics Research Section A: Accelerators, Spectrometers, Detectors and Associated Equipment* **381**, 573-575 (1996).
- 18 Kudo, K., Iizuka, M., Kuniyoshi, S. & Tanaka, K. Device characteristics of lateral and vertical type organic field effect transistors. *Thin Solid Films* **393**, 362-367 (2001).
- 19 Sakai, E. Pages: 418-422.
- 20 Valentine, J., Wehe, D., Knoll, G. & Moss, C. in *Nuclear Science Symposium and Medical Imaging Conference, 1991., Conference Record of the 1991 IEEE*. 176-182 vol.171.
- 21 Valentine, J. D., Moses, W. W., Derenzo, S. E., Wehe, D. K. & Knoll, G. F. Temperature dependence of CsI(Tl) gamma-ray excited scintillation characteristics. *Nuclear Instruments and Methods in Physics Research Section A: Accelerators, Spectrometers, Detectors and Associated Equipment* **325**, 147-157 (1993).
- 22 Keszthelyi-Lindori, S. & Hrehuss, G. Scintillation response function and decay time of CsI(Na) to charged particles. *Nuclear Instruments and Methods* **68**, 9-12 (1969).
- 23 Holl, I., Lorenz, E. & Mageras, G. A measurement of the light yield of common inorganic scintillators. *Nuclear Science, IEEE Transactions on* **35**, 105-109 (1988).
- 24 Moszynski, M., Kapusta, M., Mayhugh, M., Wolski, D. & Flyckt, S. O. Absolute light output of scintillators. *Nuclear Science, IEEE Transactions on* **44**, 1052-1061 (1997).
- 25 Abramowitz, M. & Davidson, M. Concepts in Digital Imaging Technology: Photomultiplier Tubes.

- 26 Yamamoto, K., Fujii, Y., Kotooka, Y. & Katayama, T. Highly stable silicon pin photodiode. *Nuclear Instruments and Methods in Physics Research Section A: Accelerators, Spectrometers, Detectors and Associated Equipment* **253**, 542-547 (1987).
- 27 Rose, J. D. & Stratham, E. S. *J. Chem. Soc.* **69** (1950).
- 28 Ashcroft, N. W. & Mermin, N. D. *Solid State Physics*. International Edition edn, (Saunders College Publishing, 1988).
- 29 Riande, E. & Diaz-Calleja, R. *Electrical Properties of Polymers*. (Marcel Dekker, 2004).
- 30 Hadziioannou, G. & Hutten, P. F. v. *Semiconducting Polymers: Chemistry, Physics and Engineering*. (Wiley-VCH, 2000).
- 31 Yamashita, J. & Kurosawa, T. On electronic current in NiO. *Journal of Physics and Chemistry of Solids* **5**, 34-43 (1958).
- 32 Holstein, T. Studies of polaron motion : Part II. The "small" polaron. *Annals of Physics* **8**, 343-389 (1959).
- 33 Fesser, K., Bishop, A. R. & Campbell, D. K. Optical absorption from polarons in a model of polyacetylene. *Physical Review B* **27**, 4804 (1983).
- 34 Blythe, T. & Bloor, D. *Electrical Properties of Polymers*. 2nd edn, (Cambridge University Press, 2005).
- 35 Bredas, J. L., Chance, R. R. & Silbey, R. Comparative theoretical study of the doping of conjugated polymers: Polarons in polyacetylene and polyparaphenylene. *Physical Review B* **26**, 5843 (1982).
- 36 Bredas, J. L., Scott, J. C., Yakushi, K. & Street, G. B. Polarons and bipolarons in polypyrrole: Evolution of the band structure and optical spectrum upon doping. *Physical Review B* **30**, 1023 (1984).
- 37 Mizes, H. A. & Conwell, E. M. Photoinduced charge transfer in poly(p-phenylene vinylene). *Physical Review B* **50**, 11243 (1994).
- 38 Stafstrom, S. Soliton lattice in highly doped trans-polyacetylene. *Physical Review B* **43**, 9158 (1991).
- 39 Hoppe, H., Sariciftci, N.S. Organic solar cells: An overview. *Journal of Material Research* **19**, 1924-1945 (2004).

- 40 Vissenberg, M. C. J. M. & Matters, M. Theory of the field-effect mobility in amorphous organic transistors. *Physical Review B* **57**, 12964 (1998).
- 41 Niemeyer, A. C., Campbell, I. H., So, F. & Crone, B. K. High quantum efficiency polymer photoconductors using interdigitated electrodes. *Applied physics letters* **91**, 103504 (2007).
- 42 Campbell, I. H., Hagler, T. W., Smith, D. L. & Ferraris, J. P. Direct measurement of conjugated polymer electronic excitation energies using metal/polymer/metal structures. *Physical review letters* **76**, 1900-1903 (1996).
- 43 Goris, L. *et al.* Absorption phenomena in organic thin films for solar cell applications investigated by photothermal deflection spectroscopy. *Journal of materials science* **40**, 1413-1418 (2005).
- 44 Brabec, C. J., Sariciftci, N. S. & Hummelen, J. C. Plastic solar cells. *Advanced functional materials* **11**, 15-26 (2001).
- 45 Heller, C. M., Campbell, I. H., Smith, D. L., Barashkov, N. N. & Ferraris, J. P. Chemical potential pinning due to equilibrium electron transfer at metal/C60-doped polymer interfaces. *Journal of applied physics* **81**, 3227-3231 (1997).
- 46 Sariciftci, N. S. & Heeger, A. J. Reversible, metastable, ultrafast photoinduced electron transfer from semiconducting polymers to buckminsterfullerene and in the corresponding donor/acceptor heterojunctions. *International journal of modern physics. B, Condensed matter physics, statistical physics, applied physics* **8**, 237-274 (1994).
- 47 Yu-Xiang, L., Summers, M. A., Scully, S. R. & McGehee, M. D. Resonance energy transfer from organic chromophores to fullerene molecules. *Journal of applied physics* **99**, 93521-93521 (2006).
- 48 van Duren, J. K. *et al.* Relating the morphology of a poly(p-phenylene vinylene)/methanofullerene blend to bulk heterojunction solar cell performance. *Proceedings of SPIE--the international society for optical engineering* **5215**, 99-110 (2004).
- 49 Onsager, L. Initial recombination of ions. *Physical review* **54**, 554-557 (1938).
- 50 Langevin, P. The recombination and mobilities of ions in gases. *Annales de chimie et de physique* **28**, 433-530 (1903).
- 51 Braun, C. L. Electric field assisted dissociation of charge transfer states as a mechanism of photocarrier production. *The Journal of chemical physics* **80**, 4157-4161 (1984).

- 52 Goliber, T. E. & Perlstein, J. H. Analysis of photogeneration in a doped polymer system in terms of a kinetic model for electric-field-assisted dissociation of charge-transfer states. *The Journal of chemical physics* **80**, 4162-4167 (1984).
- 53 Mihailetchi, V. D., Koster, L. J. A., Hummelen, J. C. & Blom, P. W. M. Photocurrent generation in polymer-fullerene bulk heterojunctions. *Physical review letters* **93**, 216601-216604 (2004).
- 54 Szmytkowski, J., Stampor, W., Kalinowski, J. & Kafafi, Z. H. Electric field-assisted dissociation of singlet excitons in tris-(8-hydroxyquinolino) aluminum (III). *Applied physics letters* **80**, 1465-1467 (2002).
- 55 Nunzi, J. M., Juska, G., Jean, F. & Arlauskas, K. Slowup of bimolecular recombination in organic polymer solar cells. *Acta physica Polonica. A* **107** (2005).
- 56 Nogueira, A. F. *et al.* Charge recombination in conjugated polymer/fullerene blended films studied by transient absorption spectroscopy. *Journal of Physical Chemistry B* **107**, 1567-1573 (2003).
- 57 Chern, G., Mathias, H., Testardi, L. R., Seger, L. & Schlenoff, J. Low-frequency dielectric permittivity of C60. *Journal of superconductivity* **8**, 207-210 (1995).
- 58 Tammer, M. & Monkman, A. P. Measurement of the anisotropic refractive indices of spin cast thin poly(2-methoxy-5-(2-ethyl-hexyloxy)-p-phenyl-enevinylene) (MEH-PPV) films. *Advanced materials* **14**, 210 (2002).
- 59 Choulis, S. A. *et al.* Transport and Recombination Dynamics Studies of Polymer/Fullerene Based Solar Cells. *Macromolecular symposia* **205**, 1-7 (2004).
- 60 Mayer, A. C., Scully, S. R., Hardin, B. E., Rowell, M. W. & McGehee, M. D. Polymer-based solar cells. *Materials Today* **10**, 28-33 (2007).
- 61 Bube, R. H. *Photoconductivity of Solids*. (John Wiley and Sons, 1960).
- 62 Peumans, P., Yakimov, A. & Forrest, S. R. Small molecular weight organic thin-film photodetectors and solar cells. *Journal of Applied Physics* **93**, 3693-3723 (2003).
- 63 Blumstengel, S., Sadofev, S. & Henneberger, F. Electronic coupling of optical excitations in organic/inorganic semiconductor hybrid structures. *New Journal of Physics* **10** (2008).
- 64 Schon, J. H., Kloc, C., Fichou, D. & Batlogg, B. Conjugation length dependence of the charge transport in oligothiophene single crystals. *Physical Review B* **64**, 035209 (2001).

- 65 Rose, A. *Concepts in Photoconductivity and Allied Problems*. (Robert E. Krieger Publishing Co., 1978).
- 66 Bak, G. W., Dluzniewski, M., Staryga, E., Kania, S. & Walocha, J. Recombination lifetime of charge carriers in DLC thin films. *Diamond and Related Materials* **9**, 1357-1361 (2000).
- 67 Dennler, G. *et al.* Charge carrier mobility and lifetime versus composition of conjugated polymer/fullerene bulk-heterojunction solar cells. *Organic Electronics* **7**, 229-234 (2006).
- 68 Conner, M. Portable Power: Features Abound, Thanks to New Battery Chemistries. *EDN Europe* (January 2008).
- 69 Whittingham, S. Energy Storage for Portable and Stationary Application: Materials Limitations. *Clean Tech, Applied. The Applied Materials Blog*. (2010). <<http://blog.appliedmaterials.com/energy-storage-portable-and-stationary-application-materials-limitations>>.
- 70 in *Encyclopedia Britannica* (ed et. al. Nicholas Carr) (2008).
- 71 Curtis, K. Replacing Chemical Battery Storage with Supercapacitors into Your Embedded Design. *EE Times, Design Line Power Management* (2008).
- 72 Zyga, L. Ultracapacitors Make City Buses Cheaper, Greener. *physorg.com* (2009).
- 73 G. Fujita, R. Y., T. Niimura, D. Makita, S. Takeuchi, G. Shirai. Power System Stabilizing Control Using Variable Series Capacitor Based on H Control Theory Considering AVR and Governor. *IEEE Xplore*, 43-46 (1997).
- 74 Chen Min, C. Y., Zhong Wu & Yang JueKuan. Molecular dynamics simulation of ion transport in a nanochannel. *Science China Technological Sciences* **51**, 921-931 (2008).
- 75 Joly, L., Ybert, C., Trizac, E. & Bocquet, L. Hydrodynamics within the Electric Double Layer on Slipping Surfaces. *Physical Review Letters* **93**, 257805 (2004).
- 76 Yang, K., Yiacoymi, S, Tsouris, C. Electrical Double-Layer Formation. *Dekker Encyclopedia of Nanoscience and Nanotechnology*, doi:10.1081 (2004).
- 77 Joseph, S. & Aluru, N. R. Hierarchical Multiscale Simulation of Electrokinetic Transport in Silica Nanochannels at the Point of Zero Charge. *Langmuir* **22**, 9041-9051, doi:10.1021/la0610147 (2006).

- 78 Qiao, R. & Aluru, N. R. Atypical Dependence of Electroosmotic Transport on Surface Charge in a Single-wall Carbon Nanotube. *Nano Letters* **3**, 1013-1017, doi:10.1021/nl034236n (2003).
- 79 Morse, P. M. a. F., H. *Methods in Theoretical Physics, Part II.* (McGraw Hill Science/Engineering/Math, 1953).
- 80 Alder, B. J. & Wainwright, T. E. Phase Transition for a Hard Sphere System. *The Journal of Chemical Physics* **27**, 1208-1209 (1957).
- 81 Alder, B. J. & Wainwright, T. E. Studies in Molecular Dynamics. I. General Method. *The Journal of Chemical Physics* **31**, 459-466 (1959).
- 82 Alder, B. J. & Wainwright, T. E. Studies in Molecular Dynamics. II. Behavior of a Small Number of Elastic Spheres. *The Journal of Chemical Physics* **33**, 1439-1451 (1960).
- 83 Alder, B. J. & Wainwright, T. E. Phase Transition in Elastic Disks. *Physical Review* **127**, 359 (1962).
- 84 Cramer, C. *Essentials of Computational Chemistry. Theories and Models.*, (John Wiley & Sons Ltd., 2002).
- 85 Jensen, F. *Introduction to Computational Chemistry.* (John Wiley & Sons Ltd, 1999).
- 86 Szabo A., O. N. *Modern Quantum Chemistry.* (McGraw - Hill, 1982).
- 87 Parr, R., Yang W. *Density Functional Theory of Atoms and Molecules.* (Oxford University Press, 1989).
- 88 Koch, W., Holthauseb, M. *A Chemist's Guide to Density Functional Theory.* Vol. 3 (Wiley - VCH, 2001).
- 89 Maroulis, G. Electric Polarizability and Hyperpolarizability of Carbon Monoxide. *The Journal of Physical Chemistry* **100**, 13466-13473, doi:10.1021/jp960412n (1996).
- 90 Hush, N. S. a. W., M.L. Carbon monoxide bond length, force constant and infrared intensity variations in strong electric fields: Valence-shell calculations, with applications to properties of adsorbed and complexed CO. *Journal of Molecular Spectroscopy* **50**, 349-368 (1974).
- 91 Becke, A. D. Density-functional exchange-energy approximation with correct asymptotic behavior. *Physical Review A* **38**, 3098 (1988).

- 92 Lee, C., Yang, W. & Parr, R. G. Development of the Colle-Salvetti correlation-energy formula into a functional of the electron density. *Physical Review B* **37**, 785 (1988).
- 93 Gaussian 09 Revision A.2 (Gaussian Inc., wallingford CT, 2009).
- 94 Hariharan, P. C., Pople, J. A. The influence of polarization functions on molecular orbital hydrogenation energies. *Theoretical Chemistry Accounts: Theory, Computation, and Modeling (Theoretica Chimica Acta)* **28**, 213-222 (1973).
- 95 Gilliam, O. R., Johnson, C. M. & Gordy, W. Microwave Spectroscopy in the Region from Two to Three Millimeters. *Physical Review* **78**, 140 (1950).
- 96 L. Martínez, R. A., E. G. Birgin, J. M. Martínez. Packmol: A package for building initial configurations for molecular dynamics simulations. *Journal of Computational Chemistry* **30**, 2157-2164 (2009).
- 97 Luzhkov, V. B., Osterberg, F., Acharya, P., Chattopadhyaya, J. and Aqvist, J. Computational and NMR study of quaternary ammonium ion conformations in solution. *Journal of Physical Chemistry Chemical Physics* **4**, 4640-4647, doi:10.1039/b203526j (2002).
- 98 de Andrade, J., Boes, E. S. & Stassen, H. Computational Study of Room Temperature Molten Salts Composed by 1-Alkyl-3-methylimidazolium Cations Force-Field Proposal and Validation. *The Journal of Physical Chemistry B* **106**, 13344-13351, doi:10.1021/jp0216629 (2002).
- 99 Wang, J., Wolf, R. M., Caldwell, J. W., Kollman, P. A. & Case, D. A. Development and testing of a general amber force field. *J Comput Chem* **25**, 1157-1174, doi:citeulike-article-id:197425 (2004).
- 100 Futaba, D. N. *et al.* Shape-engineerable and highly densely packed single-walled carbon nanotubes and their application as super-capacitor electrodes. *Nat Mater* **5**, 987-994, doi:http://www.nature.com/nmat/journal/v5/n12/supinfo/nmat1782\_S1.html (2006).
- 101 AMBER 9 (Univeristy of California, San Francisco, 2006).
- 102 L. Yang, B. F., A. Migliori, L. Pratt. Dielectric saturation of liquid propylene carbonate in electrical energy storage applications. *Journal of Chemical Physics* **132**, 044701 (2010).

## BIOGRAPHICAL SKETCH

Alyson Niemeyer grew up in Ormond Beach, Florida. She is the eldest of two daughters and graduated from the Spruce Creek High School International Baccalaureate Program in 2001. She earned her Bachelor of Science in chemical engineering and her Master of Science in materials science and engineering from the University of Florida.

During her studies, Alyson had the opportunity to do several internships involving a variety of research projects: she did most of her graduate research for her dissertation at Los Alamos National Laboratory (LANL) in Los Alamos, New Mexico; she spent a summer at the Technical University of Delft in The Netherlands working on a particle concentrator for use in a bioaerosol alarm; she worked at the Particle Engineering Research Center at the University of Florida researching nano-scale high aspect ratio copper platelets; she did an internship with the National Aeronautics and Space Administration (NASA) working in the applied chemistry laboratory on a variety of projects; she participated in the International Institute of Women in Engineering's summer program at the Ecole Polytechnic Feminine in Paris, France; and she worked at the Volusia County Environmental Health Lab on a project testing surface water sites for possible use in sprinkler water augmentation.

Alyson has also continued her childhood hobby of dance during her collegiate career, by participating in a professional dance performance organization through the University of Florida and teaching dance to children and adults at local dance studios. Upon completion of her Ph.D. program, Alyson will begin a career at Intel working as a process engineer in a fabrication facility in Albuquerque.